

A ROBOTIC DEVICE TO ASSIST WITH IN-VIVO MEASUREMENT OF HUMAN PELVIC ORGAN TISSUE
PROPERTIES

by

SHASHANK SANJAY KUMAR

THESIS

Submitted in partial fulfillment of the requirements for the degree of Masters of Science in
Mechanical engineering at The University of Texas at Arlington

December, 2016

Arlington, Texas

Copyright©
Shashank Sanjay Kumat
2016

Acknowledgement

Firstly I would like to thank The University of Texas at Arlington for considering me a capable graduate student. I would like to express my sincere gratitude towards my professor, Dr. Panos Shiakolas, who have helped me throughout my thesis. Without his support and invaluable expertise in the field of this research, it would have been difficult to accomplish the goal. At times when I lost my track or felt nervous, Dr. Shiakolas, being patient, showed faith in me and boosted my confidence. I would like to thank my committee members Dr. Ratan Kumar and Dr. Tre Welch for providing me with their valuable insight and recommendations over the research. I would also like to thank Dr. Zimmern of UT Southwestern medical center, who guided us as far as biological perspective of the project was concerned. I would like to thank UTA machine shop members, Kermit and Sam who helped me out with the fabrication and assembly of the sensor components. I am grateful towards the support and views provided by my lab mates at the MARS lab. Thank you Christopher, Hasan, Prashanth, Michael, Zach and Samson. I would also like to thank my friends, and my roommates who became my family in the United States. Last but certainly not the least I would like to thank my parents and my brother for coping up and supporting me at all times. I wouldn't have reached so far without your blessing *Mommy and Daddy*.

List of Illustrations

| | |
|---|----|
| Figure 1: Peritoneum cavity and bladder location for male human body [5] | 3 |
| Figure 2: Various sections in male urinary tract [13] | 7 |
| Figure 3: Tissue layer arrangement in bladder and trigone area of the bladder [17] | 7 |
| Figure 4: Anatomical regions that will be used to provide support or boundary condition in finite element analysis [3] | 9 |
| Figure 5: Rigid cystoscopy to examine the inner bladder wall [21] | 10 |
| Figure 6: Experimental stress as a function of elongation for urinary bladder evaluated by Bush <i>et al.</i> and Yamada <i>et al.</i> [22] [26] | 12 |
| Figure 7: ANSYS Workbench 17.0 regression curve fit for stress as a function of strain for experimental data obtained by Yamada <i>et al.</i> | 15 |
| Figure 8: ANSYS Workbench 17.0 bladder model boundary condition | 17 |
| Figure 9: Deformation of bladder tissue on applied load of 0.01 MPa | 17 |
| Figure 10: A concentric tube robot comprising of 3 tubes [42] | 20 |
| Figure 11: Proposed Robotic device assembly | 23 |
| Figure 12: Rigid link manipulator: inner tube with detailed front view | 24 |
| Figure 13: I-beam model to anchor the tendons | 25 |
| Figure 14: Rigid link manipulator: link 2A | 26 |
| Figure 15: Rigid link manipulator: link 2B | 26 |
| Figure 16: Rigid link manipulator: sensor support | 27 |
| Figure 17: A 5 times scaled prototype for verification of the concept of design .. | 28 |
| Figure 18: Frame assignment for kinematic analysis | 30 |
| Figure 19: Significance of homogenous transformation matrix | 32 |

| | |
|---|---------------|
| Figure 20: Torque experienced in different configuration due to normal load..... | 42 |
| Figure 21: Schematic for double shear failure of the pin joint | 43 |
| Figure 22: I-beam boundary condition with fine mesh size | 44 |
| Figure 23: Proposed sensor working principle | 46 |
| Figure 24: Proposed sensor assembly model | 47 |
| Figure 25: Sensor assembly: sensor head component..... | 48 |
| Figure 26: Sensor assembly: upper clamp component..... | 49 |
| Figure 27: Sensor assembly: lower clamp component | 50 |
| Figure 28: Sensor assembly: beam component..... | 51 |
| Figure 29: Fixed-fixed beam schematic | 52 |
| Figure 30: Strain as a function of thickness for beam selection for applied load of 0.4 N | 53 |
| Figure 31: Strain as a function of applied force on the beam with various thicknesses | 55 |
| Figure 32: Boundary condition applied to model fixed at both end beam | Error! |
| Bookmark not defined. | |
| Figure 33: Strain gauge attached on the scaled aluminum prototype beam model | 55 |
| Figure 34: Schematic representation of forward kinematic analysis to verify if the device reaches the trigone area with coordinates 15.7, -11.1, -4.5..... | 58 |
| Figure 35: Schematic representation of forward kinematic analysis to verify if the device reaches the trigone area with coordinates 19.2, 2.1, 13.6 | 58 |
| Figure 36: Boundary condition and equivalent von-Mises stress determined on the sensor support component..... | 60 |

| | |
|--|----|
| Figure 37: Boundary condition and equivalent von-Mises stress determined on link 2B | 60 |
| Figure 38: Boundary condition and equivalent von-Mises stress estimated on link 2A | 61 |
| Figure 39: Boundary condition and equivalent von-Mises stress estimated on inner tube | 62 |
| Figure 40: Illustration of sensor assembly without sensor head component | 63 |
| Figure 41: Signal flow diagram of the proposed sensor design | 64 |
| Figure 42: Experimentally and theoretically comparison of strain experienced by the beam as a function of applied load | 66 |
| Figure 43: Extended degrees of Freedom | 69 |

List of Tables

| | |
|--|----|
| Table 1: Material properties of bladder tissue for different mammals [16] | 8 |
| Table 2: Yeoh's 3 rd order parameter constants for bladder analysis | 14 |
| Table 3: Design iterations | 21 |
| Table 4: MDH parameters for the manipulator | 30 |

Abstract

A robotic device to assist with in-vivo measurement of human pelvic organ tissue properties

Shashank Kumat, MS

The University of Texas at Arlington, 2016

Supervising Professor: Dr. Panos S. Shiakolas

Measurement of the biomechanical properties of human pelvic organ tissue without undergoing minimally invasive surgery is desired for diagnostics purposes and take precautionary actions if needed. The biomechanical properties of the bladder change with age and due to diseases. Thus, identification of the viscoelastic properties of the tissue could help in detecting early stages of the disease in the bladder. A literature survey revealed that no device exists that could be used to characterize the biomechanical properties of the human bladder in-vivo.

This research contributes towards the development of a diagnostic system that could be used in a medical setting to interact with the bladder during the examination. The research focuses on the conceptual design and development of a rigid link robotic device, which is inserted through the urethra and remotely actuated/guided to probe the inner wall of the human bladder. Also, this research discusses the design of a sensor attached to the tip of the robotic device to engage with the tissue in order to obtain reaction force measurement when the tissue is disturbed. These measurements will then be used to characterize the viscoelastic properties of the bladder tissue. Scaled models of the robotic device and sensor have been prototyped to verify the function of the proposed design

Table of Contents

| | |
|--|------|
| Acknowledgement..... | iii |
| List of Illustrations | iv |
| List of Tables..... | vii |
| Abstract..... | viii |
| Table of Contents..... | ix |
| Chapter 1 Introduction | 1 |
| 1.1 Problem Statement | 2 |
| 1.2 Thesis Outline | 4 |
| Chapter 2 Human Bladder Anatomy and FEM Approximation..... | 6 |
| 2.1 Human Bladder Anatomy | 6 |
| 2.2 Bladder Biomechanics | 7 |
| 2.3 Cystoscopy and Procedure | 9 |
| 2.4 FEA Approximation of the Human Bladder | 10 |
| 2.4.1 Tissue Properties | 10 |
| 2.4.2 Tissue Mathematical Modelling..... | 12 |
| Chapter 3 Diagnostic Robotic Device and Sensor Design | 18 |
| 3.1 Robotic Device Design | 18 |
| 3.1.1 Introduction..... | 18 |

| | | |
|-----------|---|----|
| 3.1.2 | Concentric Tube Robot..... | 19 |
| 3.1.3 | Rigid Link Manipulator: Design Iterations..... | 20 |
| 3.1.4 | Rigid Link Manipulator: Proposed Design | 22 |
| 3.1.5 | Analysis of Rigid Link Manipulator | 28 |
| 3.1.6 | Kinematic Analysis..... | 29 |
| 3.1.7 | Static Force Analysis..... | 37 |
| 3.1.8 | Failure Analysis for the Pin and I-beam | 42 |
| 3.1.9 | Part Failure Analysis | 44 |
| 3.2 | Sensor Design | 45 |
| 3.2.1 | Sensor Design Components | 47 |
| 3.2.2 | Analysis for Sensor Beam Design | 51 |
| 3.2.3 | Strain Gauge | 55 |
| Chapter 4 | Result and Discussion | 56 |
| 4.1 | Results..... | 56 |
| 4.1.1 | Kinematics Verification of the Design | 56 |
| 4.1.2 | Static Force and Joint Torque for Part Failure Analysis | 59 |
| 4.1.3 | Proposed Sensor Concept Verification | 62 |
| 4.2 | Discussion | 64 |
| Chapter 5 | Conclusions and Recommendation for Future Research..... | 67 |
| 5.1 | Conclusions..... | 67 |

| | | |
|-----------------|---|----|
| 5.2 | Recommendations..... | 68 |
| Appendix A | Part Drawings..... | 70 |
| A.1 | Inner Tube..... | 70 |
| A.2 | Link 2A | 71 |
| A.3 | Link 2B..... | 72 |
| A.4 | Sensor Support | 73 |
| A.5 | Sensor Head | 74 |
| A.6 | Upper Clamp | 75 |
| A.7 | Lower Clamp | 76 |
| A.8 | Beam.. | 77 |
| Appendix B | Generalized Forward Kinematics Code | 78 |
| Appendix C | Inverse Kinematics Code | 81 |
| Appendix D | Jacobian Determinant..... | 87 |
| Appendix E | Sensor Experiment data | 89 |
| References..... | | 90 |

Chapter 1

Introduction

The objective of this research is to measure the tissue properties of the human bladder using natural openings in the human body. The reason being the benefits of non-invasive surgery or diagnostics. The recovery time for noninvasive surgery is considerably less compared to that for invasive surgical procedures. Medical diagnosis is a process of determining which disease or condition explains a person's symptoms. The most common method for diagnosing a patient by a physician is by direct touch; physical contact of the tissue or organ. This is traditionally performed by the physician's subjective experience and judgment. For instance, to check the healthiness of the prostate gland in the males, the physician inserts a finger, via anus, to qualitatively assess the healthiness of the gland.

Thus, if a medical device is developed to measure tissue reaction force and the measurements were used to identify tissue properties, the physicians can gather quantitative data for the patient's tissue/organ which could supplement the qualitative assessment through other observations or diagnostics. This research focuses on the development of a medical diagnostic device which as part of a system will assist in evaluating quantitative tissue data. This way the physician can have quantitative patient history to review, assess, and provide next-step solutions.

The area of application for this research is the human bladder. The human bladder is an important organ of the excretory system and plays an important role in storing urine generated from the kidneys. Kidneys are continuously generating urine in the body and it is because of the bladder that we do not feel the need of urinating until the bladder is filled at 30 – 50% (or in

other terms, with the bladder volume from 600 – 800 ml, the micturition point will be around 180 – 400 ml [1]). The most common bladder problem in women is the frequent urge to urinate and the occasional urine leakage. This is often caused by a decreased volume capacity of the bladder and over-activity. Whereas the most common bladder problem in men is the frequent urge to urinate and the inability to completely empty the bladder, and this is the cause of an enlarged prostate obstructing the emptying of bladder [2]. Another problem that can originate in the bladder is cancer. According to the National Cancer Institute, about 70,000 people in the United States live with bladder cancer, although it typically affects older people. Younger people, however, have been recognized to develop bladder cancer as well [3].

1.1 Problem Statement

The human bladder is a vital organ of the excretory system. It is a muscular sac in the pelvis, just above and behind the pelvic bone. Figure 1 presents the peritoneum cavity and the location of the human bladder in males. The goal of this research is to design a diagnostic device such that it could reach and interact with the bladder tissue without invasive surgery. According to Lekka *et al.* it has been evaluated that the tissue stiffness noticeably reduces from a healthy bladder compared to a cancerous bladder [4]. Similarly, a healthy bladder is stiffer for younger people, however, this stiffness reduces with age. The challenge of the present research will be to design and model a device that will reach the male urinary bladder without requiring anesthesia, remotely actuate to interact with the bladder and provide the physician with quantitative data to track the healthiness of the bladder over time.

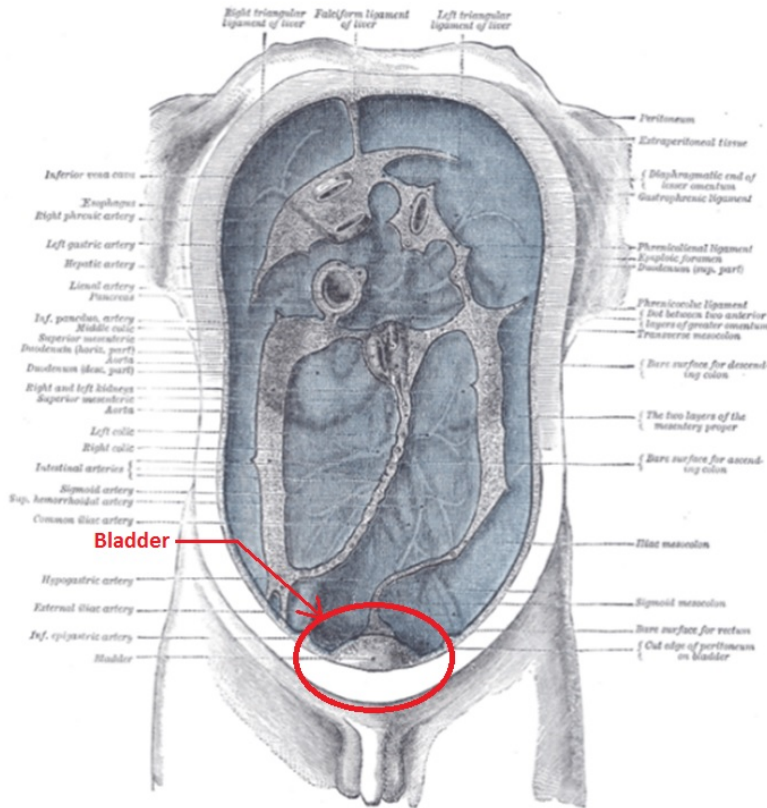


Figure 1: Peritoneum cavity and bladder location for male human body [5]

Current technologies used to visually inspect the bladder include rigid and flexible cystoscopy. A cystoscope is a device used to visually inspect the bladder. However, since the average diameter of the cystoscope is about 7 mm, general anesthesia is needed to numb the urinary tract during cystoscopy [6]. Further details regarding cystoscopy will be discussed in Section 2.3. The major challenge in designing this diagnostic device will be to maintain the maximum outer diameter under 3 mm in order to lessen any patient discomfort according to Zimmern *et al.* and Stav *et al.* [7] [8]. Therefore, a device needs to be designed such that it could be pushed through the urinary tract to reach the bladder, and externally manipulated inside the bladder to measure the reaction forces which will help evaluate the tissue properties while at

the same time minimizing discomfort in the patient and providing quantitative data to the physician.

1.2 Thesis Outline

The structure of the thesis is as follows. Chapter 1 provides an introduction to the importance of the bladder and diseases which the bladder is prone to. Other issues related to bladder diagnosis are briefly mentioned. A literature survey was performed to assess the progress in the field of bladder diagnostics. Furthermore, an introduction on the goals and the challenges for this research is also provided.

Chapter 2 focuses on the anatomy of the bladder, relationship between the organs surrounding the bladder and their interaction. An introduction on the biomechanical properties of the urinary bladder is also provided. Information on FDA-approved procedure for cystoscopy and how this procedure can be adapted to the newly designed device will also be introduced briefly. This chapter also discusses the various hyperelastic models in ANSYS Workbench 17.0 and their use to model soft tissues. Maximum allowable load on the area of interest which is the target for diagnosis, is also evaluated for design specifications of the device.

Chapter 3 focuses on the design of the device and sensor to reach, actuate and probe the inner bladder wall and measure tissue reaction forces. This chapter introduces initial design concepts and their limitations. It also provides an insight to the kinematic and force analysis of the device. ANSYS Workbench 17.0 models were developed and analyzed to evaluate the safety factors of the device. Holding joint torques were evaluated to define the specification of the actuators. The sensor model was designed such that a load obtained by probing the inner bladder

wall can be measured. A scaled prototype of the device and sensor were fabricated to confirm the operation of the proposed design.

Chapter 4 presents the information from the analysis performed in the previous chapters. The results include the forward and inverse kinematics solutions for different configurations of the device. Static force analysis was used to evaluate designed component safety factors to assess the possibility of failure of the design. Discussion on the initial calibration experiments of the proposed scaled sensor design is also provided.

Chapter 5 contains conclusions based on obtained results and provides recommendations for future research based on the analyzed results.

Chapter 2

Human Bladder Anatomy and FEM Approximation

2.1 Human Bladder Anatomy

The human bladder is a hollow muscular organ situated in the peritoneum cavity at the base of the pelvis; for men, it lies in front of the rectum, and for females, it lies in front of the uterus [9].

The combined study of urine flow in the bladder, the urinary sphincter, and the urethra is called the urodynamic. The bladder is lined with transitional epithelium tissue. Urodynamic investigations are one of the most recognized and definitive tests for the evaluation of organ functionality by a physiological micturition cycle [10]. The bladder can hold a range of 600 – 800 ml of urine [2]. To model the urinary bladder, a spherical shape is assumed and homogeneous distribution of stress and strain parameters are considered [11].

In females, the length of the urethra is approximately 4 cm long, whereas for males it ranges from 20 – 22 cm, the male urethra is divided into two parts, the anterior urethra which contains penile urethra and the posterior urethra which contains membranous urethra [12]. Figure 2 shows the different sections of the male urinary tract [13].

The wall of the bladder is made up of muscle fibers extending in all directions. At the bladder neck, relatively distinct layers appear. The inner layer of the bladder fuses with the inner longitudinal layer of the urethra. The middle layer of the bladder is most prominent in the proximity of the bladder neck and fuses with the trigonal muscle. The trigone is the triangular structure at the bladder neck. The urethra opens at the trigonal end [14]. Figure 3 shows a view of the human bladder trigone area. Various types of tissues and their arrangements have been

marked in Figure 3. The trigone is the area of interest and its stiffness helps determine the healthiness of the bladder, Zimmern *et al.* [8].

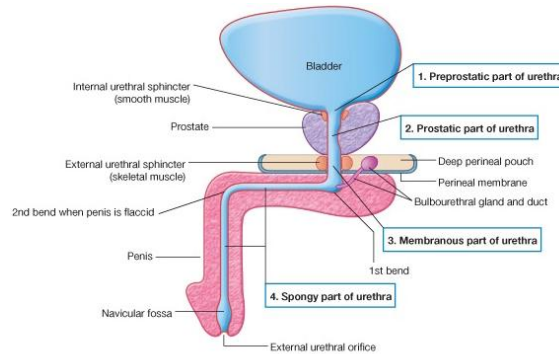


Figure 2: Various sections in male urinary tract [13]

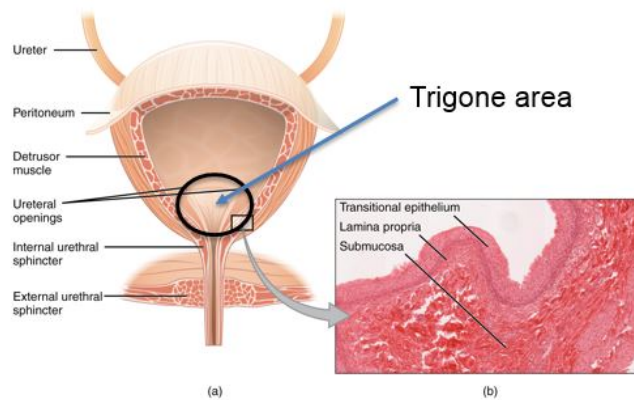


Figure 3: Tissue layer arrangement in bladder and trigone area of the bladder [17]

2.2 Bladder Biomechanics

To model a bladder by finite element method (FEM), the biomechanics of the bladder must be understood. The anatomy, and physiology of the bladder was briefly introduced in Section 2.1. The lower urinary tract consists of the bladder and the urethra which are situated at the

anterior part of the pelvic cavity. The bladder outlet and the urethra originate at the caudal end. The trigone is a triangle shaped area that lies between the outlets of ureters and urethra. To create a solid model for analysis it is important to review the general dimension of the trigone area. The angle between the internal urethral ostium and left/right urethral ostium is 77° respectively and the distance between urethral ostium is 1.9 cm [15]. The distance from internal urethral ostium to left urethral ostium and from internal urethral ostium to right urethral ostium are both 1.6 cm [15]. When filled with urine, the bladder becomes more spherical. The boundary conditions for the contact of the bladder with the structures depends on the rate of the bladder filling [11]. Figure 4 shows the regions near the human urinary bladder. Based upon the physiological diagram shown in Figure 4, the boundary conditions can be applied to the bladder model. However, during the preliminary analysis not all of them were applied to the model.

The material properties of the bladder tissue are assumed to be homogenous and continuous [11]. Most of the research to identify the mechanical properties of the bladder is performed by Dahms *et al.* and are shown in Table 1 [16].

Table 1: Material properties of bladder tissue for different mammals [16]

| Material | No. of specimens | Ultimate tensile strain (mm/mm) | Ultimate tensile strength (MPa) | Elastic Modulus (MPa) |
|----------------------|-------------------------|--|--|------------------------------|
| Rat bladder | 10 | 2.03 | 0.72 | 0.76 |
| Pig bladder | 10 | 1.66 | 0.32 | 0.26 |
| Human bladder | 10 | 0.69 | 0.69 | 0.25 |

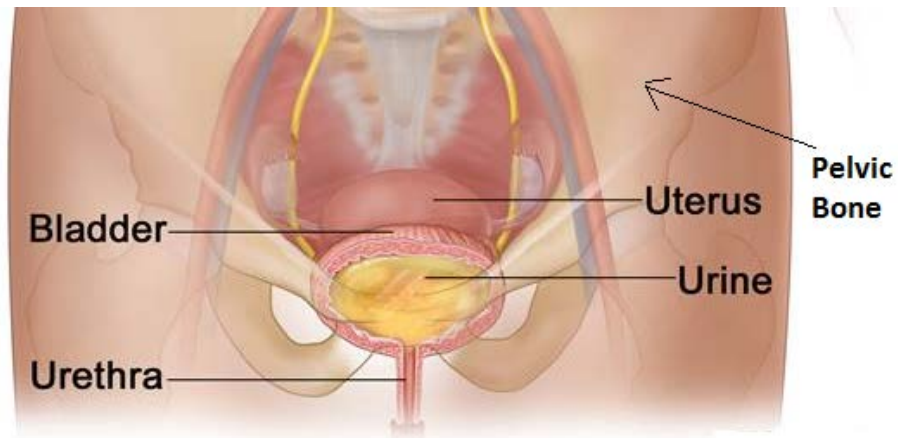


Figure 4: Anatomical regions that will be used to provide support or boundary condition in finite element analysis [3]

2.3 Cystoscopy and Procedure

The cystoscopy technique was first reported by Rose in 1927 and has been extensively used since then for both clinical and research purposes [10]. Cystoscopy can be termed as an endoscopy of the urinary track. It can be performed either by a flexible or rigid cystoscope device. Cystoscopy can be used either for diagnostic or therapeutic purposes. Advances have been made in cystoscopy with the improvisation of cold light, enhancement of optical system and the development of video endoscopy and flexible instruments [18].

A rigid cystoscope has 3 functional parts: a telescope, bridge and sheath [19]. Figure 5 is a schematic of a rigid cystoscope inserted via the urethra to examine the inner bladder wall. During this procedure, tissue samples can also be collected if needed. However, it was reported by Stav *et al.* that although cystoscopy seemed to be a painful procedure it was well tolerated by most of the patients, but that it may have adverse effect on the sexual life of a patient [7]. Furthermore,

additional research is needed to determine whether screening of adults for bladder cancer leads to better outcomes [20].

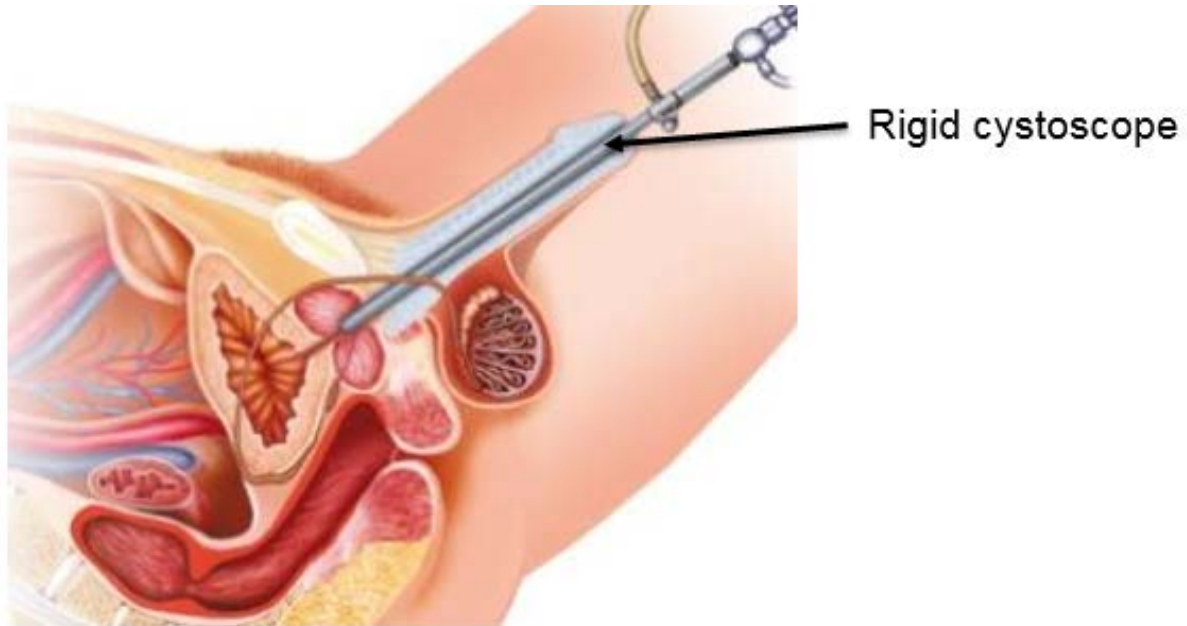


Figure 5: Rigid cystoscopy to examine the inner bladder wall [21]

In this research, a procedure for inserting the proposed device in the urethra for measuring bladder tissue properties similar to rigid cystoscopy will be adopted. Upon reaching the bladder, the instrument will be actuated to capture proper measurements from the bladder tissue.

2.4 FEA Approximation of the Human Bladder

2.4.1 Tissue Properties

The final bladder model will have the properties and the subsequent assumptions as in the research performed by Beek *et al* [11]. The bladder is assumed to be thick walled and hollow in shape. The material behavior is assumed to be incompressible, isotropic and nonlinear elastic [11].

A survey of published literature demonstrated that most soft human tissues have viscoelastic properties [22] [23] [24]. However, to simplify mathematical modeling, it is safe to assume that the bladder tissue behavior is hyperelastic in nature [25]. The material parameters were obtained from various peer reviewed sources, and the results were compared based upon the relationship of stress as a function of strain or elongation. This mean set of result closely resembled to the work performed by Yamada *et. al.* [26]. The data will be used in various mathematical models such as the Mooney-Rivlin or Yeho's, Ogden's, polynomial, Arudda-Boyce. The model does not provide extra insight over the input data, instead, it is a polynomial approximation for material property for which the specific model will be used.

The tissue will be modeled as a hyperelastic material, therefore, the material properties considered are limited to the loading conditions only and unloading conditions are disregarded. Typically, to model a hyperelastic material, a strain energy function is used to relate the stress and strain tensors [22]. Many forms of strain energy functions are available in the analysis software. Mullins effect is characterized by a decrease in material stiffness during loading and can be recognized by cyclic loading. The Mullins effect of damage was not considered while modeling the bladder tissue as there were no cyclic loading.

According to Martins, it is assessed that the modulus of elasticity of the human bladder from female cadaver ranged from 1 MPa to 4.1 MPa [27]. These values were obtained from 13 female cadavers with no pelvic floor dysfunctions. The results were obtained after performing uniaxial tensile tests on the bladder tissue. Also, the results from Hwang *et al.* and Rubod *et al.*, were examined to indicate that the stress-strain graphs closely resemble each other [25] [28]. Figure 6 presents the comparison plots of the stress-strain data for the pelvic organ obtained

from Bush *et al.* and Yamada *et al.* [22]. This data will be used as input for the material properties to model the bladder tissue as a hyperelastic material.

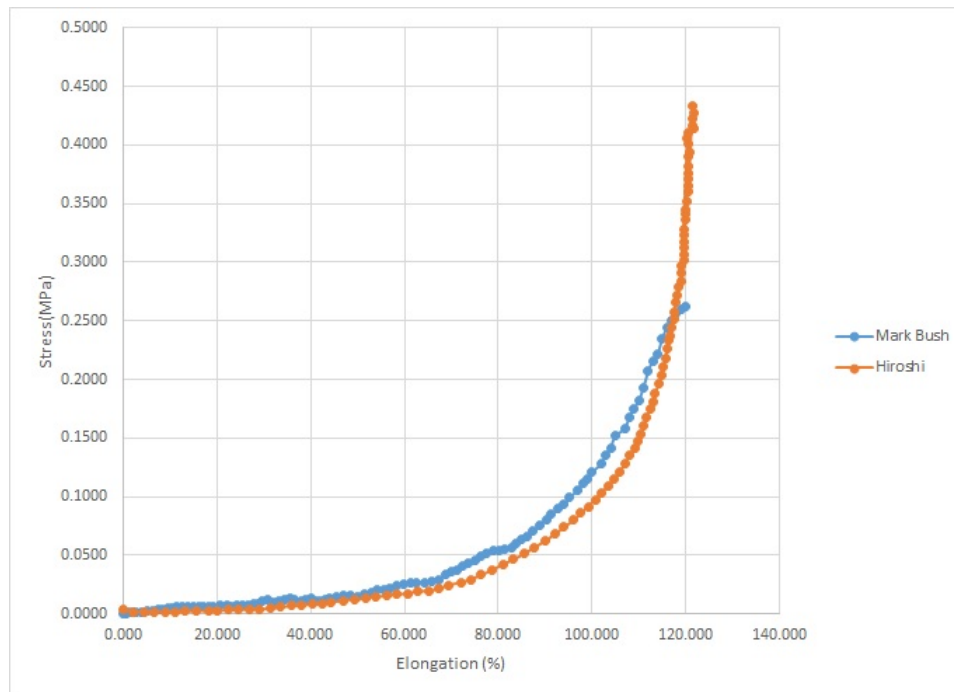


Figure 6: Experimental stress as a function of elongation for urinary bladder evaluated by Bush *et al.* and Yamada *et al.* [22] [26]

2.4.2 Tissue Mathematical Modelling

The tissue is composed of various biological components which form a fluid matrix. The theory of continuum mechanics in ANSYS Workbench 17.0 to model the bladder properties is used because the biological elements are relatively small and the mechanical variations are usually only significant at the microscopic scale [11]. Early models that characterized the mechanics of the bladder were presented in the 1970s [24] [30]. The Mooney models are popular for modeling the moderate strain nonlinear behavior of incompressible materials [11]. It's important to

understand that these models, similar to Mooney, Mooney-Rivlin, Yeoh's, Polynomial, Ogden and Arudda-Boyce models do not give any special insight into material behavior [31]. The numerical values of coefficients resulting from the regression analysis are used in a FEA program for mechanical analysis. The strain energy function for a Mooney-Rivlin model is evaluated as in Equation (1) [32].

$$W = \sum_i \sum_j C_{ij} (I_1 - 3)^i (I_2 - 3)^j + D(J - 1)^2 \quad \text{Equation (1)}$$

Where, $I_1 = \lambda_1^2 + \lambda_2^2 + \lambda_3^2$ and $I_2 = \left(\frac{1}{\lambda_1^2} + \frac{1}{\lambda_2^2} + \frac{1}{\lambda_3^2}\right)$. In Equation (1), I_1 and I_2 are the strain invariants which are functions of λ_1, λ_2 and λ_3 the principle stretch ratios, W is the strain energy function, C_{ij} are constants evaluated from regression analysis, D is also a constant evaluated from regression analysis, J is the Jacobian. Similarly, Yeoh developed a hyperelastic material model that depended on the first strain invariant only. The strain energy function for Yeoh's model is provided in Equation (2) [33].

$$W = \sum_{i=1}^n C_i \cdot (I_1 - 3)^i \quad \text{Equation (2)}$$

Where, W is the strain energy function, C_i is the evaluated constant from regression analysis, and I_1 is the first strain invariant. In typical hyperelastic models, the strain energy function, W is used to relate the strains in differential form. For this research two models were compared and the one having best fit to the experimental data is used. Experimental, uniaxial stress-strain data from Yamada *et al.* were used [22]. These stress-strain data points were provided as input in the Mooney-Rivlin 3 parameter and Yeoh 3rd order in ANSYS Workbench 17.0

hyperelastic regression analysis. These were then used to generate coefficients for the material properties for the expected tissue behavior. Selecting a right model will be determined by selecting a good curve fit and a good curve fit can be defined by considering a domain of deformation. The models are based on the strain invariant or stretch ratio [23]. Figure 7 is a comparison plot of the experimental data obtained from Yamada *et al.* and regression curve generated for the Yeoh 3rd order model evaluated by ANSYS Workbench 17.0 [26]. The blue data points are the experimental data. The curve fit generated by ANSYS Workbench 17.0 are as follows; red continuous line is the expected regression curve for the biaxial stress as a function of strain, green continuous curve is the expected regression curve for the shear stress as a function of strain and blue continuous line is the uniaxial stress as a function of strain given the uniaxial input data points. Comparing the plots for Mooney-Rivlin 3 parameters and Yeoh's 3rd order, it was determined that the Yeoh 3rd order model has a curve fit that more closely resembles the actual experimental data. The regression analysis from ANSYS Workbench 17.0 yielded the material property constants for Yeoh's 3rd order model as presented in Table 2.

Table 2: Yeoh's 3rd order parameter constants for bladder analysis

| Coefficient | Property Constants (MPa) |
|--------------------|---------------------------------|
| C_{10} | 0.00831 |
| C_{20} | -0.00355 |
| C_{30} | 0.00347 |

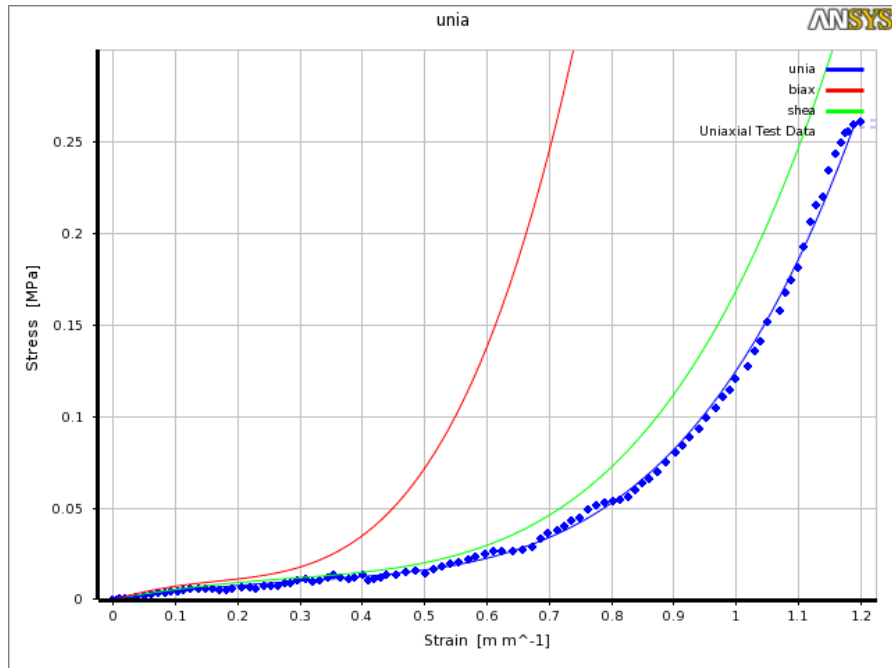


Figure 7: ANSYS Workbench 17.0 regression curve fit for stress as a function of strain for experimental data obtained by Yamada *et al.*

To analyze the deformation as a function of applied load, the constants obtained from Table 2 were used. The analysis settings were manually selected so that convergence issues could be avoided. Therefore, it is important to increment the load in small steps. Automatic meshing is defined. In addition, the relevance number is adjusted from 0 to 100, however, the relevance center is kept unchanged. This setting helped for automatic global refinement of the mesh. All the remaining values for meshing are accepted as default. The analysis settings for the Yeoh model are tuned by trial and error method for the initial substeps, minimum substeps, and maximum substeps as 50, 50, and 1000 steps respectively. The bladder is a viscoelastic material (hyperelastic assumption), and the solver control settings were such that large deflections were

allowed and weak springs were neglected. Additionally, a direct solver is used to solve for this model.

According to Zimmern *et al.* it is ideal to have a tissue displacement of 3 mm to identify properties of soft tissue [8]. Preliminary analysis revealed that applying a pressure of 0.01 MPa resulted in a tissue displacement of approximately 6 mm. A maximum pressure of 0.01 MPa is applied with small sub-steps. The pressure is applied on a circular surface area of diameter 4 mm on the inner surface of the bladder model. The surface of the bladder is allowed to move freely. The other boundary conditions due to the pelvic bone were not considered during initial stages of the bladder model. Internal bladder pressure in healthy subjects is approximated as 60 cm H₂O (~0.0058 MPa), however during the initial finite element modeling of the bladder this internal pressure was neglected [22]. The 4 mm projection on the bladder wall model is rendered to resemble the pressure applied by the instrument. Rigid body motions were suppressed while performing this analysis. Only the coronal ventral view of the bladder is modeled. The bladder is assumed thick-walled sphere similar to the research performed by Beek [11]. The mechanical properties of the wall of the bladder were assumed to be isotropic in nature. The bladder is supported along the urethra, while the other edges could move only in the radial directions. The dynamics of the urethra were not considered in this research because they play a role only during musculature of the internal and external sphincters. Figure 8 shows the applied boundary conditions along with hex-dominant meshing method. One eighth section of the sphere was modeled similar to the work performed by Beek *et al* [11]. A fixed support at A and C as marked in Figure 8. Figure 9 shows the results obtained by applying the loading and boundary conditions as discussed in Figure 8. It was estimated that applying a normal pressure of 0.01 MPa

which is equivalent to a load of 0.1 N displaces the tissue approximately by 6.4 mm. Therefore the device must be designed considering a minimum load of 0.4 N acting at the tip which is equivalent to an applied pressure of 0.03 MPa. For designing the device an applied load of 1 N which accounts for a factor of safety of 2.5 will be used.

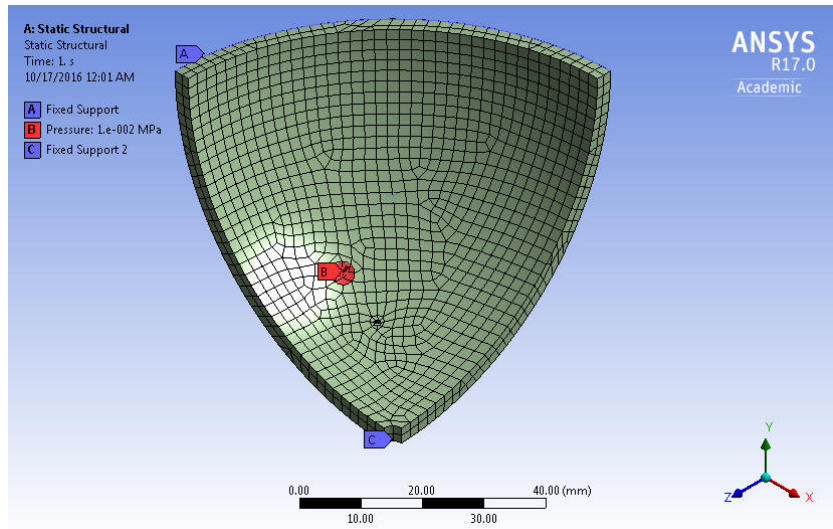


Figure 8: ANSYS Workbench 17.0 bladder model boundary condition

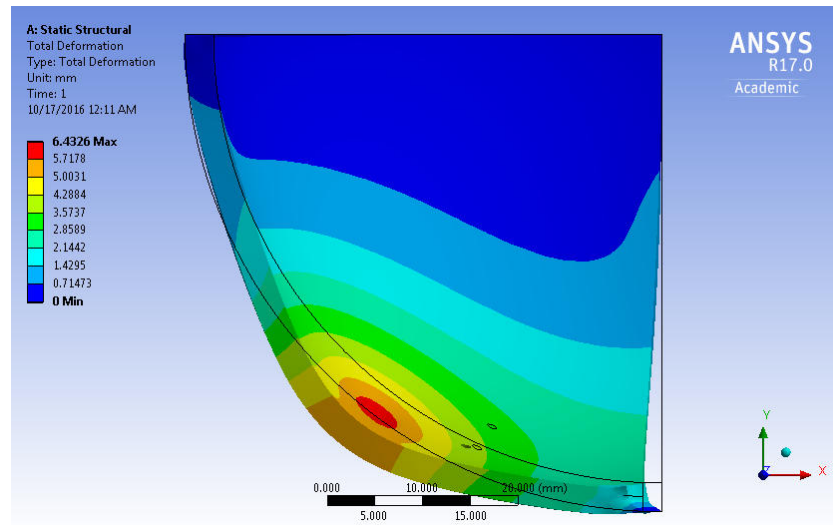


Figure 9: Deformation of bladder tissue on applied load of 0.01 MPa

Chapter 3

Diagnostic Robotic Device and Sensor Design

3.1 Robotic Device Design

3.1.1 Introduction

The goal of this thesis is to design and prototype a device which will enable a physician to evaluate biomechanical properties of the bladder tissue as a function of applied displacement. Thus, the physician will have quantitative data rather than qualitative data alone, as is traditionally the case. Evaluated material properties of soft tissues will be used as a part of diagnostics tests [34]. Due to the high recurrence rate in bladder cancer, patients are asked to undergo frequent inspection after the removal of a bladder tumor, and this inspection is reliably performed using cystoscopy [35]. However, it was reported that the cystoscope needed to be manipulated manually to view larger regions of the bladder, which made it important to have a flexible cystoscope [35]. This conclusion further demonstrates the need of a diagnostic device to be able to manipulate inside the bladder, without manipulating the urethra.

Various approaches were considered to achieve the final design of the device, to be used to probe the inner bladder wall. The initial design was to develop a soft robotic manipulator. Soft robots have a wide scope in the field of medical applications. Kim *et al.* mentioned that soft robots can be developed for medical interventions similar to diagnosis [36]. However, soft robots have a disadvantage when applied to diagnostic devices which is creating a fully soft robot that can move and modulate its body stiffness [36]. The design of continuum robotics started in the 1960s by the creation of serpentine robots. These were built using several closely spaced joints to simulate the backbone of a snake. Prominent research has been performed in the field of

continuum robots by Webster *et al.* [37] [38] [39] [40]. Continuum robots are candidates for this application, however, achieving the desired bend angle in addition to maintaining the stiffness of the robotic tube will be a great challenge. The high stiffness of the robotic device is desired for minimum error while measuring the tissue reaction force. Section 3.1.2 will discuss the strategy and a design approach in the development of the proposed diagnostic device. The details of the rigid link manipulator design will also be discussed and analyzed in Section 0 and Section 0.

3.1.2 Concentric Tube Robot

During the initial stage of research, the design approach was to use concentric tube robots similar to the research performed by Dupont *et al.* [41]. This type of robot was chosen because of the design constraints focus on the diameter of the tubes, which is important in the current research. A concentric tube robot is composed of various telescopic tubes. The stiffness of the inner tube is greater than the stiffness of the outer tube. The shape that can be achieved using concentric tubes is determined by the curvature, stiffness and length of the individual tubes. The telescopic principle differentiates the motion of each tube compared to the other. The principle can be achieved using follow-the-leader fashion, which will automatically avoid the lateral forces on the tubes.

Apart from the theoretical model of a tube inside a tube, the tubes are designed such that each section has either a fixed or variable curvature [42], [43]. Figure 10 is schematic for a concentric tube manipulator, used for vitreoretinal surgeries [42]. However upon further investigation, it was concluded that the concentric tube device will not be able to reach the area of interest in the bladder, which is the trigone, and apply load on the tissue. Therefore, using a

concentric tube robot will introduce greater hardships to apply and measure the reaction force in the desired area.

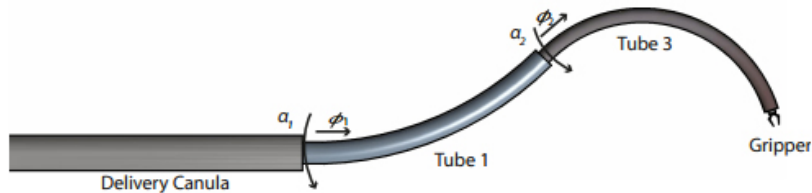
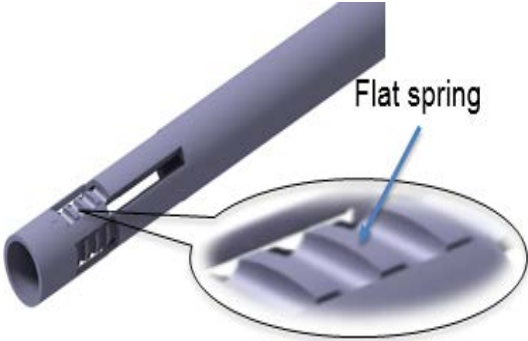




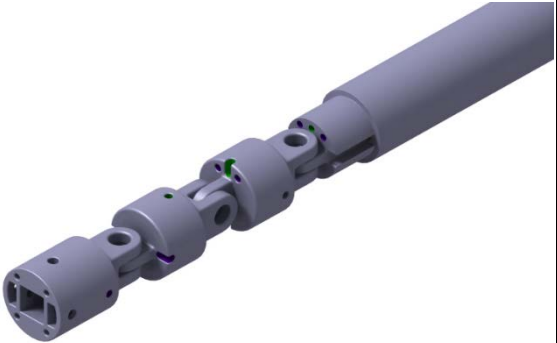
Figure 10: A concentric tube robot comprising of 3 tubes [42]

3.1.3 Rigid Link Manipulator: Design Iterations

The focus of research is to design a miniature device that will not only reach and inspect the inner bladder wall but will also be able to manipulate inside the bladder and probe the bladder tissue especially the trigone region to measure the tissue reaction forces. The design constraints were cognate to maximum allowable diameter of 3 mm, manipulate inside the bladder, probe the inner bladder tissue and measure the tissue reaction force. Various design iterations were performed. Table 3 describes the advantages and disadvantages of each design iteration. Each modification is an improved version and was based upon the limitations of the previous design.

Table 3: Design iterations

| Design Iteration Number | Device Model | Advantages | Disadvantages |
|-------------------------|---|---|---|
| 1 |  | <ul style="list-style-type: none"> • Max. outer diameter 3mm • Rigid Links • Easy to actuate • Manipulating components inside the device itself | <ul style="list-style-type: none"> • Very high stresses in the flat springs • Cannot reach the trigone area, due to design limitations • Will not be able to withstand reaction forces based on preliminary analysis • Manufacturing constraints for flat springs |
| 2 |  | <ul style="list-style-type: none"> • Max. outer diameter 3mm • Easy to actuate • Manipulation in circular workspace | <ul style="list-style-type: none"> • Cannot reach the trigone area, due to 1 DOF • Will not be able to withstand reaction forces based on preliminary analysis |

| | | | |
|---|--|---|--|
| 3 |  | <ul style="list-style-type: none"> • Can access the trigone area of bladder • Manipulation in spherical workspace • Easy to manufacture | <ul style="list-style-type: none"> • Anchoring of the actuating tendons overrules max diameter constraint • Attachment for the sensor not provided |
| 4 |  | <ul style="list-style-type: none"> • Can access the trigone area of bladder • Manipulation in spherical workspace • Sensor attachment provided | <ul style="list-style-type: none"> • Anchoring of the actuating tendons overrules max diameter constraint |

3.1.4 Rigid Link Manipulator: Proposed Design

This design proposed with rigid link connections. An important constraint to consider was that the outer diameter of the device should not exceed 3 mm. The design concept used five components using a bottom-up design approach, where the simple system will build up to an assembly. A summary and description of each component of the assembly is discussed. Although the design of the device was within the specifications the outer tube of the proposed design had an outer diameter of 3.5 mm, which was considered to be in the acceptable range. Figure 11 is the assembly of the proposed robotic device, each component of this assembly will be discussed.

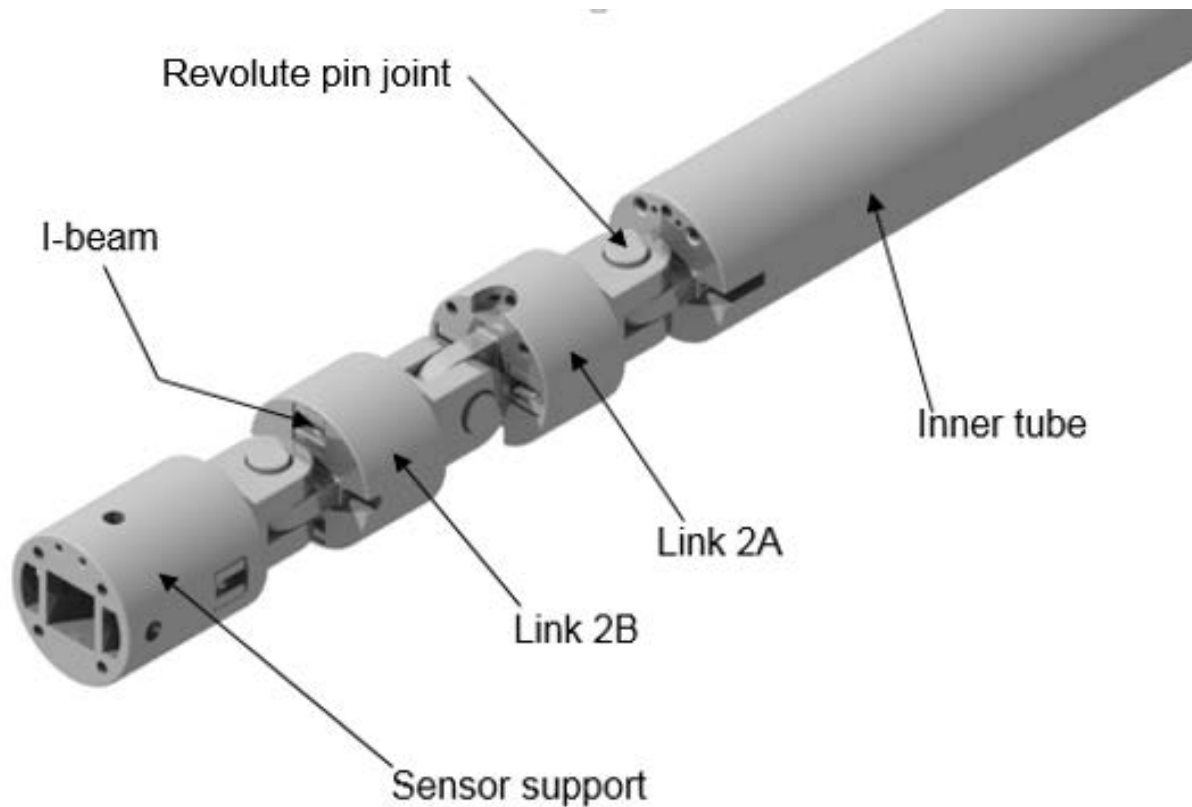


Figure 11: Proposed Robotic device assembly

Outer Tube: The outer tube was designed with an outer diameter (OD) of 3.5 mm and an inner diameter (ID) of 3.2 mm. The length of the tube in the design was 200 mm. The outer hollow tube supports the inner tube and the links connected to the inner tube. This tube will remain stationary once it is inserted in the urinary tract and reach the inner bladder. It will act as a guide for the robotic device to reach the bladder.

Inner tube: The inner tube was designed so that it can go through the outer tube and provide support to the other parts that will actuate inside the bladder to access the area of interest. The design model presented in Figure 12 can be used to examine the front view of the inner tube having several channels. These channels provide a pathway for the actuation tendons

and data-transmitting wires or sensor cables. The diameter of these channels were constrained at 0.27 mm and 0.15 mm respectively. The reason being that the outer diameter of the actuation tendon is 0.25 mm and sensor wire is 0.1 mm. An extrusion was provided on this component which will help to accommodate a revolute joint. The part drawing is attached in Appendix A.1

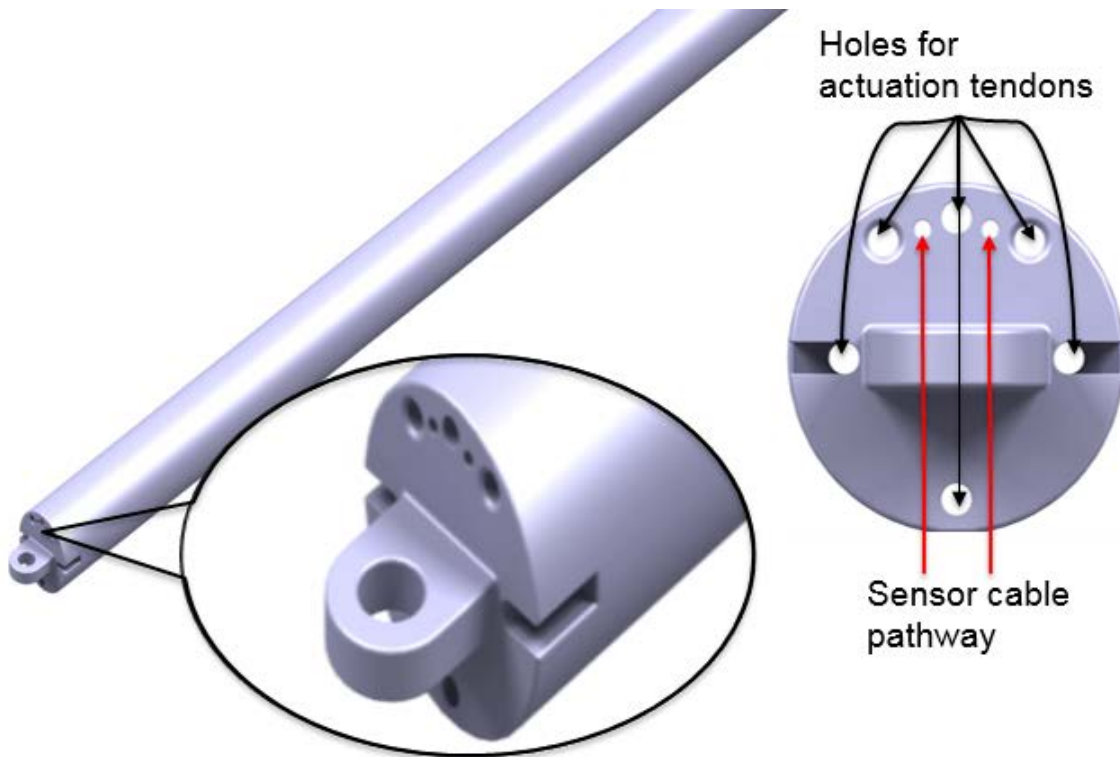


Figure 12: Rigid link manipulator: inner tube with detailed front view

I-Beam: I-beams will be used to anchor the tendons by press fitting them into the slots provided in the components; link 2A, link 2B and sensor assembly support of the rigid link manipulator. Failure analysis of the I-beam was performed. Failure of the I-beam will ultimately

lead to the failure of the actuation mechanism, hence this component was critical in designing the device. Figure 13 represents the tendon pull direction of the proposed I-beam model

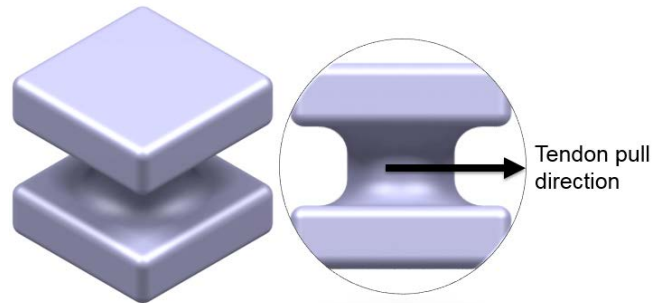


Figure 13: I-beam model to anchor the tendons

Link 2A: This link was connected to the inner tube with a pin revolute joint. The length of this link was initially chosen to be 1.5 mm. However, due to manufacturing constraints to perform machining operations, it was suggested to increase the length of this part to 2 mm. A tendon will be anchored to the I-beams which will be inserted in the two cubic slots as shown in Figure 14. Thus, the rotation of the joint can be achieved by pulling the tendon anchored to the I-beam at each side. Figure 14 also represents the guideways for the actuation tendons for joint 2 and joint 3 marked in blue arrows and channel for the sensor cable marked in red arrow. The drawing of the part is attached in Appendix A.2.

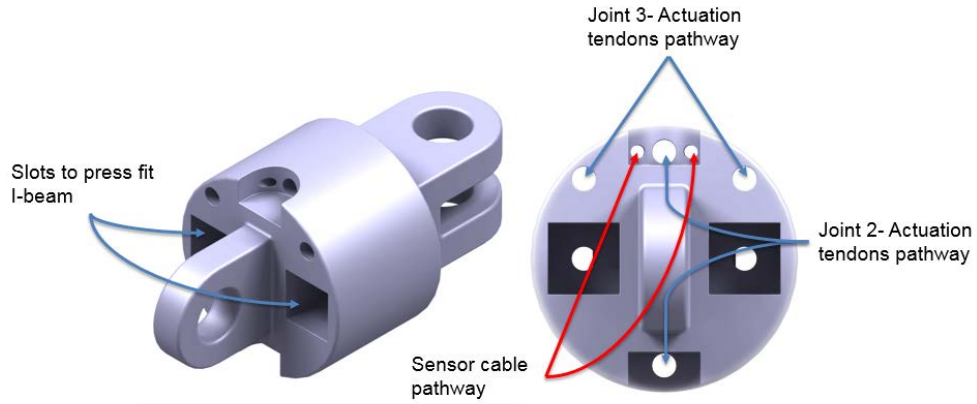


Figure 14: Rigid link manipulator: link 2A

Link 2B: Link 2B was similar to link 2A, except that link 2B does not have the same number of channels as link 2A because two channels were utilized to anchor the I-beam for link 2A which is not needed, anymore. The schematic for this link is as in Figure 15. The two slots provided on the front face of the link are for the I-beams, which will anchor the actuation tendons and press fit in those slots. The red arrow in Figure 15 indicates the sensor cable channel. The drawing of the part is attached in Appendix A.3.

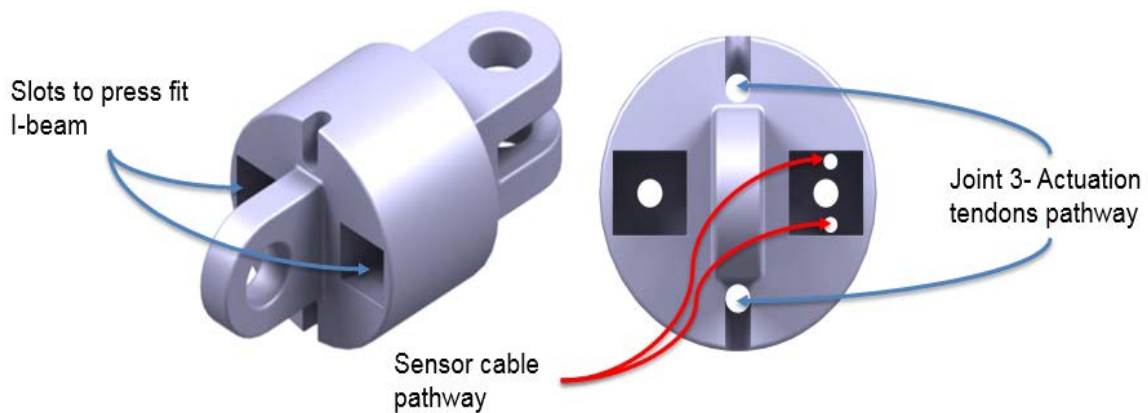


Figure 15: Rigid link manipulator: link 2B

Sensor assembly support: Figure 16 is the CAD model for sensor support component. The sensor support, which can also be termed as end effector support, will be the last link in the manipulator. The sensor support part was designed in a way that it could provide dual functionality. First it provides one degree of freedom to the device. Second, attaching and detaching of the sensor assembly can be performed easily. Equivalent to other links, the maximum diameter of this part must not exceed 3 mm. The cubical slot provided on the front face was for attaching the base of the sensor assembly, whereas the small rectangular pair of slots on the same face function as a guide for the sensor head which will be reviewed in detail in Section 3.2.1. Slots are provided on each side of this part to press fit the I-beams, which will assist in actuation of the sensor support component. The drawing of the part is attached in Appendix A.4.

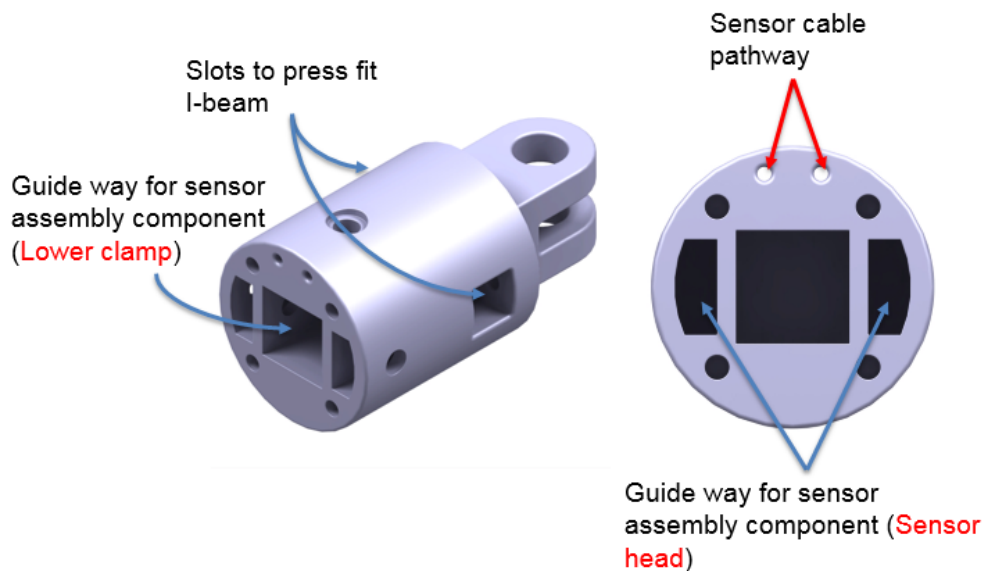


Figure 16: Rigid link manipulator: sensor support

A scaled model of the device as presented in Figure 17 (5 times scale) was manufactured using Acrylonitrile Butadiene Styrene (ABS) material in an in-house 3D printer, to examine the

motion of the joints as a conceptual verification [44]. Microfilament braided line were used as tendons to actuate the joints on scaled prototype.

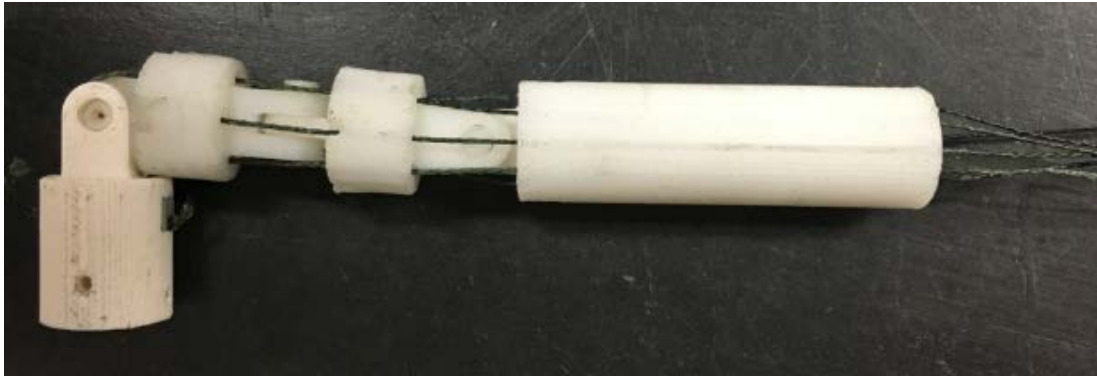


Figure 17: A 5 times scaled prototype for verification of the concept of design

3.1.5 Analysis of Rigid Link Manipulator

This section discusses the forward and inverse kinematics of the device. Static force analysis and finite element analysis for each component will also be discussed. Kinematic analysis was performed to locate the sensor tip position with respect to the base position of the device. To perform this analysis, a relationship was developed to locate the position and orientation of the tip of the sensor [45].

The design will have rigid link connections and the revolute joints will have joint angles which will be joint variables in the analysis. As presented in Figure 11, the device is a 3 degree of freedom mechanism, and the arrangement of the joints is equivalent to a spherical joint. From this point, the design of the manipulator will be considered as a set of links connected in a chain by revolute joints. To position and orient the sensor tip in 3D space, a minimum of 6 degrees of freedom is required [45]. Inverse kinematics was used to evaluate the position of the tip of the

sensor with respect to the base frame for the proposed 3 degree of freedom manipulator. At this stage of research it was sufficient to account for the position of the tip of the device, hence 3 DOF.

3.1.6 Kinematic Analysis

A methodology is followed to develop the relation between the position and orientation of the sensor tip inside the bladder with respect to the base frame of the tube held by the physician using the modified Denavit-Hartenberg (DH) notation. The definition of DH variables in the modified DH table are as follows, a_i is the distance from Z_i to Z_{i+1} along X_i , α_i is the angle from Z_i to Z_{i+1} about X_i , d_i is the distance from X_i to X_{i+1} along Z_{i+1} and θ_i is the angle from X_i to X_{i+1} about Z_{i+1} [45].

Performing the forward kinematics will identify the location and orientation of the sensor tip in 3D space. However analyzing inverse kinematics will assist to gain just the position of the last frame with respect to the base frame. Figure 18 shows the frame assignment for the base, tip and joints of the proposed robotic device. All frames rotate or translate with the joints unless specifically mentioned. A parametric relationship was developed from the base frame to the sensor tip. A homogenous transformation matrix fully defines the relationship between any two frames of interest. Table 4 presents the joint and MDH parameters that were used for the kinematic analysis of the device.

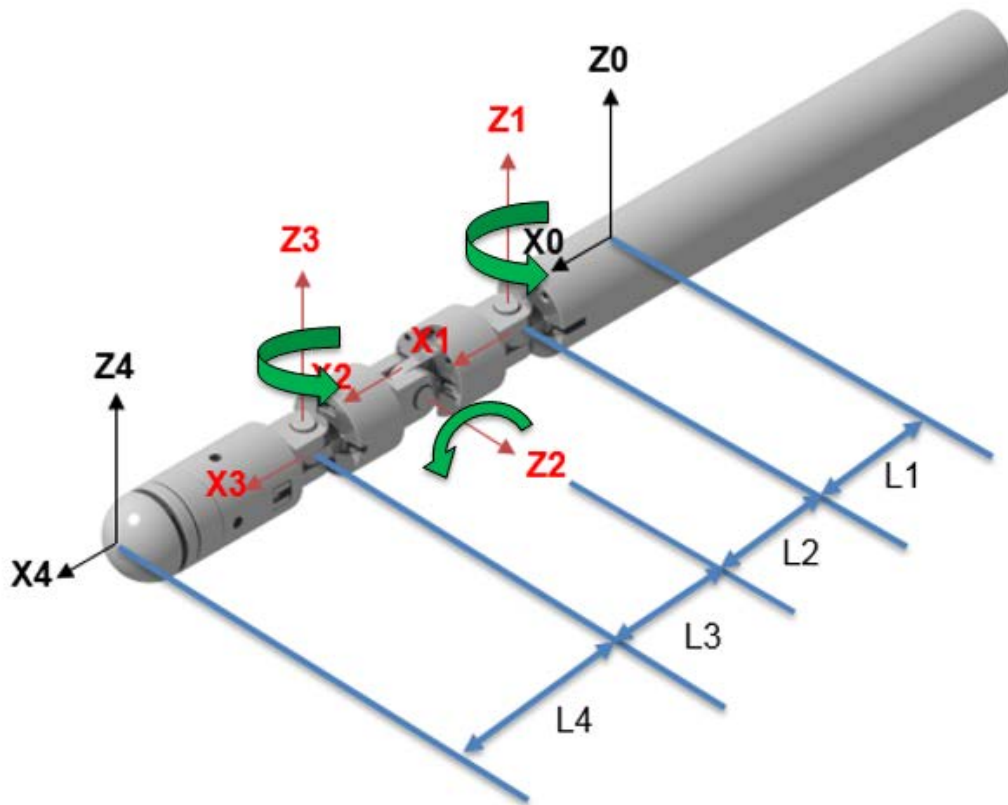


Figure 18: Frame assignment for kinematic analysis

Table 4: MDH parameters for the manipulator

| FRAME | | JOINT | | | MDH PARAMETERS | | | |
|-------------|----------|--------|------|------------|----------------|----------------|--------|----------------|
| Current (C) | Next (N) | Number | Type | Variable | a (mm) | α (rad) | d (mm) | θ (rad) |
| 0 | 1 | 1 | R | θ_1 | L1 | 0 | 0 | θ_1 |
| 1 | 2 | 2 | R | θ_2 | L2 | $3\pi/2$ | 0 | θ_2 |
| 2 | 3 | 3 | R | θ_3 | L3 | $\pi/2$ | 0 | θ_3 |
| 3 | 4 | - | - | - | L4 | 0 | 0 | 0 |

Here L_1 is the length from the base frame to the first joint of the device the base frame can be adjusted with respect to the patient, L_2 and L_3 are the link lengths from previous joint to next joint and L_4 is the length from the last joint to the sensor tip. The generalized relationship between two frames was generated according to Equation (3) where the entries of the matrix were the function of the parameters in the MDH table [45].

$$T_N^C = \begin{bmatrix} \cos(\theta_N) & -\sin(\theta_N) & 0 & a_C \\ \sin(\theta_N) \cos(\alpha_C) & \cos(\theta_N) \cos(\alpha_C) & -\sin(\alpha_C) & -\sin(\alpha_C) \cdot d_N \\ \sin(\theta_N) \sin(\alpha_C) & \cos(\theta_N) \sin(\alpha_C) & \cos(\alpha_C) & \cos(\alpha_C) \cdot d_N \\ 0 & 0 & 0 & 1 \end{bmatrix} \quad \text{Equation (3)}$$

In the transformation matrix as shown in Figure 19 the 3 x 3 matrix, represents the orientation of the next frame with respect to the current frame. The first three rows of the 4th column as shows in Figure 19, represent the position vector of the origin of the next frame with respect to the previous frame. The input parameters as presented in Table 4, were used to evaluate the homogenous transformation matrix for each joint to obtain the location and orientation of the next (N) frame as referred from the current (C) frame. The individual homogenous transformation matrices was evaluated from a generalized code that was developed using MATLAB R2016a. The code is attached in Appendix B. As a first step towards verification of the forward kinematics analysis, the joint variables were assumed to be zero. The resulting position vector yielded the summation of the link length. Likewise, arbitrary values of joint angles were selected to verify if the device reaches the trigone area. This will be discussed in Section 4.1.1. The parametric relationship obtained for each joint is evaluated in Equation (4), Equation (5), Equation (6) and Equation (7).

$$T_N^C = \begin{bmatrix} \cos(\theta_N) & -\sin(\theta_N) & 0 & 0 \\ \sin(\theta_N) \cos(\alpha_C) & \cos(\theta_N) \cos(\alpha_C) & -\sin(\alpha_C) & -\sin(\alpha_C) \cdot d_N \\ \sin(\theta_N) \sin(\alpha_C) & \cos(\theta_N) \sin(\alpha_C) & \cos(\alpha_C) & \cos(\alpha_C) \cdot d_N \end{bmatrix}$$

Figure 19: Significance of homogenous transformation matrix

$$H_1^0 = \begin{bmatrix} \cos(\theta_1) & -\sin(\theta_1) & 0 & L_1 \\ \sin(\theta_1) & \cos(\theta_1) & 0 & 0 \\ 0 & 0 & 1 & 0 \\ 0 & 0 & 0 & 1 \end{bmatrix} \quad \text{Equation (4)}$$

$$H_2^1 = \begin{bmatrix} \cos(\theta_2) & -\sin(\theta_2) & 0 & L_2 \\ 0 & 0 & 1 & 0 \\ -\sin(\theta_2) & -\cos(\theta_2) & 0 & 0 \\ 0 & 0 & 0 & 1 \end{bmatrix} \quad \text{Equation (5)}$$

$$H_3^2 = \begin{bmatrix} \cos(\theta_3) & -\sin(\theta_3) & 0 & L_3 \\ 0 & 0 & -1 & 0 \\ \sin(\theta_3) & \cos(\theta_3) & 0 & 0 \\ 0 & 0 & 0 & 1 \end{bmatrix} \quad \text{Equation (6)}$$

$$H_4^3 = \begin{bmatrix} 1 & 0 & 0 & L_4 \\ 0 & 1 & 0 & 0 \\ 0 & 0 & 1 & 0 \\ 0 & 0 & 0 & 1 \end{bmatrix} \quad \text{Equation (7)}$$

Therefore, it was possible to relate the location of Frame 4 with respect to Frame 0 by multiplying the homogenous transformation matrices and obtain the final homogenous transformation matrix as presented in Equation (8) [45].

$$H_4^0 = H_1^0 \cdot H_2^1 \cdot H_3^2 \cdot H_4^3 = \begin{bmatrix} n_x & o_x & a_x & p_x \\ n_y & o_y & a_y & p_y \\ n_z & o_z & a_z & p_z \\ 0 & 0 & 0 & 1 \end{bmatrix} \quad \text{Equation (8)}$$

Where,

$$n_x = \cos(\theta_1) \cdot \cos(\theta_2) \cdot \cos(\theta_3) - \sin(\theta_1) \cdot \sin(\theta_3),$$

$$n_y = \cos(\theta_1) \cdot \sin(\theta_3) + \cos(\theta_2) \cdot \cos(\theta_3) \cdot \sin(\theta_1),$$

$$n_z = \cos(\theta_3) \cdot \sin(\theta_2),$$

$$o_x = -\cos(\theta_3) \cdot \sin(\theta_1) - \cos(\theta_1) \cdot \cos(\theta_2) \cdot \sin(\theta_3),$$

$$o_y = \cos(\theta_1) \cdot \cos(\theta_3) - \cos(\theta_2) \cdot \sin(\theta_1) \cdot \sin(\theta_3),$$

$$o_z = \sin(\theta_2) \cdot \sin(\theta_3),$$

$$a_x = \cos(\theta_1) \cdot \sin(\theta_2),$$

$$a_y = \sin(\theta_1) \cdot \sin(\theta_2),$$

$$a_z = \cos(\theta_2),$$

$$p_x = L_1 - L_4 \cdot (\sin(\theta_1) \cdot \sin(\theta_3) - \cos(\theta_1) \cdot \cos(\theta_2) \cdot \cos(\theta_3)) + L_2 \cdot \cos(\theta_1) \\ + L_3 \cdot \cos(\theta_1) \cdot \cos(\theta_2),$$

$$p_y = L_4 \cdot (\cos(\theta_1) \cdot \sin(\theta_3) + \cos(\theta_2) \cdot \cos(\theta_3) \cdot \sin(\theta_1)) + L_2 \cdot \sin(\theta_1) \\ + L_3 \cdot \cos(\theta_2) \cdot \sin(\theta_1),$$

$$p_z = -\sin(\theta_2) \cdot (L_3 + L_4 \cdot \cos(\theta_3)).$$

The forward kinematic equations identifies the orientation and position of the tip of the sensor with respect to the 0th Frame (base frame).

Inverse kinematics is a procedure which will serve as a tool to estimate the joint angles from the desired homogeneous transformation matrix. A method to perform inverse kinematics is, to formulate the equations for all the joint angles using the given homogeneous transformation matrix.

The final homogenous matrix, is evaluated from forward kinematics

$$H_4^0 = H_1^0 \cdot H_2^1 \cdot H_3^2 \cdot H_4^3 = H_{des} \quad \text{Equation (9)}$$

In inverse kinematics, H_{des} is a given matrix, therefore it is called as desired matrix. Matrix operations are performed to estimate the values for the joint angles.

$$H_{des} = \begin{bmatrix} n_x & o_x & a_x & p_x \\ n_y & o_y & a_y & p_y \\ n_z & o_z & a_z & p_z \\ 0 & 0 & 0 & 1 \end{bmatrix} \quad \text{Equation (10)}$$

Based on the preliminary analysis performed to solve for the joint variables n_x, n_y, n_z, o_x, o_z and p_y from the homogeneous transformation matrix is required. It was analyzed that by using only position vector it was not possible to achieve a closed form solution. The method to analyze the inverse kinematics uses the orientation matrix to obtain the joint variables. Equating the sum of the square on the left-hand side to the right-hand side for 3rd row, 1st column and 3rd row, 2nd column yields,

$$\{H_4^0(3,1)\}^2 + \{H_4^0(3,2)\}^2 = \{H_{des}(3,1)\}^2 + \{H_{des}(3,2)\}^2$$

$$\sin^2(\theta_2) = n_z^2 + o_z^2 \quad \text{Equation (11)}$$

$$\cos(\theta_2) = \pm\sqrt{1 - \sin^2(\theta_2)} \quad \text{Equation (12)}$$

Solving for θ_2 ,

$$\theta_2 = \text{atan2}\left(\pm\sqrt{n_z^2 + o_z^2}, \pm\sqrt{1 - (n_z^2 + o_z^2)}\right) \quad \text{Equation (13)}$$

In order to determine the quadrant of the joint angle, atan2 function is used in Equation (13) [46]. Performing the following operation on the desired matrix,

$$H_{des1} = (H_1^0)^{-1} H_{des} = H_2^1 H_3^2$$

$$\text{Comparing, } \{H_3^1(1,1)\}^2 + \{H_3^1(2,1)\}^2 = H_{des1}(1,1)^2 + H_{des1}(2,1)^2$$

$$(n_x)^2 + (n_y)^2 = \cos^2(\theta_2) \cos^2(\theta_3) + \sin^2(\theta_3) \quad \text{Equation (14)}$$

$$\text{Substitute } m = \cos^2(\theta_2) \text{ and } b = (n_x)^2 + (n_y)^2$$

$$m \cdot \cos^2(\theta_3) + \sin^2(\theta_3) = b \quad \text{Equation (15)}$$

$$m \cdot \cos^2(\theta_3) + (1 - \cos^2(\theta_3)) = b \quad \text{Equation (16)}$$

$$\cos^2(\theta_3)(m - 1) = (b - 1) \quad \text{Equation (17)}$$

$$\cos^2(\theta_3) = \frac{(b - 1)}{(m - 1)} \dots \left(\text{here } m \neq 1 \text{ also } -1 \leq \frac{(b - 1)}{(m - 1)} \leq 1 \right) \quad \text{Equation (18)}$$

$$\sin(\theta_3) = \pm \sqrt{1 - \cos^2(\theta_3)} \quad \text{Equation (19)}$$

On solving for θ_3 , the *atan2* function will be used to identify the quadrant of the angle.

$$\begin{aligned} \theta_3 \\ = \text{atan2} \left(\pm \sqrt{1 - \left(\frac{((n_x)^2 + (n_y)^2 - 1)}{(\cos^2(\theta_2) - 1)} \right)}, \pm \sqrt{\left(\frac{((n_x)^2 + (n_y)^2 - 1)}{(\cos^2(\theta_2) - 1)} \right)} \right) \end{aligned} \quad \text{Equation (20)}$$

If $m = 1$ in Equation (18), then the value of θ_2 is zero. This particular solution yields to singularity to other joint angles, therefore, another approach needs to be provided which will calculate the value for other joint angles when the value for θ_2 is zero.

Approach 2 will be used later to obtain the other joint angles, had the value of θ_2 been zero.

As θ_3 has now been evaluated from Equation (20) considering θ_2 is not equal to zero, the following operations are performed to obtain θ_1 .

$$\text{Comparing } H_3^1(2,2) + H_3^1(1,3) = H_{\text{des1}}(2,2) + H_{\text{des1}}(1,3)$$

$$\cos(\theta_3) + \sin(\theta_2) \quad \text{Equation (21)}$$

$$= o_y \cos(\theta_1) - o_x \sin(\theta_1) + a_x \cos(\theta_1) + a_y \sin(\theta_1)$$

$$\cos(\theta_3) + \sin(\theta_2) = m \cdot \cos(\theta_1) + w \cdot \sin(\theta_1) \quad \text{Equation (22)}$$

$$r = m \cdot \cos(\theta_1) + w \cdot \sin(\theta_1) \quad \text{Equation (23)}$$

Where, $m = (o_y + a_x)$, $w = (a_y - o_x)$, and $r = \cos(\theta_3) + \sin(\theta_2)$,

$$\text{Let } u = \tan\left(\frac{\theta_1}{2}\right)$$

Using the half angle formula, Equation (23) can be solved as

$$\theta_1 = 2 \cdot \operatorname{atan2} \left(\frac{\left((a_y - o_x) \pm \sqrt{\left((a_y - o_x)^2 + (o_y + a_x)^2 - \cos(\theta_3) + \sin^2(\theta_2) \right)} \right)}{(o_y + a_x) + \cos(\theta_3) + \sin(\theta_2)}, 1 \right) \quad \text{Equation (24)}$$

All joint angles are obtained. However, it is assumed that θ_2 is not equal to zero. Approach 2 will evaluate the joint angles in the case that θ_2 is zero. A comparison will be performed by using the position information of the H_{des} matrix, on comparing the right and left-hand side,

$$H_4^0(2,4) - L_4 \cdot H_4^0(2,1) = H_{des}(2,4) - L_4 \cdot H_{des}(2,1)$$

$$(L_2 + L_3)\sin(\theta_1) = (p_y - L_4 \cdot n_y) \quad \text{Equation (25)}$$

$$\sin(\theta_1) = (p_y - L_4 \cdot n_y)/(L_2 + L_3) \quad \text{Equation (26)}$$

$$\cos(\theta_1) = \pm\sqrt{1 - \sin^2(\theta_1)} \quad \text{Equation (27)}$$

$$\theta_1 = \operatorname{atan2} \left(\frac{(p_y - L_4 \cdot n_y)}{(L_2 + L_3)}, \pm\sqrt{1 - \left(\frac{(p_y - L_4 \cdot n_y)}{(L_2 + L_3)} \right)^2} \right) \quad \text{Equation (28)}$$

In Equation (28), $(p_y - L_4 \cdot n_y) \leq (L_2 + L_3)$ after obtaining the value for θ_1 from Equation (28), a comparison on same matrix was performed to obtain θ_3 . Comparing $H_{des}(2,1)$ with $H_4^0(2,1)$

$$\sin(\theta_1 + \theta_3) = n_y \quad \text{Equation (29)}$$

$$\cos(\theta_1 + \theta_3) = \pm\sqrt{1 - \sin^2(\theta_1 + \theta_3)} = \pm\sqrt{1 - (n_y)^2} \quad \text{Equation (30)}$$

$$\theta_3 = \operatorname{atan2} \left(n_y, \pm\sqrt{1 - (n_y)^2} \right) - \theta_1 \quad \text{Equation (31)}$$

A code was developed in MATLAB to evaluate numerical values for the joint angles. This inverse kinematic code is attached in Appendix C. Joint limits were also considered when developing the code. According to the frame assignments and the design of the device the joint limits assigned for each joint was from -90° to 90° . Solution sets for the joint angles are

obtained by performing inverse kinematics. All possible solutions, within the joint limits are selected. Amongst the selected solution sets, the one to consume minimum energy to actuate will be preferred. After the selection of this solution set these values of the joint angles were given as in input in the forward kinematics, to confirm if the sensor tip would indeed reaches the position and orientation defined by the joint angles. Therefore, a procedure was implemented such that the difference from the transformation matrix obtained from the inverse kinematic solution and the desired transformation matrix was zero. The inverse kinematics performed addresses the position of the manipulator tip.

3.1.7 Static Force Analysis

In this section, the limiting torque at the joints were calculated for different configurations to avoid motion at the joints when an external force was applied to the end effector. To obtain static torque as a parametric equation, the rotation matrices are evaluated from the individual homogeneous transformation matrix obtained during forward kinematic formulation. The relationship between Cartesian coordinates and joint variables is developed.

A Jacobian matrix is a multidimensional matrix that relates the Cartesian velocities to the joint quantities of the robot.

$$v^0 = J^0(\theta) \cdot \dot{\theta} \quad \text{Equation (32)}$$

Where, $\dot{\theta}$ is the joint velocity vector, and v^0 is the Cartesian velocity vector at the base frame. The Jacobian matrix, J^0 can be used to find points of singularity, which will determine the workspace boundary singularities. It can also be used to acquire the relationship between the Cartesian force and joint torques. The joint values are the functions of time. Assuming a fixed

base frame, the Jacobian matrix is obtained according to Equation (33), by taking the partial derivatives of the position vectors with respect to joint angles.

$$J^0 = \begin{bmatrix} \frac{\partial P_x}{\partial \theta_1} & \frac{\partial P_x}{\partial \theta_2} & \frac{\partial P_x}{\partial \theta_3} \\ \frac{\partial P_y}{\partial \theta_1} & \frac{\partial P_y}{\partial \theta_2} & \frac{\partial P_y}{\partial \theta_3} \\ \frac{\partial P_z}{\partial \theta_1} & \frac{\partial P_z}{\partial \theta_2} & \frac{\partial P_z}{\partial \theta_3} \end{bmatrix} = \begin{bmatrix} J_{11} & J_{12} & J_{13} \\ J_{21} & J_{22} & J_{23} \\ J_{31} & J_{32} & J_{33} \end{bmatrix} \quad \text{Equation (33)}$$

Where,

$$J_{11} = -L_2 \cdot \sin(\theta_1) - L_3 \cdot \cos(\theta_2) \cdot \sin(\theta_1) - L_4 \cdot \cos(\theta_1) \cdot \sin(\theta_3) \\ - L_4 \cdot \cos(\theta_2) \cdot \cos(\theta_3) \cdot \sin(\theta_1),$$

$$J_{12} = -\cos(\theta_1) \cdot \sin(\theta_2) \cdot (L_3 + L_4 \cdot \cos(\theta_3)),$$

$$J_{13} = -L_4 \cdot \cos(\theta_3) \cdot \sin(\theta_1) - L_4 \cdot \cos(\theta_1) \cdot \cos(\theta_2) \cdot \sin(\theta_3),$$

$$J_{21} = L_2 \cdot \cos(\theta_1) + L_3 \cdot \cos(\theta_1) \cdot \cos(\theta_2) - L_4 \cdot \sin(\theta_1) \cdot \sin(\theta_3) \\ + L_4 \cdot \cos(\theta_1) \cdot \cos(\theta_2) \cdot \cos(\theta_3),$$

$$J_{22} = -\sin(\theta_1) \cdot \sin(\theta_2) \cdot (L_3 + L_4 \cdot \cos(\theta_3)),$$

$$J_{23} = L_4 \cdot (\cos(\theta_1) \cdot \cos(\theta_3) - \cos(\theta_2) \cdot \sin(\theta_1) \cdot \sin(\theta_3)),$$

$$J_{31} = 0,$$

$$J_{32} = -\cos(\theta_2) \cdot (L_3 + L_4 \cdot \cos(\theta_3)),$$

$$J_{33} = L_4 \cdot \sin(\theta_2).$$

The position vector obtained from Equation (8) is used to obtain the Jacobian. Here the joint angles are functions of time. The operation mentioned in Equation (33) is performed. The Jacobian obtained from Equation (33) is with respect to base frame of the proposed robotic device. A code in Appendix D, is formulated to determine the Jacobian, static force and torques.

The determinant of the Jacobian matrix will be analyzed to identify workspace boundary singularities. Note, that the inverse of the Jacobian exists only if the determinant is a non-zero. If the determinant is zero, then singularity arises. This is demonstrated as follows by analyzing the determinant of Equation (33).

$$||J|| = \sin(\theta_3) \cdot \{L_2 + L_3 \cdot \cos(\theta_2)\} \cdot \{0 - L_4 \cdot (L_3 + L_4 \cdot \cos(\theta_3))\} \quad \text{Equation (34)}$$

On simplifying, it is evaluated that singular condition arises at

$$\sin \theta_3 = 0, \cos(\theta_2) = -\frac{L_2}{L_3} \text{ and } \cos(\theta_3) = -\frac{L_3}{L_4} \quad \text{Equation (35)}$$

. Equation (35) add a geometric constraint on the robotic device, such that $L_2 \leq L_3$ and $L_3 \leq L_4$. It can also be interpreted that near such singular configuration small joint torques can generate large force at the end effector. Static force analysis will be used to estimate the holding torques required at the joints in their static position when an external force is applied at the end effector. Moreover, information from the static force analysis can be analyzed further for mechanical design purposes. Static torque can be evaluated by using inward iteration. A parametric set of equations were generated to obtain the joint torques.

For the static force analysis, assume a generalized force acting on the manipulator by the environment as:

$$F_{env} = [F_x \quad F_y \quad F_z]^T \quad \text{Equation (36)}$$

A relationship adopted from Craig *et al.* will be used to express the joint loads and torques from the next coordinate frame to the current coordinate frame, as follows [45]

$$f_i^i = R_{i+1}^i \cdot f_{i+1}^{i+1} \quad \text{Equation (37)}$$

$$n_i^i = R_{i+1}^i \cdot n_{i+1}^{i+1} + P_{i+1}^i \times f_i^i \quad \text{Equation (38)}$$

$$\tau_i = (n_i^i)^T \cdot \hat{Z}_i^i \quad \text{Equation (39)}$$

Where, F_{env} is the external load applied on the last frame, f_i^i is the force exerted on the i^{th} link and expressed in the same frame, n_i^i is the torque exerted on the i^{th} joint and expressed in the same frame and τ_i is the torque exerted on the joint along the axis of rotation. Performing inward iterations on these expressions (Equation (37) and Equation (38)) with the sensor tip being frame 4,

$$F_4^4 = [F_x \quad F_y \quad F_z]^T \quad \text{Equation (40)}$$

$$n_4^4 = [0 \quad 0 \quad 0]^T \quad \text{Equation (41)}$$

Likewise, for the end effector support, $i = 3$,

$$F_3^3 = \begin{bmatrix} 1 & 0 & 0 \\ 0 & 1 & 0 \\ 0 & 0 & 1 \end{bmatrix} \cdot \begin{bmatrix} F_x \\ F_y \\ F_z \end{bmatrix} = \begin{bmatrix} F_x \\ F_y \\ F_z \end{bmatrix} \quad \text{Equation (42)}$$

$$n_3^3 = \begin{bmatrix} 1 & 0 & 0 \\ 0 & 1 & 0 \\ 0 & 0 & 1 \end{bmatrix} \cdot 0 + \left\{ \begin{bmatrix} L_4 \\ 0 \\ 0 \end{bmatrix} \times \begin{bmatrix} F_x \\ F_y \\ F_z \end{bmatrix} \right\} = \begin{bmatrix} 0 \\ -L_4 F_z \\ L_4 F_y \end{bmatrix} \quad \text{Equation (43)}$$

Similarly, for link 2B, $i = 2$,

$$F_2^2 = \begin{bmatrix} \cos(\theta_3) \cdot F_x - \sin(\theta_3) \cdot F_y \\ -F_z \\ \sin(\theta_3) \cdot F_x + \cos(\theta_3) \cdot F_y \end{bmatrix} \quad \text{Equation (44)}$$

$$n_2^2 = \begin{bmatrix} L_4 \cdot F_z \cdot \sin(\theta_3) \\ -L_4 \cdot F_z - L_3 (\sin(\theta_3) \cdot F_x + \cos(\theta_3) \cdot F_y) \\ -F_z \cdot (L_3 + L_4 \cdot \cos(\theta_3)) \end{bmatrix} \quad \text{Equation (45)}$$

Finally, for link 2A, $i = 1$,

$$F_1^1 = \begin{bmatrix} F_z \cdot \sin(\theta_2) + \left(\cos(\theta_2) \cdot (F_x \cos(\theta_3) - F_y \sin(\theta_3)) \right) \\ F_y \cos(\theta_3) + F_x \sin(\theta_3) \\ F_z \cdot \cos(\theta_2) - \left(\sin(\theta_2) \cdot (F_x \cos(\theta_3) - F_y \sin(\theta_3)) \right) \end{bmatrix} \quad \text{Equation (46)}$$

$$n_1^1 = \begin{bmatrix} n_{1x}^1 \\ n_{1y}^1 \\ n_{1z}^1 \end{bmatrix} \quad \text{Equation (47)}$$

Where,

$$n_{1x}^1 = \sin(\theta_2) (L_3 (\sin(\theta_3) \cdot F_x + \cos(\theta_3) \cdot F_y) + F_z \cdot L_4) + F_z \cdot L_4 \cdot \cos(\theta_2) \cdot \sin(\theta_3),$$

$$n_{1y}^1 = -L_2 \left(F_z \cdot \cos(\theta_2) - \sin(\theta_2) \left((F_x \cos(\theta_3) - F_y \sin(\theta_3)) \right) \right) - F_z (L_3 + L_4 \cdot \cos(\theta_3)),$$

$$n_{1z}^1 = L_2 (F_y \cos(\theta_3) + F_x \sin(\theta_3)) + \cos(\theta_2) \cdot \left(\left(L_3 \left((F_y \cos(\theta_3) + F_x \sin(\theta_3)) \right) \right) + (F_z L_4) \right) - F_z L_4 \sin(\theta_2) \sin(\theta_3).$$

The third row in n_i^i contributes towards the torque required to hold the joints in the desired static position. This torque would be used for selecting the holding torque for the actuator for each joint. A code was developed to calculate the numerical values for torque at each joint depending on the applied force. This code is attached in Appendix D. Therefore the numerical values for the actuator holding torques at joint 1, 2 and 3 were evaluated. The analysis assumed a load along the X-direction of the 4th frame, because the proposal was to apply a normal load on the tissue. Equation (48) was justified as presented in Figure 20. Maximum static torque to hold a 1 N load in a particular configuration was estimated as 9 Nmm at joint 1. This value was evaluated from Equation (48), considering F_x is 1 N, θ_3 is 90 ° and θ_2 is 0 °.

$$\tau = \begin{bmatrix} \tau_1 \\ \tau_2 \\ \tau_3 \end{bmatrix} = \begin{bmatrix} F_x \cdot \sin(\theta_3) \cdot \{L_2 + L_3 \cdot \cos(\theta_2)\} \\ 0 \\ 0 \end{bmatrix} \quad \text{Equation (48)}$$

Where, θ_1 , θ_2 and θ_3 are the 1st, 2nd and 3rd joint angles and τ_1 , τ_2 and τ_3 are the holding torque at 1st, 2nd and 3rd joint.

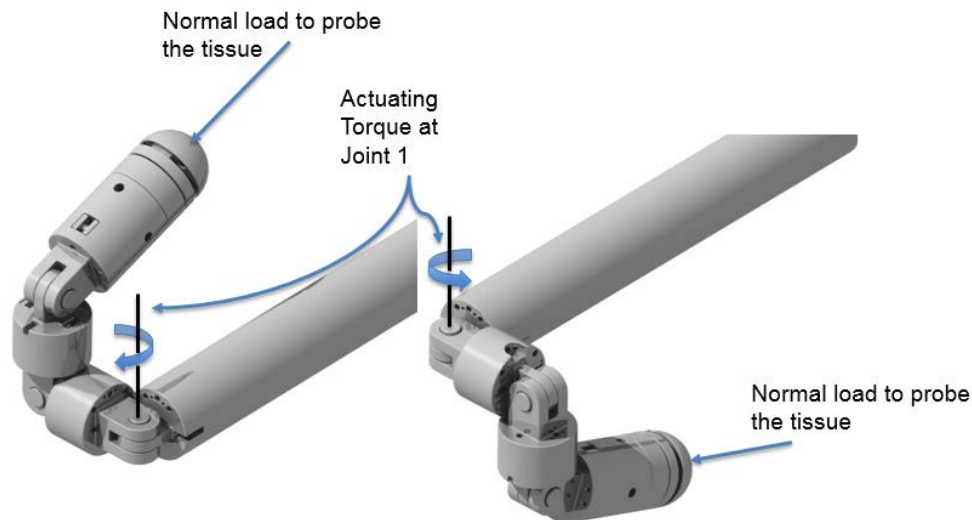


Figure 20: Torque experienced in different configuration due to normal load

3.1.8 Failure Analysis for the Pin and I-beam

As a safety consideration, failure analysis on the joint pins was performed. This analysis was performed using double shear failure of the pin according to Equation (49). The diameter of the pin was constrained due to the overall dimension of the device. Therefore, the channels provided on each component of the manipulator cannot exceed a diameter of 0.8 mm. The area under shear was the surface area of the pin having the diameter 0.8 mm. The material property for medical grade stainless steel instruments having a yield strength of 300 MPa was used to analyze the shear failure of the pin. [47]. A load of 1 N was applied on the pin, based upon the discussion in Section 2.4.2, this load already accounted for a factor of safety of 2.5. Pin shear failure is evaluated as:

$$\tau_{sp} = \frac{\left(\frac{4}{3}\right) \left(\frac{F_{sp}}{2}\right)}{A_{sp}} = \frac{\left(\frac{4}{3}\right) \cdot \left(\frac{1}{2}\right)}{\left(\frac{\pi}{4} \cdot (0.8)^2\right)} = 1.326 \text{ MPa} \quad \text{Equation (49)}$$

Where τ_{sp} is the shear stress exerted on the pin and F_{sp} is the shear load on the pin.

The maximum shear stress that the pin experienced was 1.32 MPa. The factor of safety is evaluated as the ratio of the yield strength of the material over the maximum stress experienced by the component is 226.

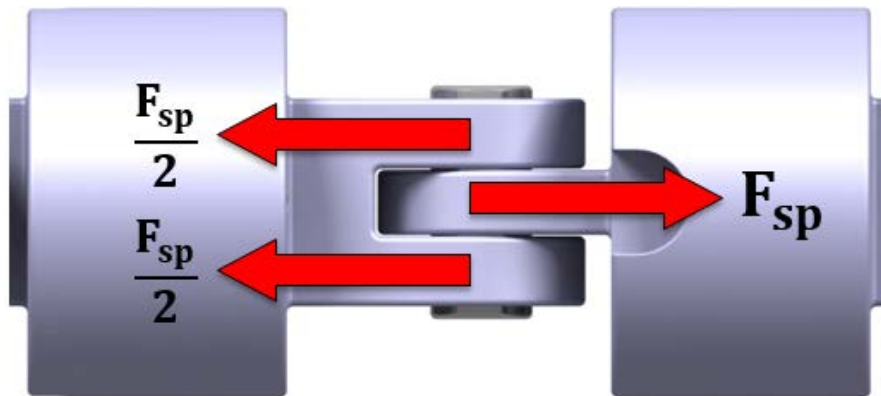


Figure 21: Schematic for double shear failure of the pin joint

The failure analysis of the I-beam was performed using ANSYS Workbench 17.0. The boundary condition of the I-beam is shown in Figure 22. A force of 10 N was chosen because it was evaluated from the preliminary analysis that the maximum moment experienced by the first joint was 9 Nmm when an external load of 1 N was applied, Section 3.1.7. From the geometry, the perpendicular distance between the joint and the attached tendon channel in the inner tube is 1 mm. Therefore, the maximum tension that the tendon will experience will be 10 N, from the moment balance equation. To evaluate the structural failure of the part, a load of 10 N was applied in the bending direction. This resulted in the equivalent von-Mises stress of 152 MPa,

which results in a factor of safety of 1.97 when considering the material properties of medical grade stainless steel [47].

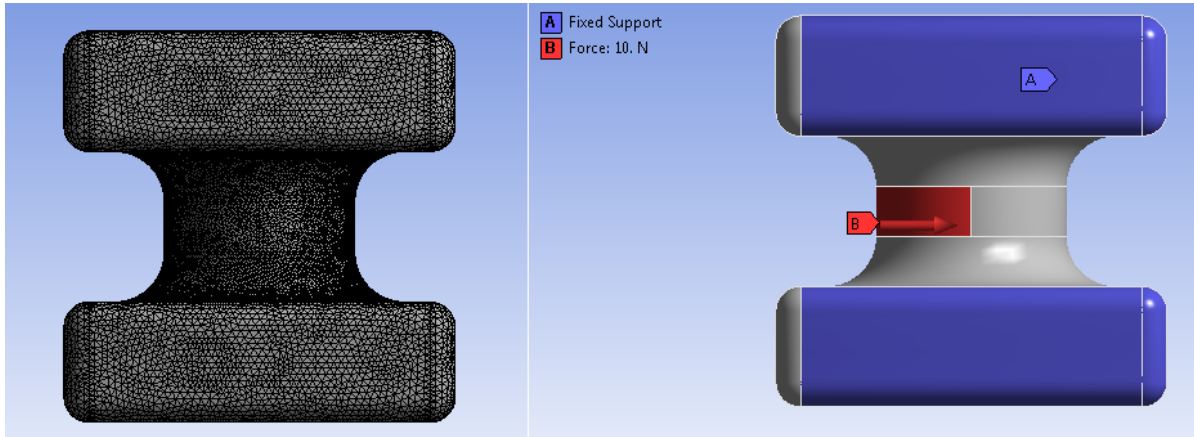


Figure 22: I-beam boundary condition with fine mesh size

3.1.9 Part Failure Analysis

It was important to obtain the failure load for the parts. The loading condition for the part failure analysis was gathered from the static force analysis from Section 3.1.7. Appendix D is used to evaluate the static force and torques acting on the joints. These results were then used to identify the structural failure of the components under static loading conditions. For this particular manipulator application, the load acting on the manipulator will be along the X-direction of the last frame. Therefore all other force components were assumed to be zero. The force and torques acting on the 3rd joint of the manipulator were derived parametrically as in Equation (42) and Equation (43). Therefore $F_x = 1$ N was considered to estimate the failure of the parts. Note that a load of 1 N already accounts for a factor of safety of 2.5. Therefore the load and torques acting on the 3rd joint using the information are as follows:

$$F_3^3 = \begin{bmatrix} F_x \\ 0 \\ 0 \end{bmatrix} \text{ and } n_3^3 = \begin{bmatrix} 0 \\ 0 \\ 0 \end{bmatrix} \quad \text{Equation (50)}$$

These loading conditions were applied on the 3rd joint to determine the static structural failure of the components (sensor support and link 2B). Similarly, the force and torques acting on the 2nd joint of the manipulator were derived from Equation (44) and Equation (45). They are presented in Equation (51),

$$F_2^2 = \begin{bmatrix} F_x \cdot \cos(\theta_3) \\ 0 \\ F_x \cdot \sin(\theta_3) \end{bmatrix} \text{ and } n_2^2 = \begin{bmatrix} 0 \\ -F_x \cdot L_3 \cdot (\sin(\theta_3)) \\ 0 \end{bmatrix} \quad \text{Equation (51)}$$

A combination of these force and torques were applied on link 2A and link 2B, to determine the structural failure of these components. The results obtained from Equation (51) are discussed in Section 4.1.2.

Similarly, loads and torques obtained from Equation (46) and Equation (47) will be used to estimate the failure of the components at joint 1. The analysis assumed a load acting along the X-direction of the last frame. Equation (52) and Equation (53) are evaluated to determine the loading conditions on joint 1 of the device to determine the failure of the component. These loading conditions will be used to evaluate the failure of link 2A and inner tube.

$$F_1^1 = \begin{bmatrix} F_x \cdot \cos(\theta_2) \cdot \cos(\theta_3) \\ F_x \cdot \sin(\theta_3) \\ -F_x \cdot \cos(\theta_3) \cdot \sin(\theta_2) \end{bmatrix} \quad \text{Equation (52)}$$

$$N_1^1 = \begin{bmatrix} F_x \cdot L_3 \cdot \sin(\theta_2) \cdot \sin(\theta_3) \\ F_x \cdot L_2 \cdot \cos(\theta_3) \cdot \sin(\theta_2) \\ F_x \cdot \sin(\theta_3) \cdot (L_2 + L_3 \cdot \cos(\theta_2)) \end{bmatrix} \quad \text{Equation (53)}$$

3.2 Sensor Design

The sensor was designed to measure the normal tissue reaction force acting on the bladder., therefore requiring high sensitivity. In order to meet the dimension constraints along with the loading conditions that the sensor needs to measure, a sensor concept was developed,

designed and analyzed. The sensor working principle is as presented in Figure 23. According to Figure 23 a normal load will act on the load transmitting element. This load will be transferred to a beam and will be measured by the sensing element.. A sensing element will be attached to the beam. The beam will be designed such that uniform loading on the beam can be measured by using a strain gauge along the axial direction of the beam. The sensor is designed using 4 components such that the load can be transferred from the apex of the device to the sensing element, which is the strain gauge attached on the beam in the sensor assembly. The 4 components of the sensor are sensor head, upper clamp, lower clamp and beam. Figure 24 is the exploded view of the proposed sensor assembly, the components of the sensor assembly will be discussed in Section 3.2.1

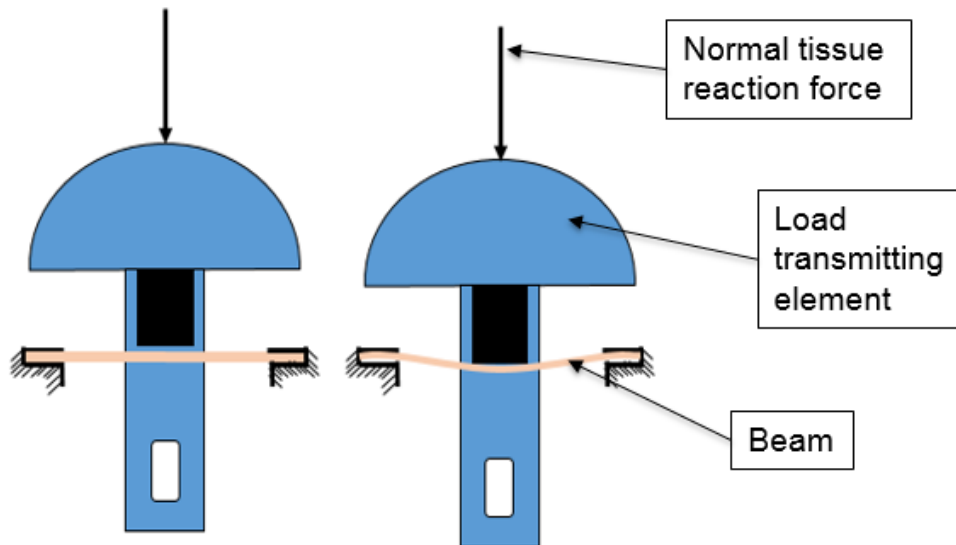


Figure 23: Proposed sensor working principle

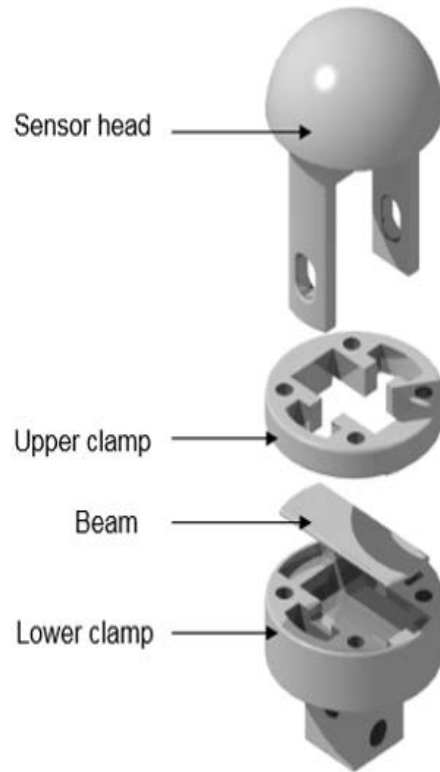


Figure 24: Proposed sensor assembly model

3.2.1 Sensor Design Components

Sensor head: This component of the assembly contacts the tissue on the hemispherical end and the beam at the opposite end. This sensor head will help to transmit the contact force from the tissue to the sensing element. The legs of the sensor head will be guided into the pockets provided in the sensor support component discussed. The legs of the sensor head are free to translate, in a prismatic motion along the length, in the sensor support component. Also the sensor head will be held to the assembly by a threaded screw that will pass through the locating slots (Figure 25), which provides free translation of the sensor head. The extrusion at the bottom of the dome called as load transfer extrusion, located between the two legs of the sensor head, will transmit the applied load to the beam. The deflection in the beam will be measured by the

sensing element. The clamping bolt spacing was provided because the sensor head should not come in contact with other clamping components. Appendix A.5 shows the sensor head drawing.

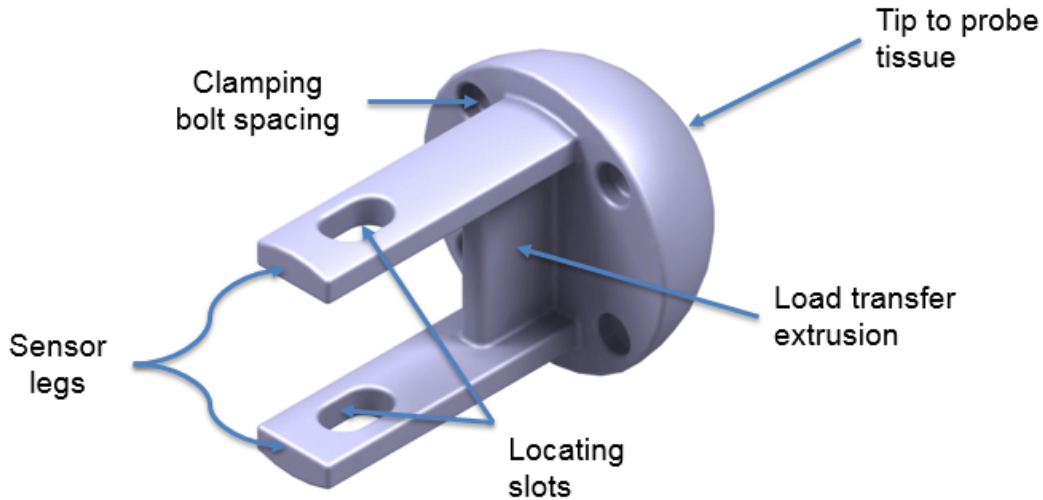


Figure 25: Sensor assembly: sensor head component

Upper clamp: The upper clamp of the sensor is the part which is situated exactly below the sensor head. The important function of this part is to firmly hold the beam, such that both ends of the beam are fixed. This is achieved by providing clampers on one face of the component as presented in Figure 26. The guideway for the sensor head legs and load transfer extrusion were provided in this component, as shown in Figure 26. These guideways allow frictionless motion of the legs and the load transferring extrusion. Apart from these slots, clamping bolt holes are provided on this part to clamp it along with the lower clamp component of the sensor assembly.

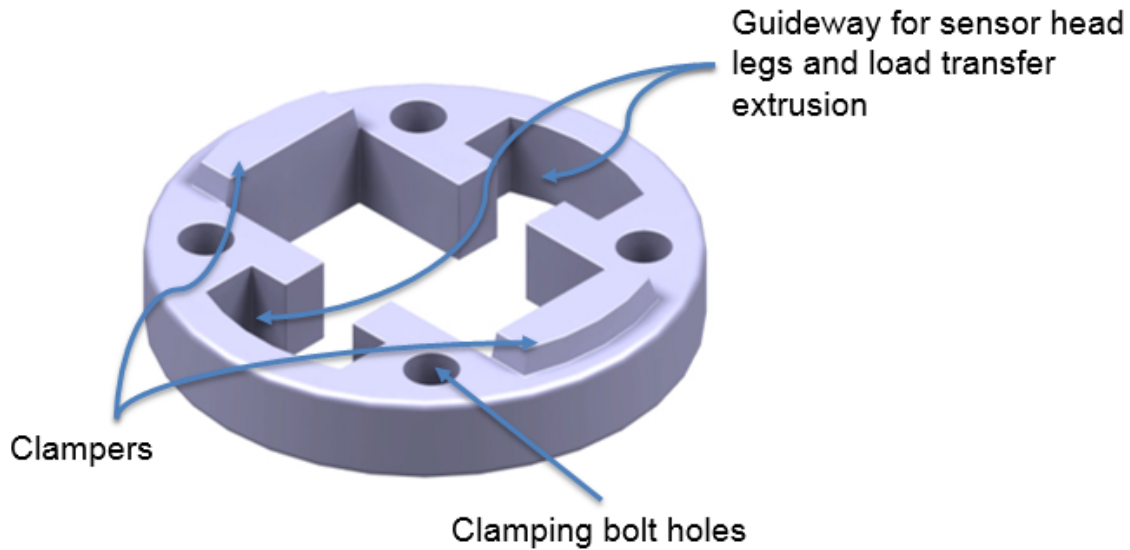


Figure 26: Sensor assembly: upper clamp component

Lower clamp: The lower clamp in the sensor assembly will serve the main purpose of holding the beam which will be attached with the strain gauge. Step-1 is used to serve this purpose as presented in Figure 27. It was necessary to provide an arrangement such that a mechanical stop will be activated, in case a force greater than 0.4 N was applied normal to the sensing element. This function was provided by designing Step-2. This mechanical stop will also be used to indicate to the physician that the applied force is reaching an unsafe load for the beam sensor assembly so that appropriate action to stop the further testing of the tissue can be taken. The lower clamp component has slots similar to the upper clamp component to allow a prismatic motion for the sensor head legs. Slots were provided for wire harnessing of the strain gauge wires.

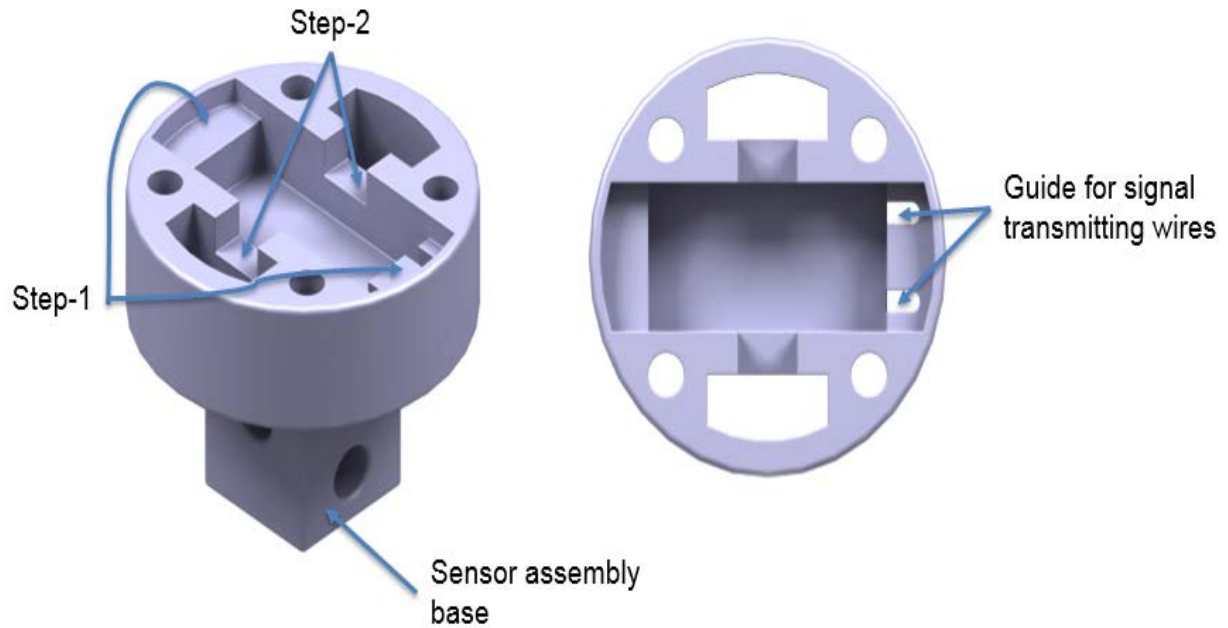


Figure 27: Sensor assembly: lower clamp component

Beam: The model of the beam is presented in Figure 28. It was necessary to design the beam such that it can provide a reading for not only applied load but also an indication if the load was exceeding specified maximum limit. Due to size constraints of the device, it was necessary that the load transferring mechanism of the beam be simple, yet provide necessary output data. The beam will be fixed between the upper and lower clamps. This will theoretically allow for the analysis to consider both ends of the beam fixed. The strain gauge will be mounted at the bottom face of the beam along the axial direction as shown in Figure 28. It was essential to attach the strain gauge at the bottom face because the top face of the beam will come into contact with the sensor head component. Section 3.2.2 will discuss the analysis for the design of the beam.

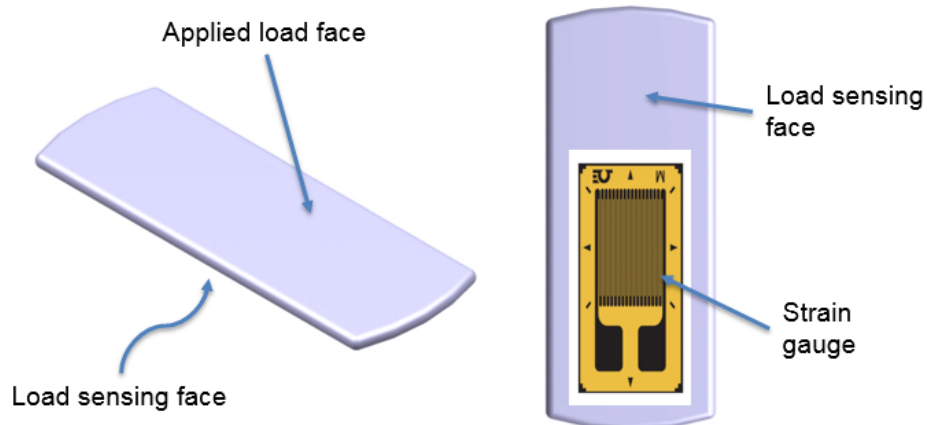


Figure 28: Sensor assembly: beam component

3.2.2 Analysis for Sensor Beam Design

The parametric equations derived in Bansal were used to design a fixed-fixed beam assuming a concentrated load at the center[48].. These equations were used to evaluate beam thicknesses. The selected thicknesses were then used to determine the strains and the maximum deformation in the beam. The deformation in the beam was obtained using the Euler-Bernoulli beam theory [49]. Equation (54) represents the deformation of the beam as a function of applied load, active length, geometric and material properties. Due to symmetry, deformation along only half length of the beam was evaluated [48]. Figure 29 is a representation of the beam boundary condition along with the active length of the beam.

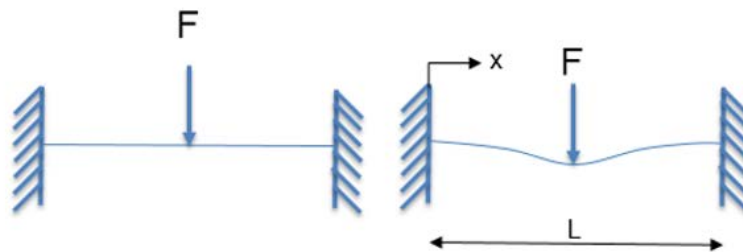


Figure 29: Fixed-fixed beam schematic

$$\delta = \frac{\left\{ \frac{F \cdot x^3}{12} - \frac{F \cdot L \cdot x^2}{16} \right\}}{E \cdot I} \quad \text{Equation (54)}$$

The bending stress in the beam was evaluated using the relationship between the geometric properties of the beam and the moment due to the applied load. This was evaluated as in Equation (55) and Equation (56),

$$\sigma_{\max} = M_{\max} \cdot \frac{y}{I} = \frac{F \cdot L}{8} \cdot \frac{\frac{h}{2}}{\frac{b \cdot h^3}{12}} \quad \text{Equation (55)}$$

$$\epsilon_{\max} = \frac{\sigma_{\max}}{E} \quad \text{Equation (56)}$$

Where, δ is the deflection in bending direction of the beam at any point up to half length of the beam, F is the applied load, x is the distance along the length of the beam as represented in the Figure 29, L is the total length of the beam, E is the Young's modulus, I is the moment of Inertia, σ_{\max} is the maximum bending stress, M_{\max} is the maximum bending moment, y is the perpendicular distance to the neutral axis, b is the width of the beam, h is the thickness of the beam and ϵ is the strain.

Using Equation (56), a rectangular geometry was considered in the design of the beam thickness to achieve reasonable and measurable strain. Figure 30 was used to select the thickness considering the failure of the beam and the measurable axial strain of the beam. Due to the size constraints the length and the width of the beam were selected as 2 mm and 1 mm respectively. The analysis of the beam was performed assuming medical grade stainless steel material properties with a yield strength of 300 MPa [47]. For selecting beam thickness a normal load of

0.4 N was applied at the center of the beam. As represented in Figure 30, the green colored markers indicate stresses in the beam considering a factor of safety of 3 or greater.

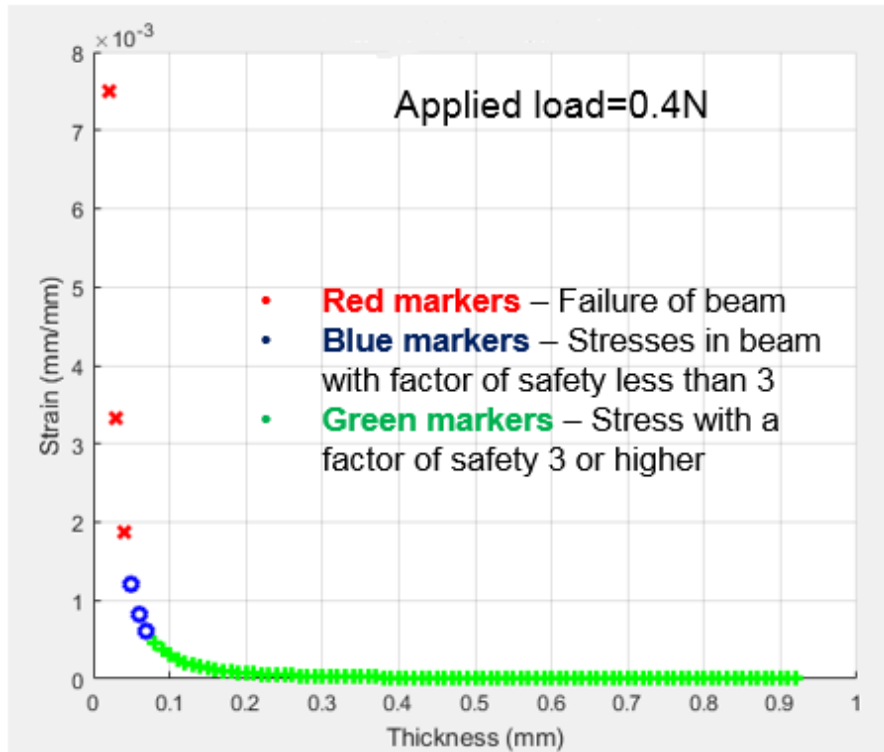


Figure 30: Strain as a function of thickness for beam selection for applied load of 0.4 N

The blue colored markers indicate stresses induced in the beam with the factor of safety below 3 but not at failure, and the red markers indicate stresses induced which will cause the beam to fail. Figure 30 helps in selecting a beam thickness of any values greater than 0.08 mm. However, it was necessary not to choose a thicker beam as it would reduce the sensitivity of the reading thus requiring a high-resolution data acquisition device. Hence, beam thickness of 0.1 mm was selected considering the design requirements, and ability to measure the load less than 0.4 N. Upon having the desired beam thickness it was essential to perform a strain analysis, which would determine the minimum readable strain by the data acquisition device (DAQ). From Equation (56) strains were calculated for variable beam thickness and loads acting on the beam.

A code was generated in MATLAB to evaluate the strain on the beam as a function of applied load starting from 0 N to a maximum of 0.4 N. A National Instruments DAQ device (16-bit, model no.USB-6001) was selected to acquire the data of the strain gauge. The other input parameters were excitation voltage of 5 V, strain gauge resistance of 120 Ω and strain gauge factor of 2.09. It was evaluated that the minimum readable strain without amplifying the signal was approximately 30.5 $\mu\epsilon$, which corresponds to a load of 0.04 N. Whereas the strain value obtained for a 0.4 N load was 310 $\mu\epsilon$.The analysis adapted to convert the change in output voltage to the strain experienced by the beam is presented in Appendix E. Figure 31 is a representation of the strains as load was applied with various beam thickness. Green line was evaluated for the selected beam thickness of 0.1 mm. In Figure 31 Black lines indicate the strains with respect to applied load for beam thicknesses of 0.06 mm, 0.08 mm, 0.12 mm and 0.14 mm. These thicknesses were selected because the beam with thickness less than 0.06 mm will fail and with thickness greater than 0.14 mm will yield very small strain values.

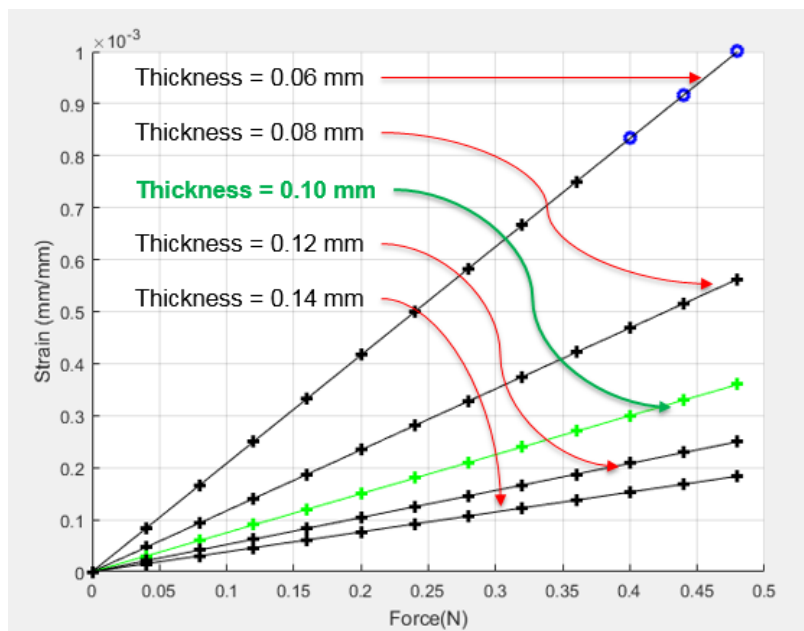


Figure 31: Strain as a function of applied force on the beam with various thicknesses

3.2.3 Strain Gauge

The sensor is one of the most important components of the device because it is needed to measure the applied force that the tissue will experience. A sensor is designed such that it can read relatively small forces with high sensitivity and less than 0.4 N. A sensor using a strain gauge can be effectively designed to obtain the necessary data. The design of the sensor discussed in this section assumes an off-the-shelf strain gauge having maximum dimensions of 1×1.5 mm. The strain gauge will be attached to the bottom side of the beam, facing the lower clamp in the sensor assembly. The proposed strain gauge for the application is a metal foil strain gauge. Analysis for current research was performed using a strain gauge (gauge type EA-13-060LZ-120) from Measurements group, Inc. having a resistance of 120Ω , a gauge factor of 2.09. The allowable strain range for the attached strain gauge is approximately 5% for 6mm gauge length. Figure 33 represents the strain gauge attached on the scaled prototype beam model.



Figure 32: Strain gauge attached on the scaled aluminum prototype beam model

Chapter 4

Result and Discussion

4.1 Results

4.1.1 Kinematics Verification of the Design

On deriving the kinematics equations for the device, verification was performed to confirm that the device indeed reaches the desired position. This verification was performed by aligning the 4th frame as demonstrated in Figure 18 of the device assembly to the area near the trigone of the bladder. This can be demonstrated by selecting a point on a sphere.

As discussed in Section 3.1.6, the joint angles were defined to be zero and the link length values were obtained from the design of the device, to acquire the forward kinematics results. The relationship was evaluated by substituting the defined joint values into Table 4 along with the geometrical design constants. The final homogeneous transformation matrix that relates the sensor tip frame to the base frame was then obtained by performing the operation in Equation (57).

$$H_4^0 = H_1^0 \cdot H_2^1 \cdot H_3^2 \cdot H_4^3 = \begin{bmatrix} 1 & 0 & 0 & 29 \\ 0 & 1 & 0 & 0 \\ 0 & 0 & 1 & 0 \\ 0 & 0 & 0 & 1 \end{bmatrix} \quad \text{Equation (57)}$$

. Geometric calculations can verify that, having all the joint variables defined to be 0°, the sensor tip is 29 mm away from the base frame in the X-direction of the base frame. Along with the geometric verification of the forward kinematics, it was necessary to perform an analysis which can assure that the device will be able to reach the trigone of the bladder. To verify if the device indeed reaches the trigone region, 2 more arbitrary points on a sphere with radius

equivalent to bladder dimension were chosen. This sphere represented a completely filled bladder. On performing the forward kinematics it was evaluated that coordinates 15.7 mm, -11.1 mm, -4.5 mm were obtained for joint angles configuration $-10^\circ, 56^\circ, -84^\circ$ as represented in Figure 34. Coordinates 19.21 mm, 2.12 mm, 13.62 mm were obtained on the trigone for the joint angles configuration $13^\circ, -70^\circ, 0^\circ$ and this is shown in Figure 35. Evaluating these results concluded that the variation in the radius obtained by both the coordinates with respect to the base frame were due to the assumption the robot was a stick manipulator. Frame assignment did not consider the geometry of the links. Figure 34 and Figure 35 represents a model for an inner bladder wall, the trigone region is presented, the base, and the last frame of the robot and the bladder are shown in the figure as well. Equation (58) and Equation (59) were used as input parameters to evaluate the joint angles for both configurations. As estimated the joint angles obtained on performing inverse kinematics resulted as equivalent to those that were given as input in the forward kinematic analysis. The inverse kinematics was performed using the code attached in Appendix C. Also, verification for inverse kinematics was performed by providing a homogeneous transformation matrix which represented a frame out of workspace area and as expected, the results were not provided, the reason being the frame not being in workspace.

$$H_4^0 = H_1^0 \cdot H_2^1 \cdot H_3^2 \cdot H_4^3 = \begin{bmatrix} 0.19 & -0.54 & 0.81 & 15.758 \\ 0.98 & 0.13 & -0.14 & -11.114 \\ -0.03 & 0.82 & 0.55 & -4.5972 \\ 0 & 0 & 0 & 1 \end{bmatrix} \quad \text{Equation (58)}$$

$$H_4^0 = H_1^0 \cdot H_2^1 \cdot H_3^2 \cdot H_4^3 = \begin{bmatrix} 0.33 & -0.22 & -0.91 & 19.21 \\ 0.07 & 0.97 & -0.21 & 2.12 \\ 0.93 & 0 & 0.34 & 13.62 \\ 0 & 0 & 0 & 1 \end{bmatrix} \quad \text{Equation (59)}$$

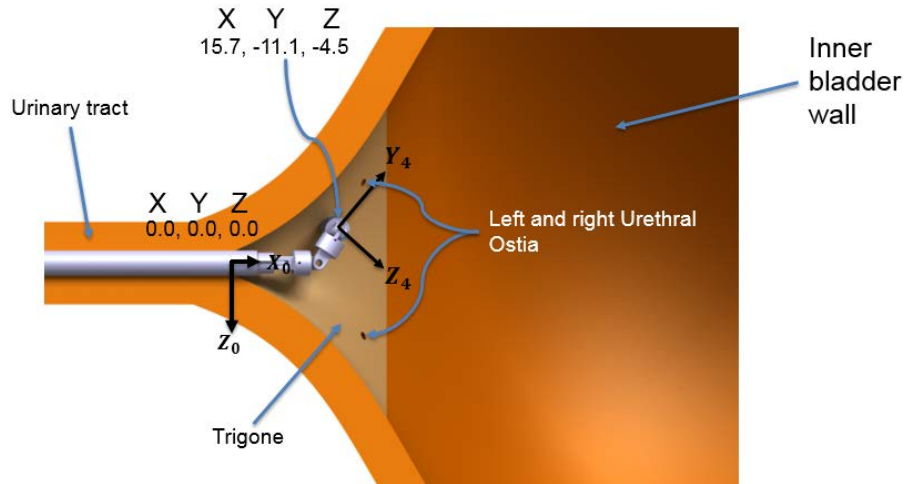


Figure 33: Schematic representation of forward kinematic analysis to verify if the device reaches the trigone area with coordinates (15.7, -11.1, - 4.5) mm

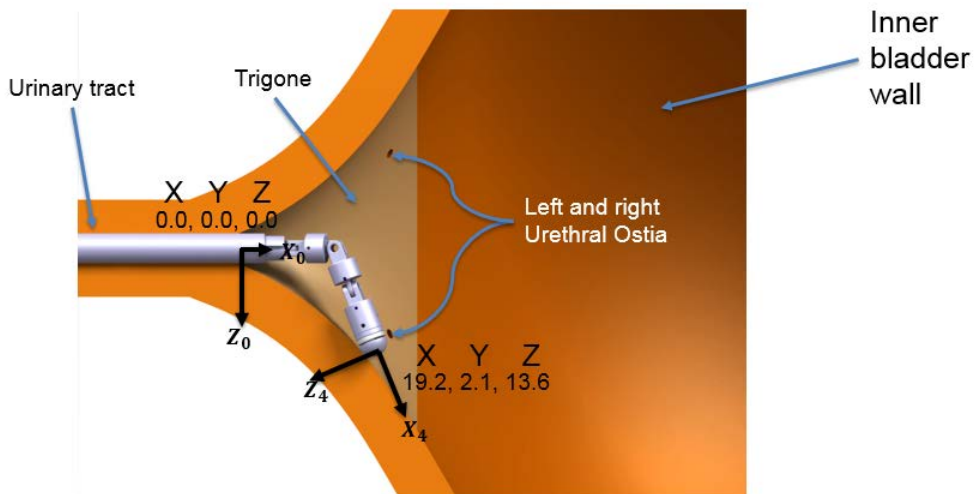


Figure 34: Schematic representation of forward kinematic analysis to verify if the device reaches the trigone area with coordinates (19.2, 2.1, 13.6) mm

4.1.2 Static Force and Joint Torque for Part Failure Analysis

The loading condition mentioned in Section 2.4.2, such that a load of 1 N was applied on the sensor tip, considering a factor of safety of 2.5. This load will be transmitted to the sensor support component. A fixed support is provided, on the face where the lower clamp of the sensor assembly would rest. The material used for the analysis was medical grade stainless steel having a yield strength of 300 MPa [47]. The finite element analysis was performed in ANSYS Workbench 17.0 with a Hex Dominant mesh consisting of 147926 elements. Figure 36 shows the equivalent von-Mises stress estimated on the sensor support component. The loading conditions mentioned Equation (50). The loading conditions for all components are obtained by applying a normal load of 1 N on the last frame. For failure analysis the configuration selected was such that all the joint angles were rotated to 45° . Maximum stress estimation for sensor support component was approximately 2 MPa. Thus an additional factor of safety of 150 was assured.

The analysis was performed for Link 2B for a similar configuration, where all the joints were rotated at 45° . Figure 37 shows the estimated equivalent stress experienced by link 2B due to the loading condition applied from Equation (50) and Equation (51). The analysis was performed with a Hex Dominant mesh consisting of 160106 elements. The maximum stress that this component experiences is 4.3 MPa. An additional factor of safety of 18 is evaluated for the component.

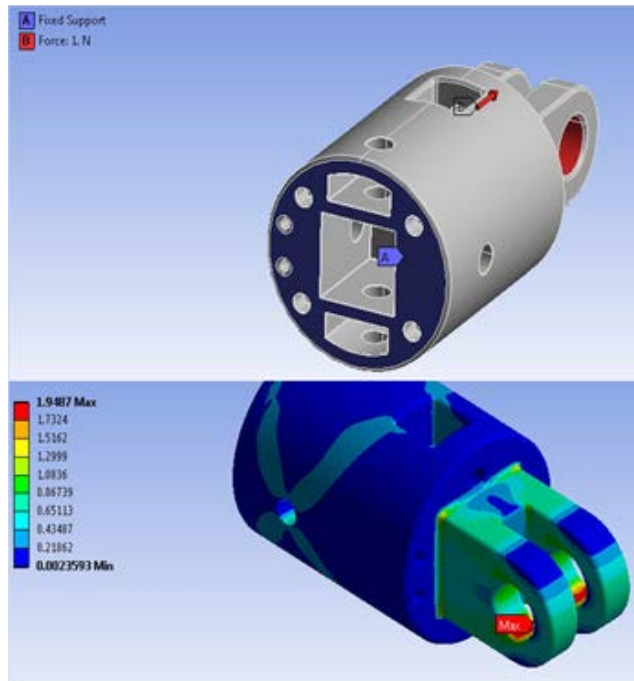


Figure 35: Boundary condition and equivalent von-Mises stress determined on the sensor support component

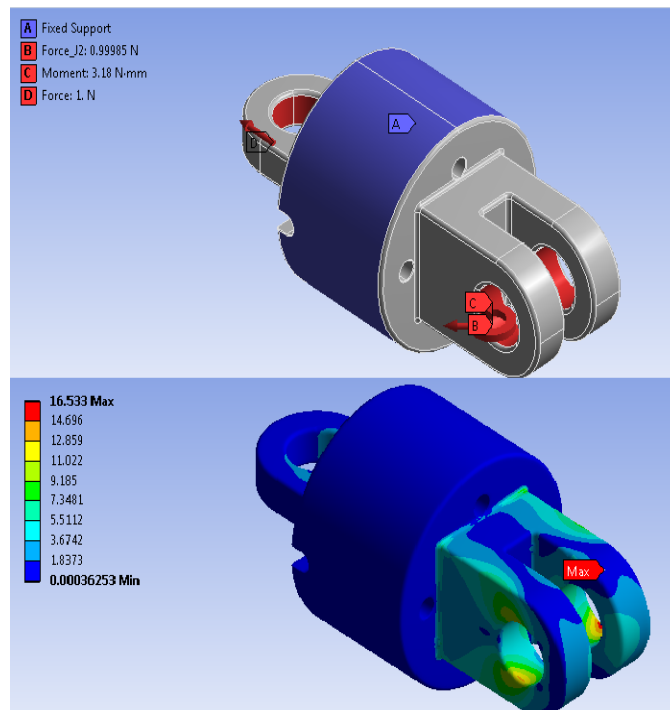


Figure 36: Boundary condition and equivalent von-Mises stress determined on link 2B

The analysis in Section 3.1.9 was used to evaluate the loading condition on link 2A and inner tube. These loading conditions on link 2A are obtained from Equation (51), Equation (52) and Equation (53). The analysis is performed with a Hex Dominant mesh consisting of 68628 elements. Figure 38 shows the maximum stress experienced by link 2A, which is 46 MPa. Assuming the material to be medical grade stainless steel with the yield strength of 300MPa [47], a factor of safety of 6.4 is achieved in addition to the 2.5 already considered due to the applied loading condition.

The loading condition for the inner tube component is obtained from Equation (52) and Equation (53). The analysis is performed with a Hex Dominant mesh consisting of 206854 elements. Figure 39 shows the estimated equivalent von-Mises stress. The maximum stress experienced by inner tube is 160 MPa, which yields an additional factor of safety of 1.87.

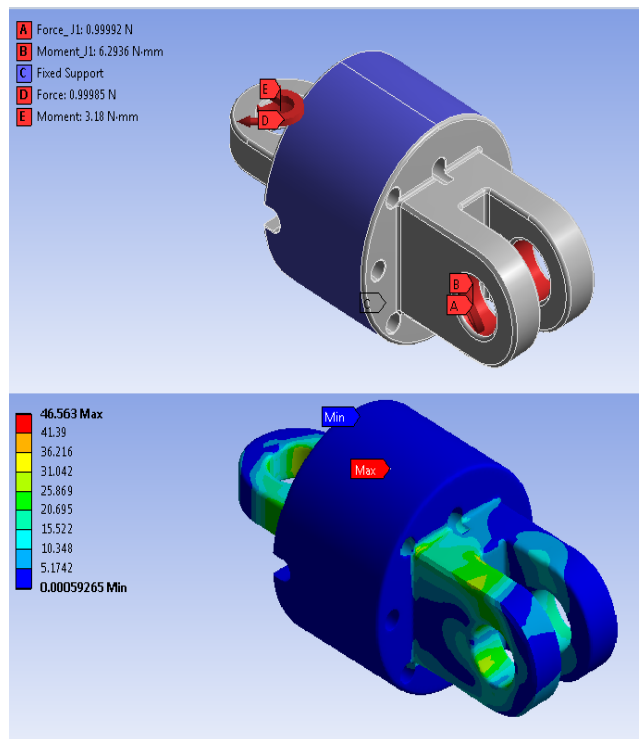


Figure 37: Boundary condition and equivalent von-Mises stress estimated on link 2A

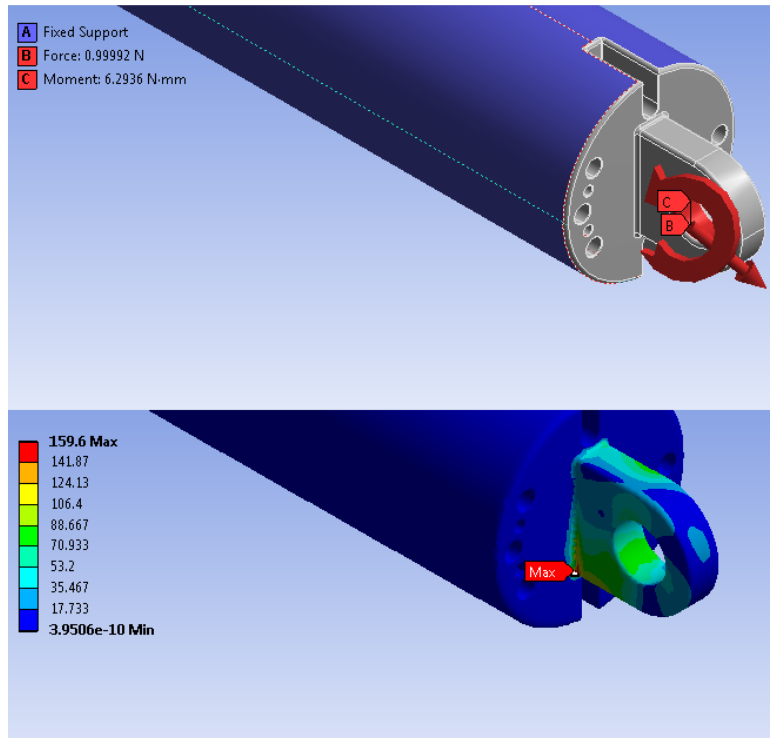


Figure 38: Boundary condition and equivalent von-Mises stress estimated on inner tube

4.1.3 Proposed Sensor Concept Verification

The proposed sensor was fabricated at 5 times scale using in-house 3D printer, and assembled for verification as represented in Figure 40. For the verification of the operation of the scaled sensor prototype a sensor calibration set-up developed for a different in-house project was modified such that the proposed sensor can be mounted on it. For conceptual verification, the beam was chosen as aluminum having a modulus of elasticity of 69 GPa. Dead weights were added on the carriage of the calibration set-up which transferred the load to the sensor head, which eventually transfers the load to the beam and thus sensing element. The sensing element can measure only the normal component of the applied load, and no indication will be provided if loads other than normal are experienced. Analysis was carried out for experimental verification

of the scaled sensor prototype. Maximum stress experienced by a fixed at both end beam was evaluated in Equation (55)

Where, σ_{\max} is maximum stress experienced by the sensing element, F is normal load applied on the sensor head, L is active length of the beam and Z is section modulus of the beam. The maximum strain experienced by the beam in the elastic region can be evaluated using the linear relationship between stress and strain. This was evaluated in Equation (56).

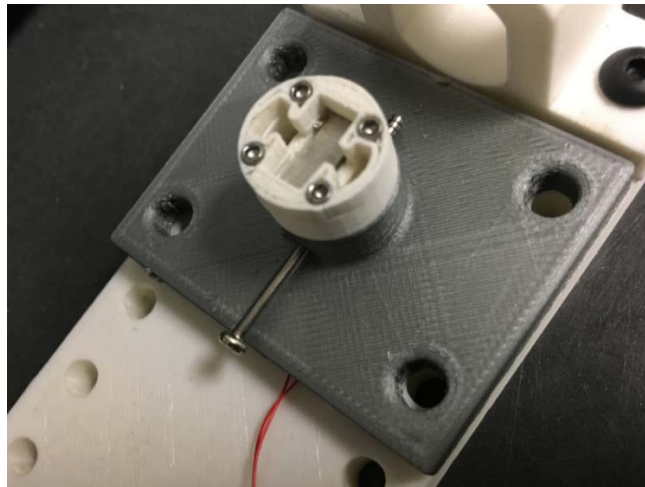


Figure 39: Illustration of sensor assembly without sensor head component

Where, E is Young's modulus of the material, Z is the section modulus for a rectangular cross section, b is the width of the beam element, and h is the thickness of the selected beam element. Therefore the 5 times scaled beam model with same material properties will yield the strain equation as calculated in Equation (60).

$$\epsilon_{N\max} = \frac{1}{25} \cdot \frac{6 \cdot F \cdot L}{8 \cdot b \cdot h^2 \cdot E} \quad \text{Equation (60)}$$

Hence from Equation (60) it was demonstrated that 25 times of actual load (0.4 N) needs to be applied on the scaled sensor prototype. Weights were added to the sensor calibration assembly and the change in voltage was obtained using Wheatstone bridge completion module.

The loads were incremented by 1 N. The resolution of 14-bit DAQ was 0.3 mV. Therefore the measurable strain for this minimum voltage was $115 \mu\epsilon$, which corresponds to a load of 0.04 N and approximately 1 N in the scaled model. The sensitivity of the sensor can be improved further by amplifying the output voltage signal from the sensor. Each loading condition was repeated 5 times, and similar responses were encountered. As expected a dead zone was identified when a load below 1 N was applied on the scaled model. Figure 41 demonstrates the signal flow chart of the proposed sensor calibration setup.

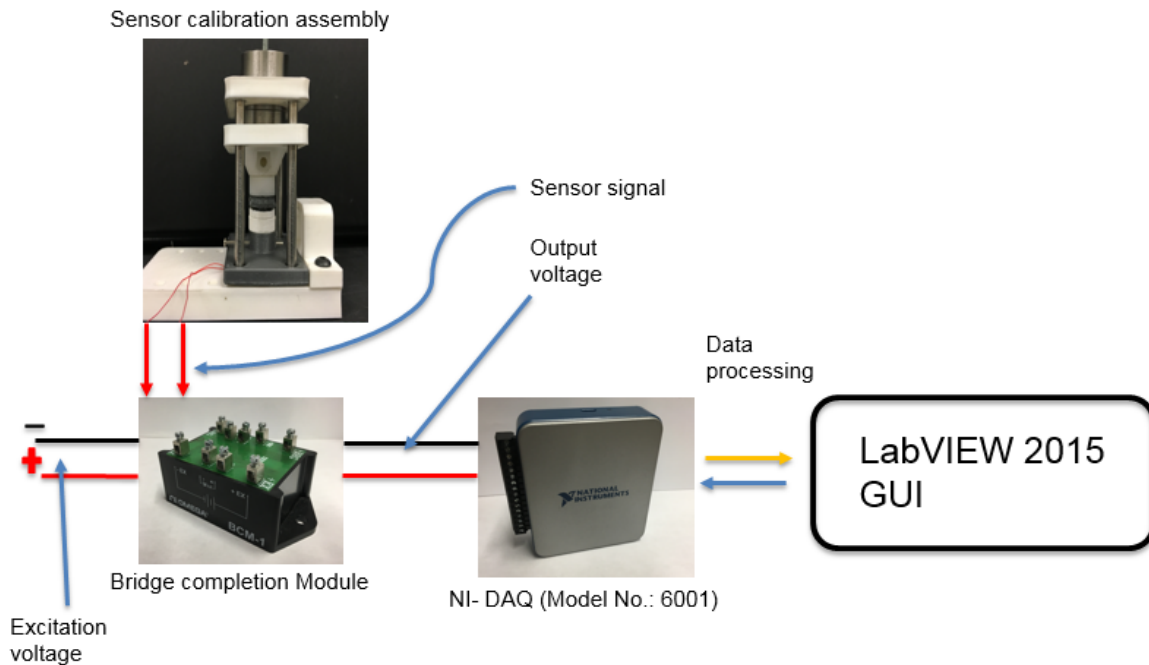


Figure 40: Signal flow diagram of the proposed sensor design

4.2 Discussion

Quantitative measures for workspace analysis of the manipulator can be used to evaluate the efficiency of the proposed design. According to Craig, the length sum of the manipulator can be defined from Equation (61) [45].

$$L = \sum_{i=1}^N (a_{i-1} + d_i) \quad \text{Equation (61)}$$

Where, L is length sum, a is MDH parameter, d is MDH parameter and N is Total number of links. From Equation (61) the length sum for the manipulator is evaluated as

$$L = L_2 + L_3 + L_4 = 19 \quad \text{Equation (62)}$$

The structural length index defined from Craig is used to estimate the structural amount of relative index to generate a given work volume. A good design should have low Q_L value. The proposed manipulator workspace volume is 28349 mm^3 . The workspace volume is approximated using the volume of a hemisphere. Therefore the structural length index is evaluated as

$$Q_L = \frac{L}{\sqrt[3]{w^3}} = \frac{19}{\sqrt[3]{14365.45}} = 0.78 \quad \text{Equation (63)}$$

Where, L is the length sum of the manipulator, w is workspace volume. This is a small value for Q_L which indicates a good conceptual designed manipulator

Initial experiments on the scaled sensor calibration setup were performed in sets of 10. Dead weights of 100 g, 200 g, 300 g, 400 g and 600 g were used in the experiments. The signals were measured from the bridge completion module by using LabVIEW interface. The resulting output voltage from LabVIEW was processed to obtain the strain experienced by the strain gauge. Appendix E is the data obtained from the initial experiments on the sensor validation set up. On acquiring 10 such sets of data for a single loading condition, an average of strain value versus applied load was plotted. This result was then compared with the theoretical expected values. Figure 42 shows the comparison of the experimental and theoretical strain values. It was expected that the graph in Figure 42 is linear similar to that in Figure 31. However, the strain

values evaluated from experimentation were slightly higher as compared to the theoretical. This attributed to the difficulties to clamp the beam completely between the upper and lower clamps for a true fixed-fixed condition.

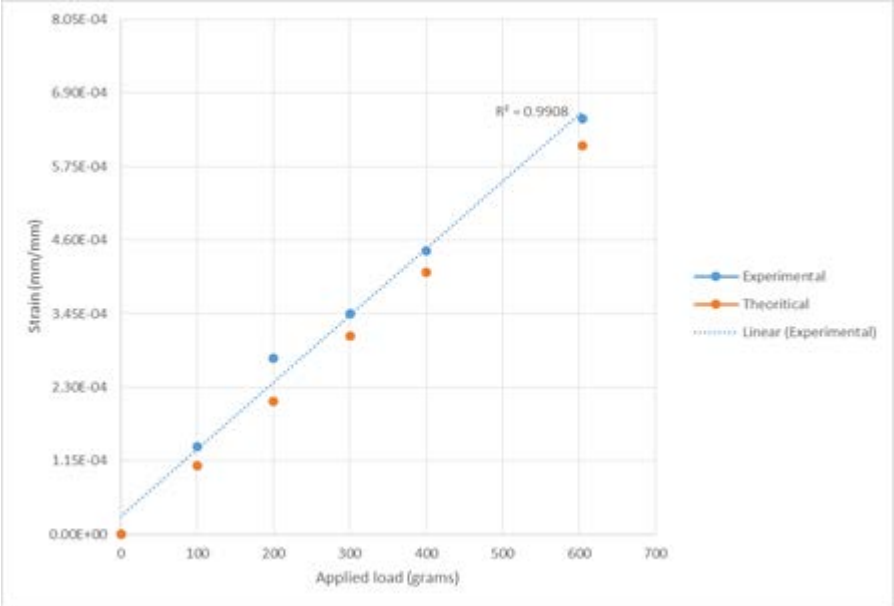


Figure 41: Experimentally and theoretically comparison of strain experienced by the beam as a function of applied load

Chapter 5

Conclusions and Recommendation for Future Research

5.1 Conclusions

The goal of the research was to develop a robotic device to evaluate soft tissue properties. In order to perform this task, it was necessary to design a miniature robotic device that will be able to reach the human bladder in-vivo without invasive surgery while minimizing discomfort during diagnosis. The device should be able to actuate inside the bladder and probe the inner bladder wall and the trigone area. To fulfil these goals the current research focused on designing, developing and analyzing a robotic device and a sensor. The discussion in Section 2.3 and Section 2.4.1 included the proposed insertion methodology of the device in the urinary tract and design constraints of the device respectively. A mathematical hyperelastic model was introduced in Section 2.4 to estimate the approximate tissue loads. A rigid link manipulator design was proposed to manipulate inside the bladder and access the trigone area of the bladder. The device failed to access the area outside the trigone region. It was analyzed that the sensor tip of the proposed manipulator was not able to align to the normal from a point of interest on a surface. The device was able to reach the point of interest with an arbitrary orientation. Kinematic analysis was performed to develop a relationship between the sensor tip and the user end. Static force analysis was performed to evaluate the minimum required holding torque to estimate the actuator size. Failure analysis was performed using finite element results. A sensor design was proposed in Section, 3.2 to interact with the tissue. A beam was designed. The analysis was performed for the proposed sensor model. Precautionary measures in design of the beam were considered to indicate if the applied load exceeded the maximum recommended load. The strain

gauge used in the proposed sensor design was not sensitive enough to measure loads less than 0.04 N. A scaled prototype of the device and model were developed. Initial experiments were performed on the scaled prototype sensor assembly. A relationship was developed between the scaled and actual sensor model. Based on the limitations identified during the current research for the proposed manipulator future recommendations are advised.

5.2 Recommendations

The device was designed considering 3 DOF manipulations. It was estimated that using just 3 DOF does not assist with reaching the side walls of the bladder, nevertheless, this device can reach the trigone region of the bladder. Even if the existing design of the device was able to reach the specified point on the trigone of the bladder, it was not able to orient itself in a normal direction. Extending a 3 DOF mechanism to a 6 DOF will help gain access to all the regions inside the bladder and also orient in the normal direction to apply normal load on the tissue. Accessing areas other than the trigone may be of value to the physician to treat other bladder abnormalities. Therefore it is recommended to extend the analysis of a 3 DOF to a 6 DOF by the addition of a pitch, yaw and translation in the present design represents the existing and the recommended degree of freedom for the manipulator. The green arrows indicate the current degrees of freedom while the red arrows indicate the additional degrees of freedom. In black arrows indicate the axis of rotation of the red arrows near it. Both the axis of rotation are about the same point, however, they have been marked at a distance for ease of understanding.

Actuator can be implemented to actuate the tendons in the existing device to develop an automated system. The actuator will assist to automatically manipulate inside the bladder and probe the inner bladder wall to collect the necessary data.

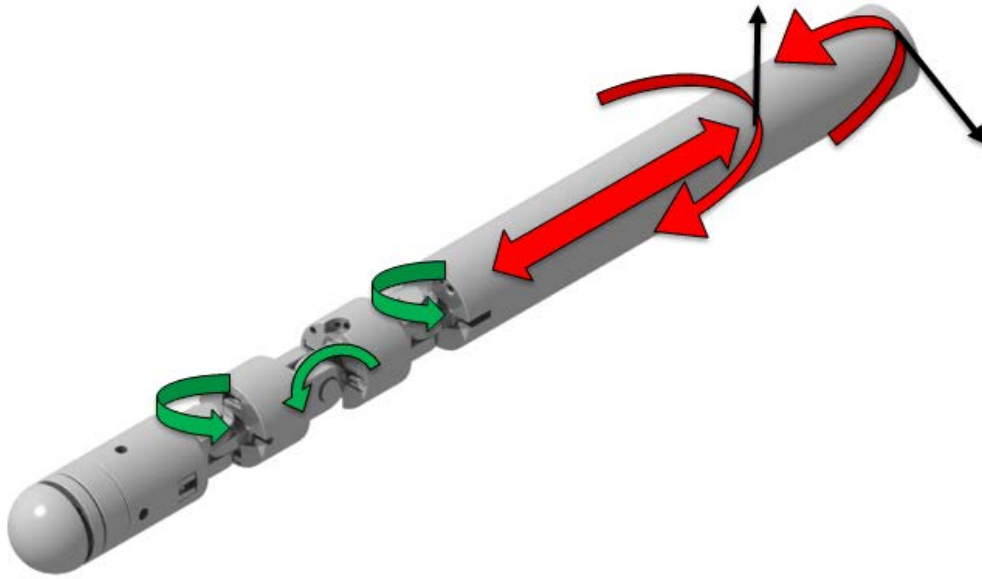


Figure 42: Extended degrees of Freedom

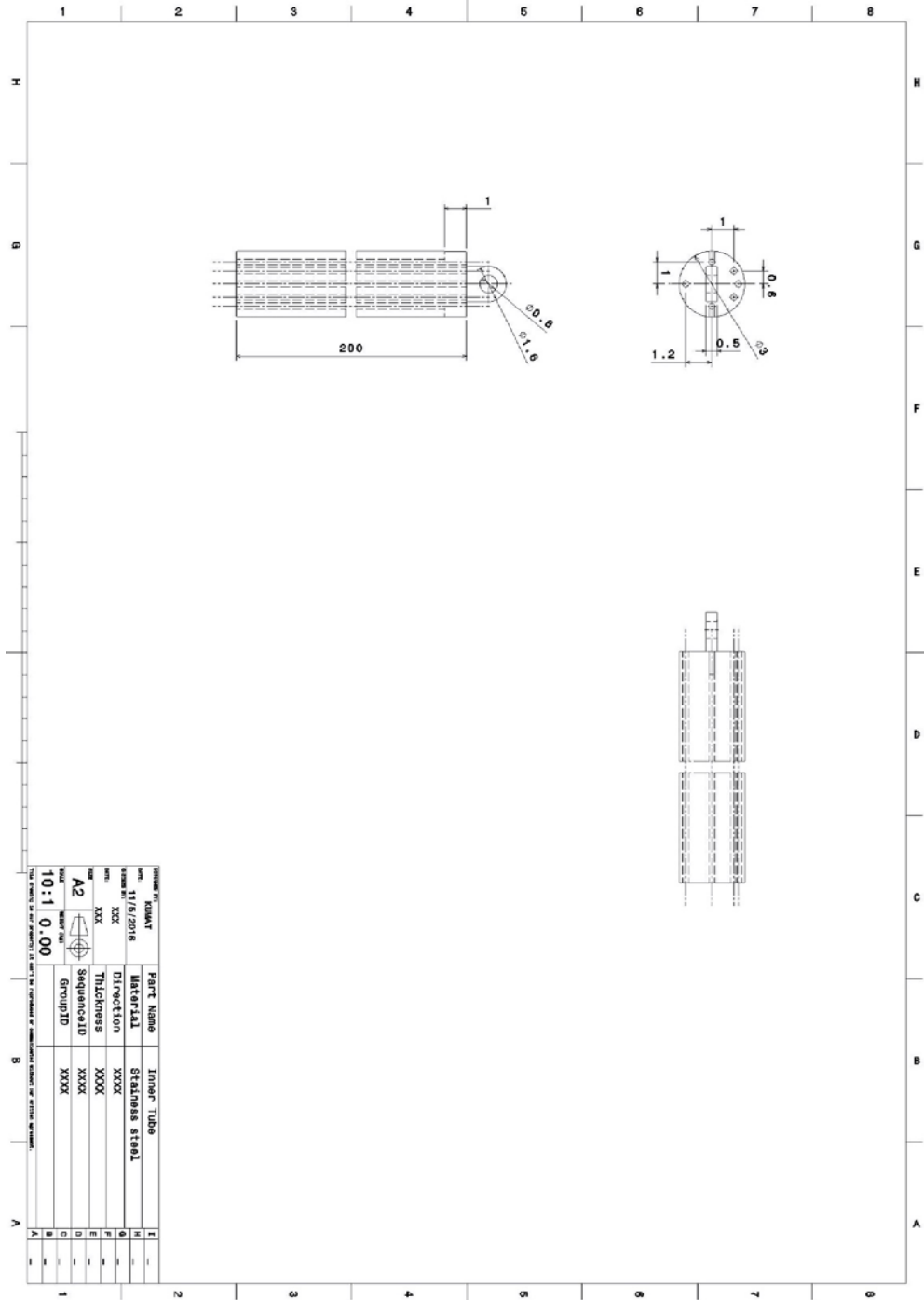
The calibration of the sensor prototype was performed using the Acrylonitrile Butadiene Styrene (ABS) material and aluminum for the beam component of the sensor assembly as discussed in Section 4.1.3. For the actual model, the aluminum beam needs to be replaced with medical grade stainless steel beam.

The strain experienced by the beam of the sensor assembly mentioned in Section 3.2.2 was in the order of magnitude of around $10 \mu\epsilon$. Semiconductor strain gauges can be investigated as an alternative to metal foil strain gauges. These strain gauges are suitable for small strain application, such as in the current research [50]. The overall dimension of the recommended semi-conductor bar shaped strain gauge is approximately 0.7 mm in length and 0.3 mm wide. Moreover the gauge factor for this strain gauge is approximately 155. This gauge factor is approximately 74 times larger than the metal foil strain gauge [50].

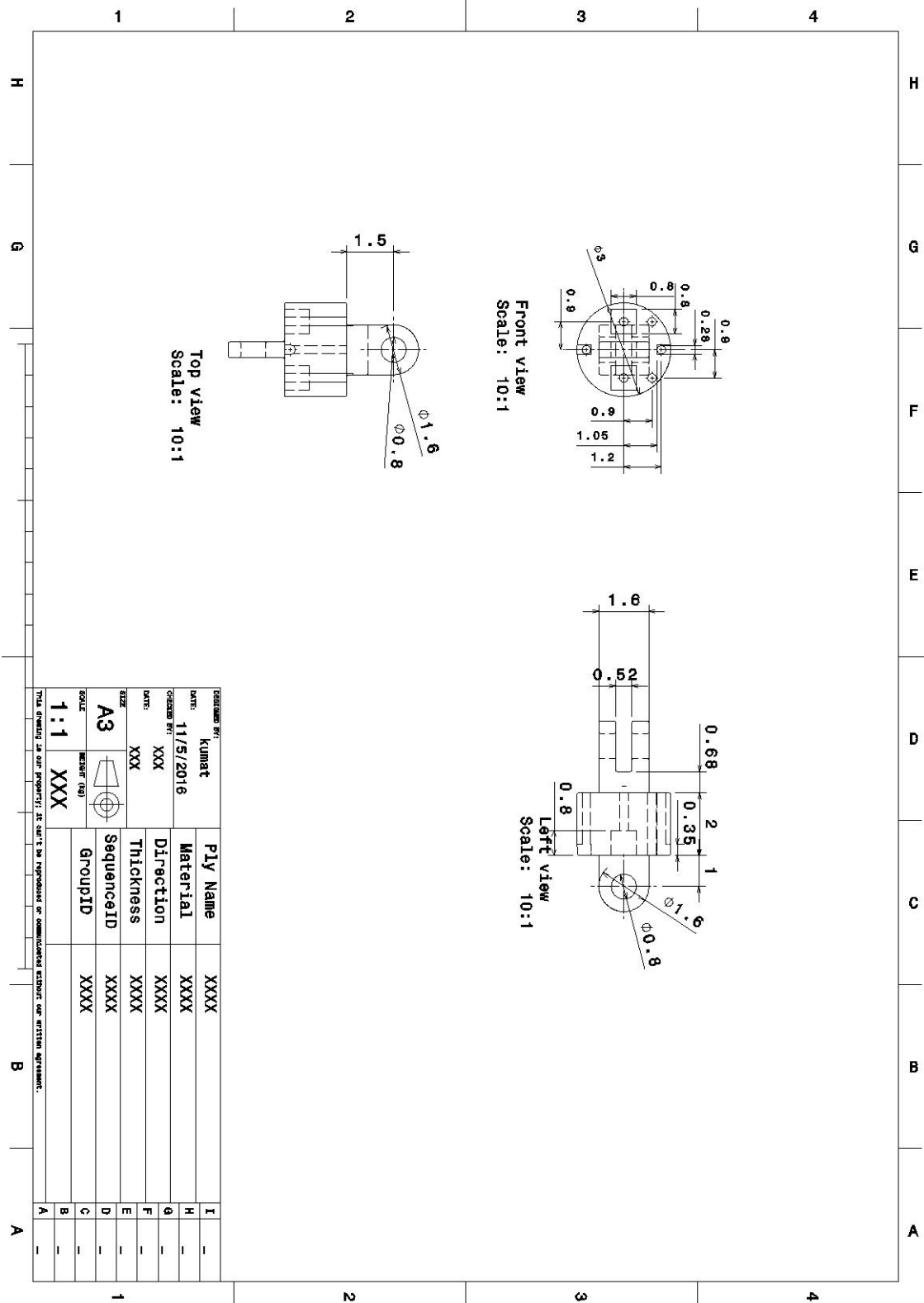
Appendix A

Part Drawings

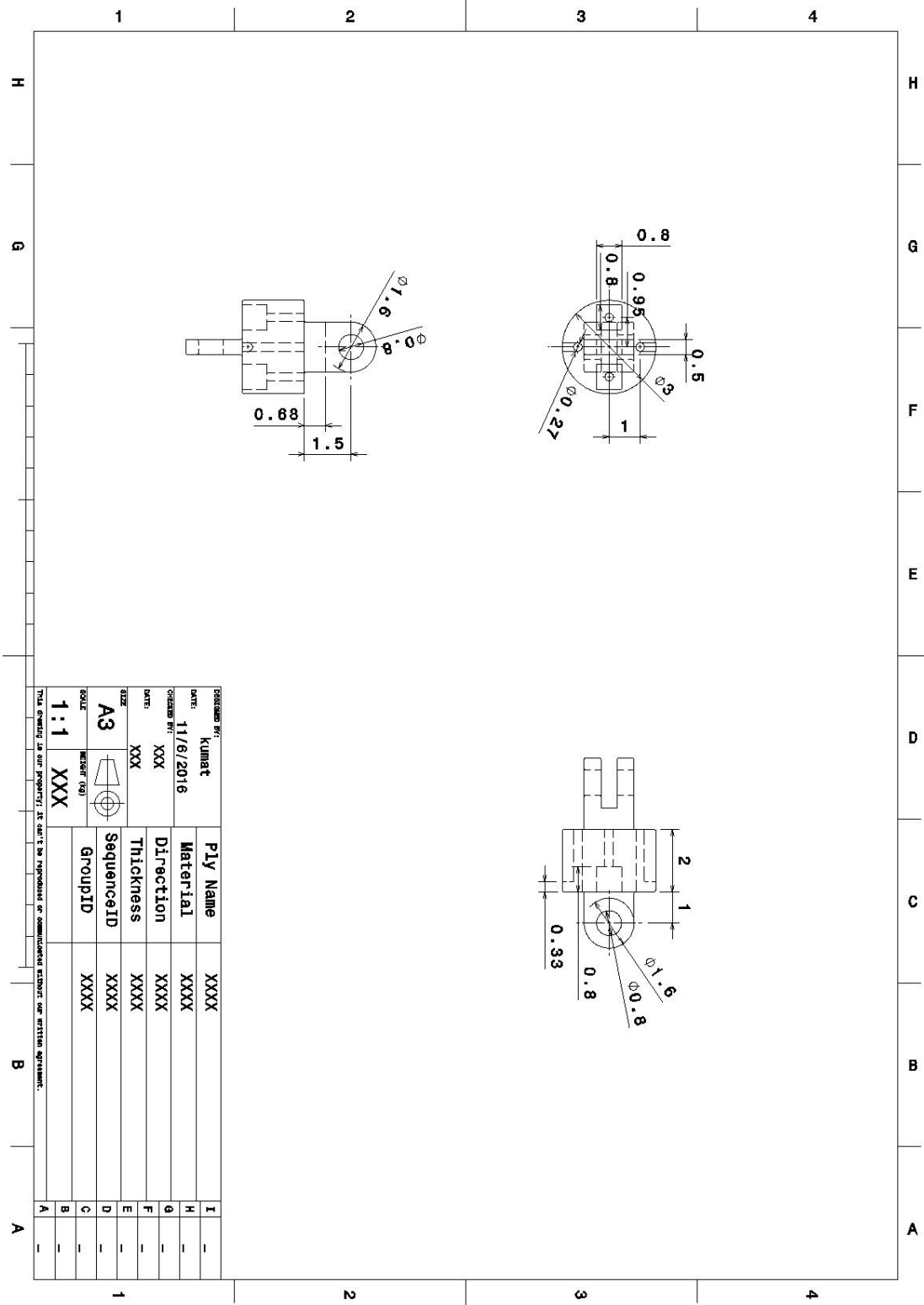
A.1 Inner Tube



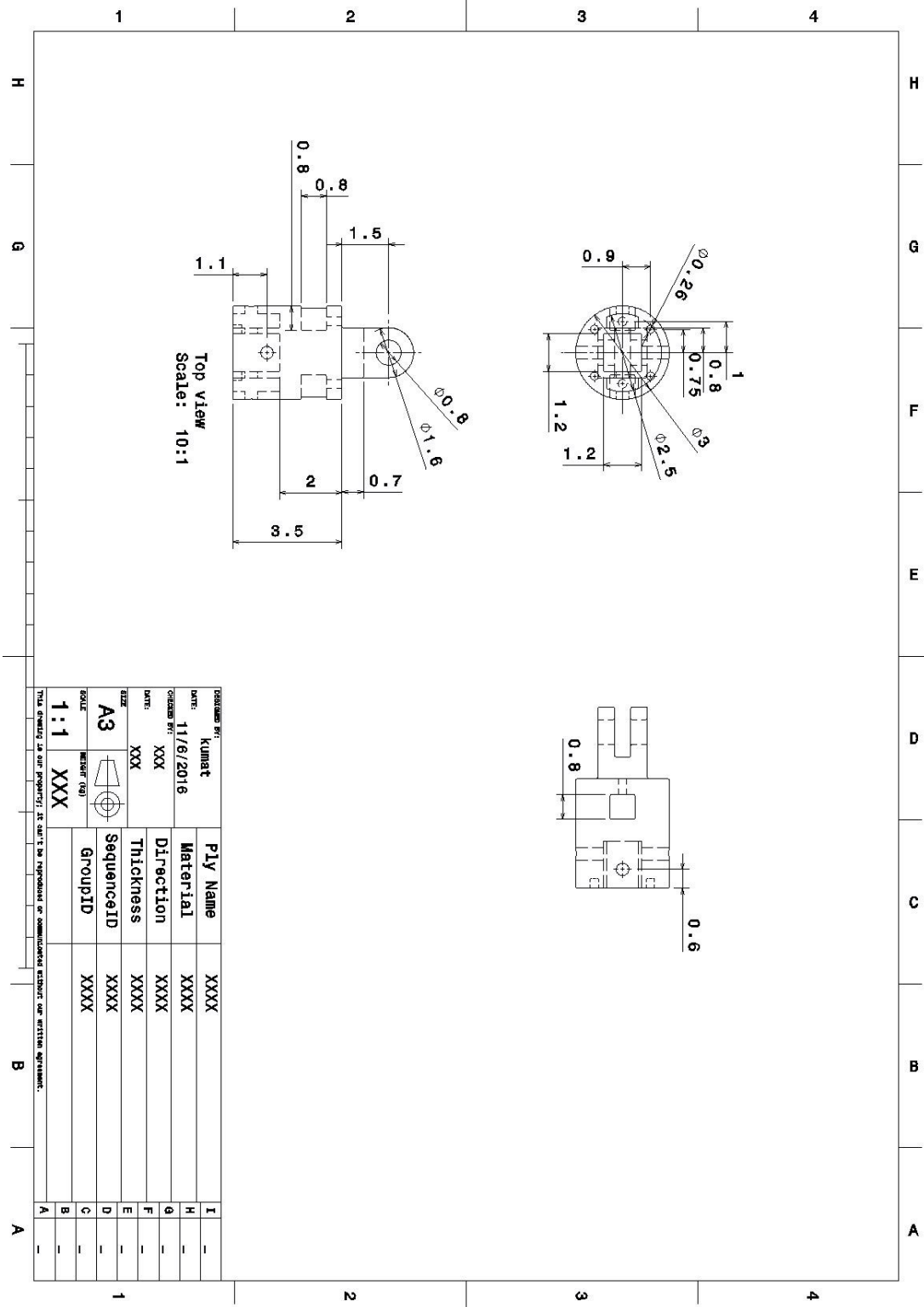
A.2 Link 2A



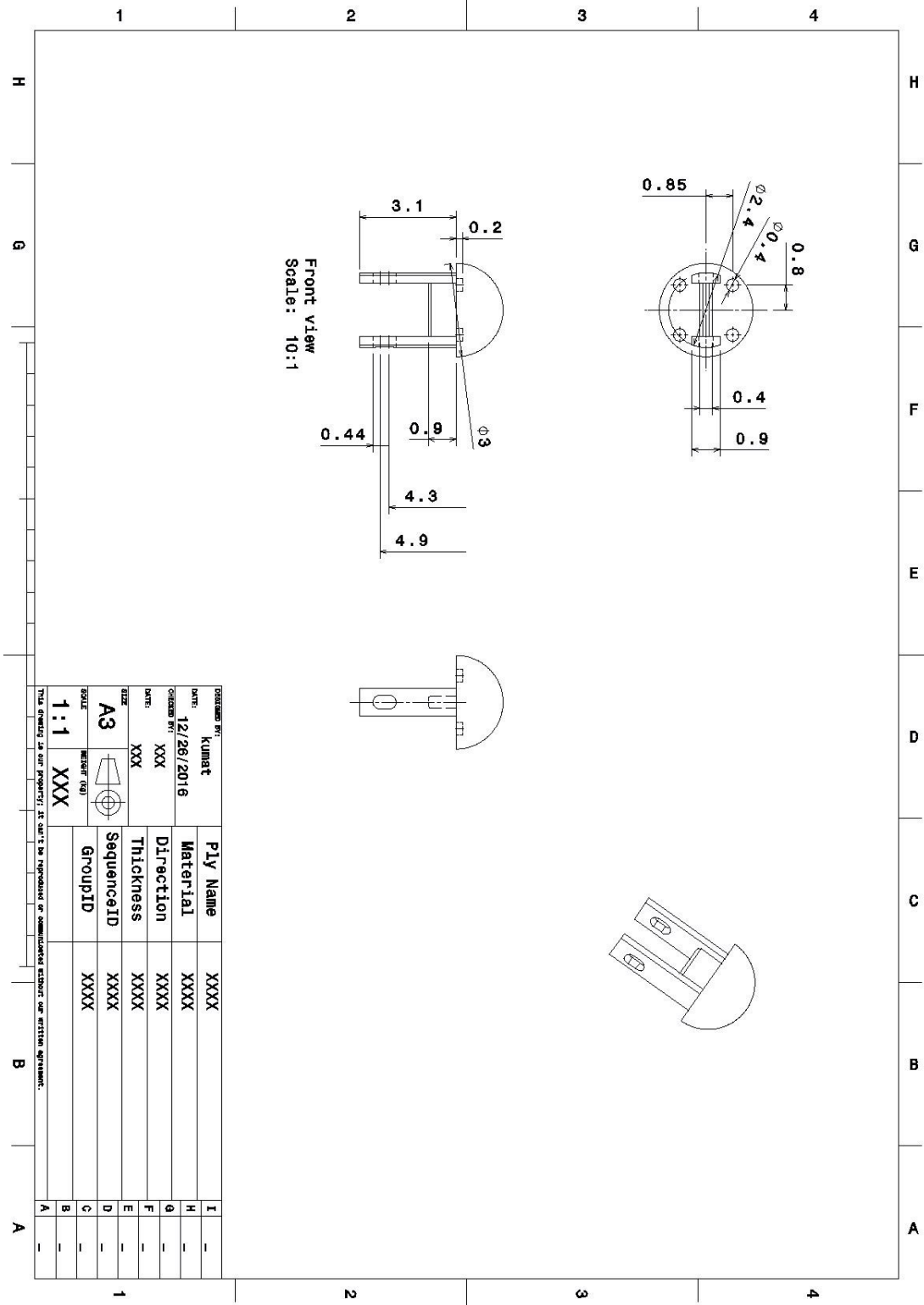
A.3 Link 2B



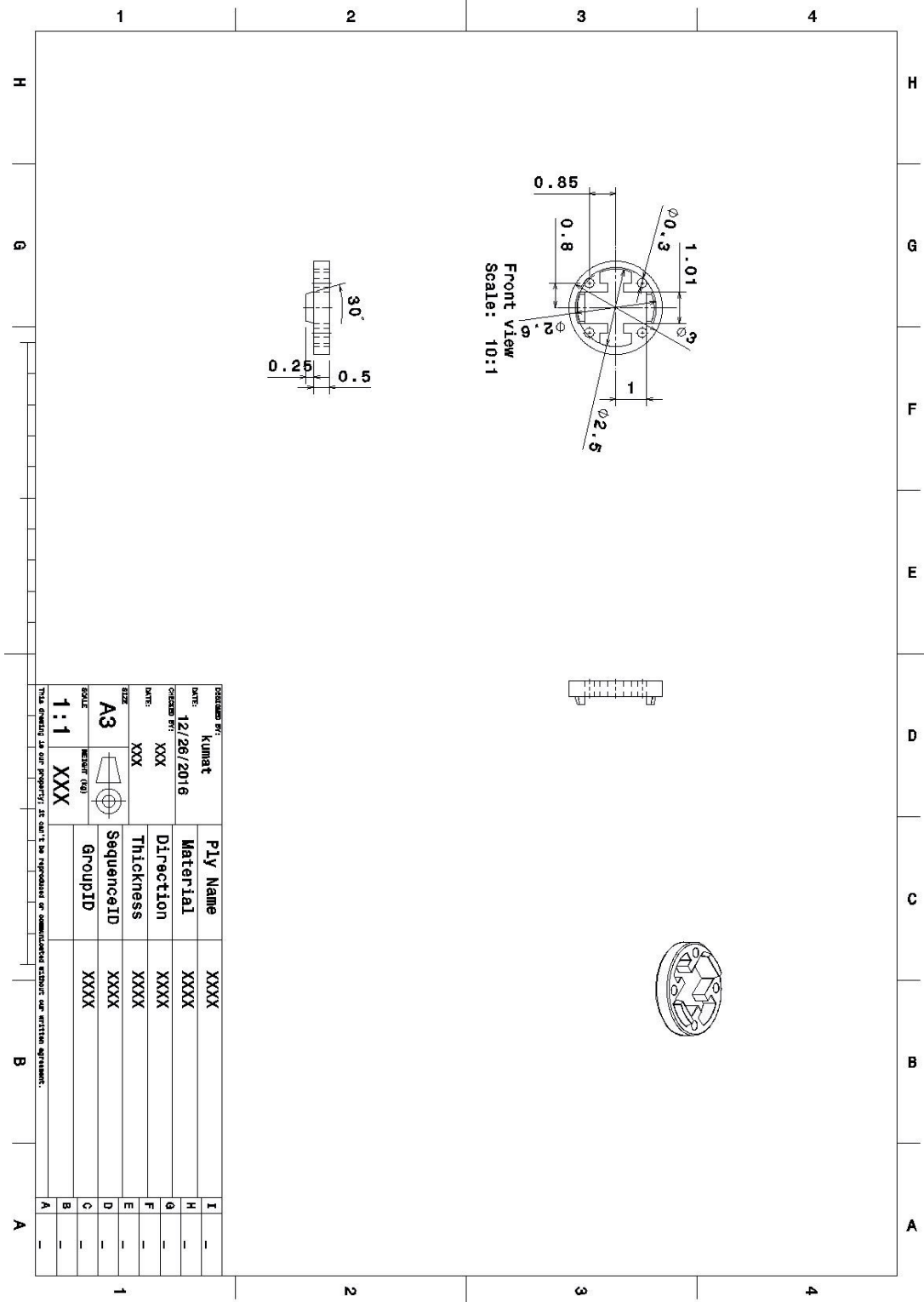
A.4 Sensor Support



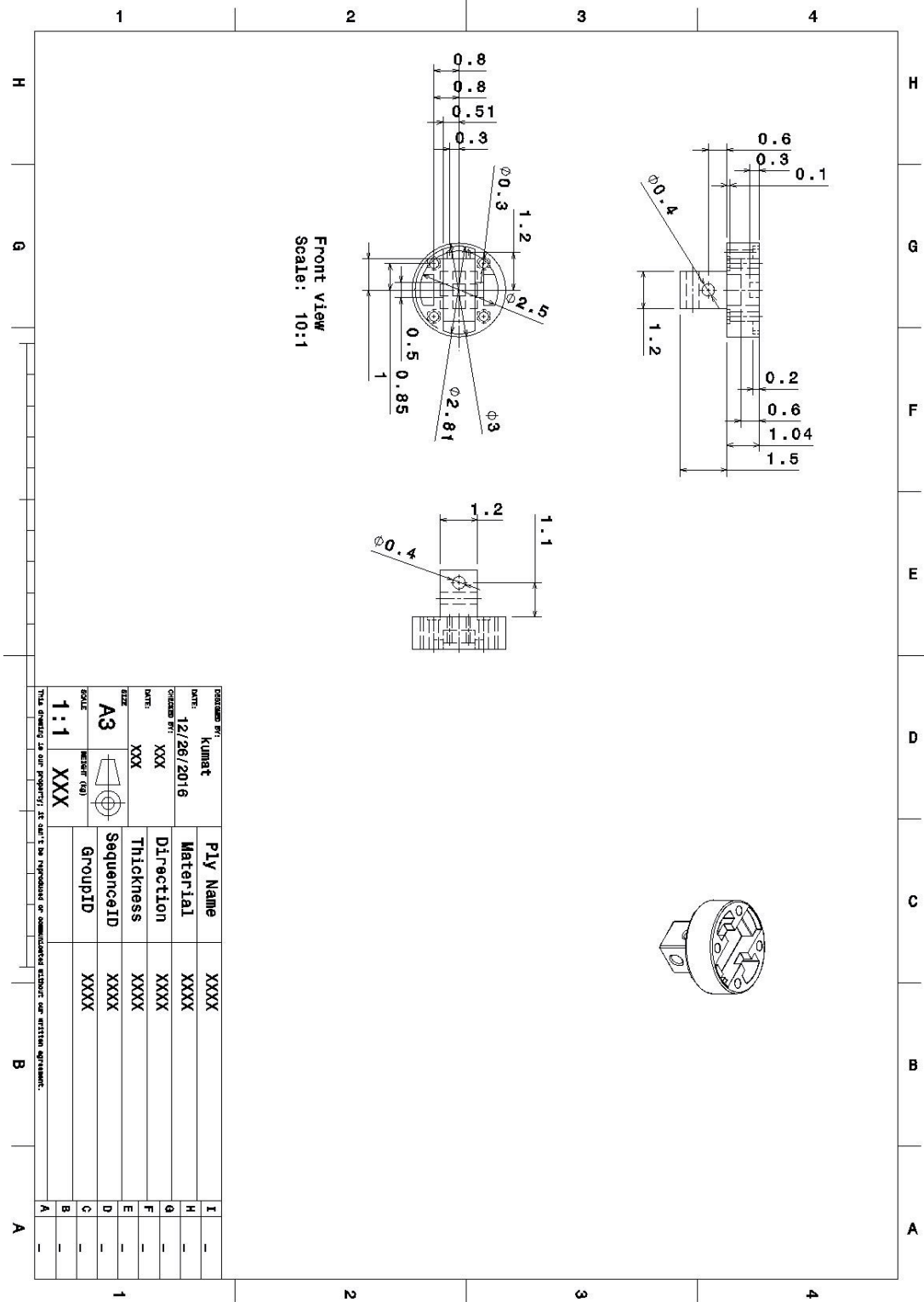
A.5 Sensor Head



A.6 Upper Clamp



A.7 Lower Clamp



Appendix B

Generalized Forward Kinematics Code

```
%% Read data from Excel file
clear all
close all
clc
data='mdhtable_mechanism3.xlsx'; % read the MDH table
sheet=4; % Extract the particular sheet number from the excel
file
[num, txt, raw] = xlsread(data, sheet, '', 'basic'); % Convert
the excel file in to matlab readable array
%% Initialization for the code
n=size(raw);
H=eye(4);
%% Define symbol
pi=sym('pi');
%% Distinguish between syms and number entries from extracted
data
for i=3:n(1,1) % Considering only required data
    for j=6:n(1,2) %Starting from 'a' parameter of MDH of
columns in raw
        entry=cell2mat(raw(i,j));
        if isnumeric(entry)
            num=num2cell(entry);
            raw{i,j}=num;
        else
            raw{i,j}=sym(entry);
        end
    end
end

%% Create a Matrix for MDH parameter from the extracted data
for k=6:n(1,2) % Column
    for l=3:n(1,1) % Row
        if isequal(k,6)
            b{1-2}=(raw(l,k));
            a=[b{:}];
        end
        if isequal(k,7)
            c{1-2}=(raw(l,k));
            al=[c{:}];
        end
        if isequal(k,8)
            b{1-2}=(raw(l,k));
        end
    end
end
```

```

        d=[b{:}];
    end
    if isequal(k,9)
        c{1-2}=(raw(1,k));
        th=[c{:}];
    end
end
end
clear i j k l b c num % clear variable so these can be used
again

%% Create cos and sine terms
for i=1:length(a)
    if isequal(class(th{i}), 'sym')
        ct(i)=cos(sym(th{i}));
        st(i)=sin(sym(th{i}));
    end
    if isequal(class(th{i}), 'cell')
        ct(i)=cos(cell2mat(th{i}));
        st(i)=sin(cell2mat(th{i}));
    end

    if isequal(class(al{i}), 'sym')
        cal(i)=cos(sym(al{i}));
        sal(i)=sin(sym(al{i}));
    end
    if isequal(class(al{i}), 'cell')
        cal(i)=cos(cell2mat(al{i}));
        sal(i)=sin(cell2mat(al{i}));
    end
end
end
%% Create a(i) Vector
for i=1:length(a)
    if isequal(class(a{i}), 'cell')
        E(i)=(a{i}); % Create a dummy variable to convert from
cell to double
        F=cell2mat(E(i));
        a{i}=sym(F);
    end
end
a=[a{:}];

%% Creat d(i) Vector
for i=1:length(a)
    if isequal(class(d{i}), 'cell')
        E(i)=(d{i}); % Create a dummy variable to convert from
cell to double

```

```

        F=cell2mat(E(i));
        d{i}=sym(F);
    end
end
d=[d{:}];

%% Homogenous Transformation Matrix
clear i
for i=1:length(a)
    fprintf('Joint Number %d\n',i)
    T=[ct(i),          -st(i),          0,          a(i)
        st(i)*cal(i),      ct(i)*cal(i),      -sal(i),
d(i)*(-sal(i))          st(i)*sal(i),      ct(i)*sal(i),      cal(i),
d(i)*cal(i)            0,          0,          0,          1];
    T=simplify(T);
    disp(T)
    TT{i}=T;
    H=H*TT{i};
end
fprintf('Homogenous Transformation Matrix is \n')
H=simplify(H);

%% Simplify H Matrix
digits(5);
Q=vpa(H);
disp(Q)
for i=1:length(a)
    IT{i}=Inversematrix(TT{i});
end

```

Appendix C

Inverse Kinematics Code

```
clc
clearvars -except H
pi=sym('pi');
%% Pre defined MDH fixed parameters that will be used to select
the solution set
L1=200;
L2=4;
L3=4;
L4=4;
syms nx ny nz qx qy qz ax ay az px py pz
% q=[ax qx nx px
%     ay qy ny py
%     az qz nz pz
%     0 0 0 1];
q=H;
q=vpa(q);
fprintf('The given Homogenous Transformation matrix is \n')
disp(q);
%% Assign joint limits:-
T1mx=degtorad(91);
T1mn=degtorad(-91);
T2mx=degtorad(91);
T2mn=degtorad(-91);
T3mx=degtorad(91);
T3mn=degtorad(-91);
clear a l gm a b c d e f g h i j k l m n t1
%% Find theta 2
ss=(q(3,1)^2)+(q(3,2)^2);
c1=sqrt(1-((q(3,1)^2)+(q(3,2)^2)));
c2=-sqrt(1-((q(3,1)^2)+(q(3,2)^2)));
t2(1,1)=atan2(sqrt(ss),c1);
t2(2,1)=atan2(sqrt(ss),c2);
t2(3,1)=atan2(-sqrt(ss),c1);
t2(4,1)=atan2(-sqrt(ss),c2);
t2=simplify(t2);
theta2=radtodeg(t2);
clear i
% Assign Joint limits for t2
clear i j k
for i=1:length(t2)
    if ge(double(subs(t2(i,1))),T2mx)
        le(double(subs(t2(i,1))),T2mn)
            theta2(i,:)=(NaN);
    end
end
```

```

        end
    end
    theta2=simplify(theta2);
    t2=degtorad(theta2);
    %% If Theta 2 is zero
    if isequal (double(q(3,3)^2),1)
        clear i j k s13 c13 t1
        % Find theta 1
        for i=1:length(t2)
            s1=(q(2,4)-(L4*q(2,1)))/(L2+L3);
            c1=sqrt(1-((s1)^2));
            c2=-sqrt(1-((s1)^2));
            t1(i,1)=atan2(s1,c1);
            t1(i+length(t2),1)=atan2(s1,c2);
        end
        t1=simplify(t1);
        theta1=radtodeg(t1);
        % Assign Joint limits for t1
        for i=1:length(t1)
            if ge(double(subs(t1(i,1))),T1mx) ||
le(double(subs(t1(i,1))),T1mn)
                theta1(i,:)=(NaN);
            end
        end
        theta1=simplify(theta1);
        t1=degtorad(theta1);
        % Find theta3
        for i=1:(length(t2)-2)
            for j=i+2:length(t1)
                t3(j,1)=(atan2(q(2,1),q(1,1)))-t1(j,1);
                t3(j+length(t1),1)=(atan2(q(2,1),q(1,1)))-
t1(j,1);
            end
        end
        t3=simplify(t3);
        theta3=radtodeg(t3);
        % Assign Joint limits for t3
        for i=1:length(t3)
            if ge(double(subs(t3(i,1))),T3mx) ||
le(double(subs(t3(i,1))),T3mn)
                theta3(i,:)=(NaN);
            end
        end
        theta3=simplify(theta3);
        t3=degtorad(theta3);
    else
        %% If theta 2 has any value except 0

```

```

    % Find theta 3
clear cc s1 s2 c ss b
for i=1:length(t2)
    c(i,1)=(cos(t2(i,1)))^2;
    b=(q(1,1)^2)+(q(2,1)^2);
    if isequal (double(b),1) && isequal (double(c(i,1)),1)
        cc(i,1)=1;
    else
        cc(i,1)=(b-1)/(c(i,1)-1);
    end
    s1(i,1)=sqrt(1-cc(i,1));
    s2(i,1)=-sqrt(1-cc(i,1));
    t3(i,1)=atan2(s1(i,1),sqrt(cc(i,1)));
    t3((i+length(t2)),1)=atan2(s2(i,1),sqrt(cc(i,1)));
    t3((i+2*length(t2)),1)=atan2(s1(i,1),-sqrt(cc(i,1)));
    t3((i+3*length(t2)),1)=atan2(s2(i,1),-sqrt(cc(i,1)));
end
t3=simplify(t3);
theta3=radtodeg(t3);
clear i
% Assign Joint limits for t3
for i=1:length(t3)
    if ge(double(subs(t3(i,1))),T3mx)
le(double(subs(t3(i,1))),T3mn)
        theta3(i,:)=(NaN);
    end
end
theta3=simplify(theta3);
t3=degtorad(theta3);
% Find theta 1
clear i j k a b c
for i=1:length(t2)
    for j=i+4:(length(t3))
        a=1;
        b=1;
        c=(q(1,3)+q(2,3))/sin(t2(i,1));
    if ((double((b^2)+(a^2)-(c^2)))<0)
        t1(j,1)=[NaN];
        t1(j+length(t3),1)=[NaN];
    else
        t1(j,1)=2*atan2((b+sqrt(((b)^2)+((a)^2)-
((c)^2))), (a+c));
        t1(j+length(t3),1)=2*atan2((b-sqrt(((b)^2)+((a)^2)-
((c)^2))), (a+c));
    end
end
end
end

```

||

```

t1=simplify(t1);
thetal=radtodeg(t1);
% Assign Joint limits for t1
for i=1:length(t1)
    if ge(double(subs(t1(i,1))),T1mx)
le(double(subs(t1(i,1))),T1mn)
        thetal(i,:)=(NaN);
    end
end
thetal=simplify(thetal);
t1=degtorad(thetal);
end
%% Selection of the Solution
clear i j k l m n J1 J2 J3
syms m n o
J1=max(abs(T1mx),abs(T1mn));
J2=max(abs(T2mx),abs(T2mn));
J3=max(abs(T3mx),abs(T3mn));
maxsum=J1+J2+J3;
tsum=0;
Fval=[m n o];
maxsum=radtodeg(maxsum);
xxx=0;
% All Possible solution sets
if (length(t3)>length(t1))
    for i=1:length(theta2)
        if ~isnan(theta2(i,1))
            for j=i:4:length(thetal)
                if ~isnan(thetal(j,1))
                    for k=j:8:length(theta3)
                        if ~isnan(theta3(k,1))
                            set(k,:)=[j i k];
                            xxx=1;
                        end
                    end
                end
            end
        end
    end
end
if (length(t3)<length(t1))
    for i=1:length(t2)
        if ~isnan((theta2(i,1)))
            for j=i:4:length(theta3)
                if ~isnan((theta3(j,1)))
                    for k=j:16:length(thetal)
                        if ~isnan((thetal(k,1)))

```

||

```

set(k,:)=[k i j];
xxx=1;
end
end
end
end
end
end
end
if isequal(xxx,1)
set(all(~set,2),:)=[];
%% Choose proper set and display solution
clear i j k l sz
sz=size(set); % extract the size of solution set
k=sz(1,1); % No. of valid solution sets
l=sz(1,2); % No. of D.O.F.
for i=1:k
    NT(1,i)=theta1(set(i,1));
    NT(2,i)=theta2(set(i,2));
    NT(3,i)=theta3(set(i,3));
end
%% Fixed MDH parameters
clear i j o z
z=0;
a=[L1,L2,L3,L4];
al=[0,3*pi/2,pi/2,0];
d=[0,0,0,0];
NT=degtorad(NT');
for o=1:k % k is number of solution sets
    NH=eye(4);
for i=1:length(a)
    if le(i,l)
        ct(i)=cos((NT(o,i)));
        st(i)=sin((NT(o,i)));
    else
        ct(i)=cos(0);
        st(i)=sin(0);
    end
end
end
for j=1:length(al)
    cal(j)=cos((al(j)));
    sal(j)=sin((al(j)));
end

%% Homogenous Transformation Matrix
clear i
for i=1:length(a)

```



```

        T=[ct(i),          -st(i),          0,          a(i)
           st(i)*cal(i),   ct(i)*cal(i),   -sal(i),   d(i)*(-
sal(i))
           st(i)*sal(i),          ct(i)*sal(i),          cal(i),
d(i)*cal(i)
           0,          0,          0,          1];
        T=simplify(T);
        TT{i}=T;
        NH=NH*TT{i};
end
digits (6)
NH=simplify(NH);
%% Compare New homogenous and given Homogenous
digits(7)
if le(double((vpa(NH))-(vpa(H))),double(1.0e-3))
    z=1;
    SNH=NH;
    FNT1=radtodeg(NT(o,1));
    FNT1=simplify(FNT1);
    FNT2=radtodeg(NT(o,2));
    FNT2=simplify(FNT2);
    FNT3=radtodeg(NT(o,3));
    FNT3=simplify(FNT3);
end
end
%% Print Final Answer
if isequal(z,1)
    fprintf('The desired H matrix has Theta1 (deg): \n')
    disp(round(FNT1))

    fprintf('The desired H matrix has Theta2 (deg): \n')
    disp(round(FNT2))

    fprintf('The desired H matrix has Theta3 (deg): \n')
    disp(round(FNT3))
end
if isequal(z,0)
    fprintf ('Plese verify the Final homogenous Matrix, Point
not in Workspace')
end
end
end

```

Appendix D

Jacobian Determinant

```
clc
close all
clearvars -except TT % where TT is the Final homogenous matrix
% syms Fx Fy Fz
L1=200; % Unit for length mm
L2=4.5;
L3=4.5;
L4=10;
Fx=-1; % units for force N
Fy=0;
Fz=0;
% In the for loop below(length(TT)+1)= 5 is nothing but frame 4
and similarly going to
% 1 is nothing but frame 0
for i=length(TT)+1:-1:1
    if isequal(i,length(TT)+1)
        R{i}=eye(3,3);
        F{i}=[Fx;Fy;Fz];
        N{i}=zeros(3,1);
    else
        [R{i},P{i}]=RoPo(TT{i});
        F{i}=R{i}*F{i+1};
        N{i}=(R{i}*N{i+1}+cross(P{i},F{i}));
    end
end
clear i
for i=1:length(TT)
    N{i}=simplify(N{i});
    F{i}=simplify(F{i});
    N{i}=vpa(N{i});
    F{i}=vpa(F{i});
    fprintf('Torque at Frame %d\n',i-1)
    disp(N{i})
end

%% Find Maximum torque on joints within the given range of theta's
counter=0;
% t3=pi/2;
% t2=pi/2;
for t3=-pi/2:pi/6:pi/2 %from -90 to 90 with increment of 30
    for t2=-pi/6:pi/6:pi/2
        for t1=-pi/2:pi/6:pi/2
            for i=1:(length(N)-1)
```

```

        M{i}=subs(N{i});
        if isequal(i,(length(N)-1))
            Np{counter+1}=vpa(M);
            Mp=vpa(Np);
            v{counter+1}=vpa([radtodeg(t1) radtodeg(t2)
radtodeg(t3)]);
            counter=counter+1;
        end
    end
end
end
clear i X Y Z t
for i=1:length(Np)
    X{i,1}=Np{i}(3,2);
    S{i,1}=(v{i}(1,1));
end
clear i
for i=1:length(Np)
    Y{i,1}=Np{i}(2,3);
end
clear i
for i=1:length(Np)
    Z{i,1}=Np{i}(3,4);
end
S=vpa(S);
X=vpa(X);
Y=vpa(Y);
Z=vpa(Z);
figure(1)
grid on
hold on
xlabel ('\theta (deg)');
ylabel ('\tau (Nmm)');
p1=plot(S,X,'-rs','Linewidth',1.5);
hold on
p2=plot(S,Y,'-bo','Linewidth',1.5);
hold on
p3=plot(S,Z,'-kx','Linewidth',1.5);
hold off
legend([p1 p2 p3],'Torque at \theta_1','Torque at
\theta_2','Torque at \theta_3')
title('Torques at Joints when Force of -0.4 N is applied in normal
direction of sensor frame')

```

Appendix E

Sensor Experiment data

| Srno | Load(gms) | vin | v1 | v2 | Amp/Vout abs vout | mpificatio | Vout | out average | R1 | R2 | R4 | gauge resi/gauge fact(1+R2/R3+Vout/Vin+R1R4)/l | Strain | strain | Theoretical Strain | | | | |
|------|-----------|-----|----------|---------|-------------------|------------|------|-------------|--------|-----|-----|--|--------|--------|--------------------|----------|----------|----------|----------|
| 1 | | 5 | -0.00010 | -0.0004 | -0.0003 | 0.0003 | 1 | -0.0003 | 120 | 120 | 120 | 120 | 2.09 | 5760 | -0.00006 | -0.0288 | 0.000115 | | |
| 2 | | 5 | -0.00010 | -0.0004 | -0.0003 | 0.0003 | 1 | -0.0003 | 120 | 120 | 120 | 120 | 2.09 | 5760 | -0.00006 | -0.0288 | 0.000115 | | |
| 3 | 100 | 5 | -0.00010 | -0.0005 | -0.0004 | 0.0004 | 1 | -0.0004 | 0.0004 | 120 | 120 | 120 | 2.09 | 5760 | -0.00008 | -0.03839 | 0.000153 | 1.38E-04 | 1.07E-04 |
| 4 | | 5 | -0.00010 | -0.0005 | -0.0004 | 0.0004 | 1 | -0.0004 | 120 | 120 | 120 | 120 | 2.09 | 5760 | -0.00008 | -0.03839 | 0.000153 | | |
| 5 | | 5 | -0.00010 | -0.0005 | -0.0004 | 0.0004 | 1 | -0.0004 | 120 | 120 | 120 | 120 | 2.09 | 5760 | -0.00008 | -0.03839 | 0.000153 | | |
| 6 | | 5 | -0.00020 | -0.0010 | -0.0008 | 0.0008 | 1 | -0.0008 | 120 | 120 | 120 | 120 | 2.09 | 5760 | -0.00016 | -0.07678 | 0.000306 | | |
| 7 | | 5 | -0.00030 | -0.0010 | -0.0007 | 0.0007 | 1 | -0.0007 | 120 | 120 | 120 | 120 | 2.09 | 5760 | -0.00014 | -0.06718 | 0.000268 | | |
| 8 | 200 | 5 | -0.00030 | -0.0010 | -0.0007 | 0.0007 | 1 | -0.0007 | 0.0007 | 120 | 120 | 120 | 2.09 | 5760 | -0.00014 | -0.06718 | 0.000268 | 2.76E-04 | 2.08E-04 |
| 9 | | 5 | -0.00030 | -0.0010 | -0.0007 | 0.0007 | 1 | -0.0007 | 120 | 120 | 120 | 120 | 2.09 | 5760 | -0.00014 | -0.06718 | 0.000268 | | |
| 10 | | 5 | -0.00030 | -0.0010 | -0.0007 | 0.0007 | 1 | -0.0007 | 120 | 120 | 120 | 120 | 2.09 | 5760 | -0.00014 | -0.06718 | 0.000268 | | |
| 11 | | 5 | -0.00030 | -0.0012 | -0.0009 | 0.0009 | 1 | -0.0009 | 120 | 120 | 120 | 120 | 2.09 | 5760 | -0.00018 | -0.08637 | 0.000344 | | |
| 12 | | 5 | -0.00030 | -0.0012 | -0.0009 | 0.0009 | 1 | -0.0009 | 120 | 120 | 120 | 120 | 2.09 | 5760 | -0.00018 | -0.08637 | 0.000344 | | |
| 13 | 300 | 5 | -0.00040 | -0.0012 | -0.0008 | 0.0008 | 1 | -0.0008 | 0.0009 | 120 | 120 | 120 | 2.09 | 5760 | -0.00016 | -0.07678 | 0.000306 | 3.44E-04 | 3.10E-04 |
| 14 | | 5 | -0.00040 | -0.0015 | -0.0011 | 0.0011 | 1 | -0.0011 | 120 | 120 | 120 | 120 | 2.09 | 5760 | -0.00022 | -0.10555 | 0.000421 | | |
| 15 | | 5 | -0.00040 | -0.0012 | -0.0008 | 0.0008 | 1 | -0.0008 | 120 | 120 | 120 | 120 | 2.09 | 5760 | -0.00016 | -0.07678 | 0.000306 | | |
| 16 | | 5 | -0.00040 | -0.0016 | -0.0012 | 0.0012 | 1 | -0.0012 | 120 | 120 | 120 | 120 | 2.09 | 5760 | -0.00024 | -0.11514 | 0.000459 | | |
| 17 | | 5 | -0.00040 | -0.0016 | -0.0012 | 0.0012 | 1 | -0.0012 | 120 | 120 | 120 | 120 | 2.09 | 5760 | -0.00024 | -0.11514 | 0.000459 | | |
| 18 | 400 | 5 | -0.00030 | -0.0015 | -0.0012 | 0.0012 | 1 | -0.0012 | 0.0012 | 120 | 120 | 120 | 2.09 | 5760 | -0.00024 | -0.11514 | 0.000459 | 4.44E-04 | 4.10E-04 |
| 19 | | 5 | -0.00030 | -0.0015 | -0.0012 | 0.0012 | 1 | -0.0012 | 120 | 120 | 120 | 120 | 2.09 | 5760 | -0.00024 | -0.11514 | 0.000459 | | |
| 20 | | 5 | -0.00040 | -0.0014 | -0.0010 | 0.0010 | 1 | -0.0010 | 120 | 120 | 120 | 120 | 2.09 | 5760 | -0.00022 | -0.09596 | 0.000393 | | |
| 21 | | 5 | -0.00010 | -0.0019 | -0.0018 | 0.0018 | 1 | -0.0018 | 120 | 120 | 120 | 120 | 2.09 | 5760 | -0.00036 | -0.17268 | 0.000688 | | |
| 22 | | 5 | -0.00010 | -0.0016 | -0.0015 | 0.0015 | 1 | -0.0015 | 120 | 120 | 120 | 120 | 2.09 | 5760 | -0.0003 | -0.14991 | 0.000574 | | |
| 23 | 605 | 5 | -0.00020 | -0.0016 | -0.0014 | 0.0014 | 1 | -0.0014 | 0.0017 | 120 | 120 | 120 | 2.09 | 5760 | -0.00028 | -0.13432 | 0.000556 | 6.50E-04 | 6.07E-04 |
| 24 | | 5 | -0.00020 | -0.0022 | -0.0020 | 0.0020 | 1 | -0.0020 | 120 | 120 | 120 | 120 | 2.09 | 5760 | -0.0004 | -0.19185 | 0.000755 | | |
| 25 | | 5 | -0.00020 | -0.0020 | -0.0018 | 0.0018 | 1 | -0.0018 | 120 | 120 | 120 | 120 | 2.09 | 5760 | -0.00036 | -0.17268 | 0.000688 | | |

References

- [1] D. Shaw, *Volume of Human bladder*, Glenn Elert, 2001.
- [2] T. Taylor, *Urinary System*.
- [3] "Bladder Cancer," *National Cancer institute*, vol. 10, p. 1–1, Jul 2010.
- [4] M. Lekka, P. Laidler, D. Gil, J. Lekki, Z. Stachura and A. Z. Hryniewicz, "Elasticity of normal and cancerous human bladder cells studied by scanning force microscopy," *European Biophysics Journal*, vol. 28, pp. 312-316, 1999.
- [5] H. Gray, "Anatomy of the human body. 1918," *Bartleby. com*, 1821.
- [6] R. G. Hudson, M. J. Conlin and D. H. Bagley, "Ureteric access with flexible ureteroscopes: effect of the size of the ureteroscope," *BJU international*, vol. 95, pp. 1043-1044, 2005.
- [7] K. Stav, D. Leibovici, E. Goren, A. Livshitz, Y. I. Siegel, A. Lindner and A. Zisman, "Adverse effects of cystoscopy and its impact on patients' quality of life and sexual performance.," *The Israel Medical Association journal: IMAJ*, vol. 6, pp. 474-478, 2004.
- [8] C.-J. Chuong, M. Ma, R. C. Eberhart and P. Zimmern, "Viscoelastic properties measurement of the prolapsed anterior vaginal wall: a patient-directed methodology," *European Journal of Obstetrics & Gynecology and Reproductive Biology*, vol. 173, pp. 106-112, 2014.
- [9] R. N. Miftahof and H. G. Nam, *Biomechanics of the human urinary bladder*, Springer Science & Business Media, 2013.
- [10] R. N. Miftahof and H. G. Nam, "Investigations into Biomechanics of the Bladder," in *Biomechanics of the Human Urinary Bladder*, Springer, 2013, pp. 25-39.

- [11] A. J. Van Beek, A finite element model of the urinary bladder, Stan Ackermans Instituut, 1997.
- [12] R. O'Rahilly and F. Müller, Basic human anatomy: a regional study of human structure, WB Saunders Company, 1983.
- [13] W. Aref, *Anatomical components of continence mechanism in males*, American Urology association, 2012.
- [14] B. C. Gill, *Urinary Incontinence Relevant Anatomy*, 2015.
- [15] M. Greco, P. Marsillac, J. Vieira, M. Brito, A. Saud, R. Prinz and J. Pereira-Correia, "Searching for the Lost Ostium: A Morphometric Analysis of the Ureteral Ostia Distribution in Normal and Thickened Bladders and Its Applications in Endourology," 2013.
- [16] S. E. Dahms, H. J. Piechota, R. Dahiya, T. F. Lue and E. A. Tanagho, "Composition and biomechanical properties of the bladder acellular matrix graft: comparative analysis in rat, pig and human," *British journal of urology*, vol. 82, pp. 411-419, 1998.
- [17] Unknown, *The urinary bladder*, Unknown.
- [18] G. M. Ghoniem, *Cystoscopy*, 2016.
- [19] J. Shah, "Endoscopy through the ages," *BJU international*, vol. 89, pp. 645-652, 2002.
- [20] R. Chou and T. Dana, "Screening adults for bladder cancer: a review of the evidence for the US preventive services task force," *Annals of internal medicine*, vol. 153, pp. 461-468, 2010.
- [21] S. Lewis, *Cystoscopy - Cell Test*, 2016.

- [22] M. B. Bush, B. Liedl, F. Wagenlehner and P. Petros, "A finite element model validates an external mechanism for opening the urethral tube prior to micturition in the female," *World Journal of Urology*, vol. 33, pp. 1151-1157, 2015.
- [23] A. Ali, M. H. Fouladi and B. Sahari, "A review of constitutive models for rubber-like materials," *American Journal of Engineering and Applied Sciences*, vol. 3, pp. 232-239, 2010.
- [24] B. L. Coolsaet, W. A. Van Duyl, R. Van Mastrigt and J. W. Schouten, "Viscoelastic properties of bladder wall strips.," *Investigative urology*, vol. 12, pp. 351-356, 1975.
- [25] S. Hwang and J. Ma, "Mechanical Characterization of Human Prostate".
- [26] H. Yamada, F. G. Evans and others, "Strength of biological materials," 1970.
- [27] P. A. L. S. Martins, A. L. Silva Filho, A. M. R. M. Fonseca, A. Santos, L. Santos, T. Mascarenhas, R. M. N. Jorge and A. J. M. Ferreira, "Uniaxial mechanical behavior of the human female bladder," *International urogynecology journal*, vol. 22, pp. 991-995, 2011.
- [28] C. Rubod, M. Brieu, M. Cosson, G. Rivaux, J.-C. Clay, L. de Landsheere and B. Gabriel, "Biomechanical Properties of Human Pelvic Organs," *Urology*, vol. 79, pp. 968.e17 - 968.e22, 2012.
- [29] M. Argungu, S. Bayram, B. Brook, B. Chakrabarti, R. H. Clayton, D. M. Daly, R. J. Dyson, C. Holloway, V. Manhas, S. Naire and others, "Modelling afferent nerve responses to bladder filling," *arXiv preprint arXiv:1510.03119*, 2015.
- [30] R. van Mastrigt, B. L. R. A. Coolsaet and W. A. Van Duyl, "Passive properties of the urinary bladder in the collection phase," *Medical and Biological Engineering and Computing*, vol. 16, pp. 471-482, 1978.

- [31] M. Wadham-Gagnon, P. Hubert, C. Semler, M. P. Paidoussis, M. Vézina and D. Lavoie, "Hyperelastic modeling of rubber in commercial finite element software (ANSYS™)," in *Proceedings of Conference on SAMPE 2006*, 2006.
- [32] M. Rackl, "Curve Fitting for Ogden, Yeoh and Polynomial Models," 2015.
- [33] C. Renaud, J.-M. Cros, Z.-Q. Feng and B. Yang, "The Yeoh model applied to the modeling of large deformation contact/impact problems," *International Journal of Impact Engineering*, vol. 36, pp. 659-666, 2009.
- [34] H. A. K. A. N. Oflaz and O. N. D. E. R. Baran, "A new medical device to measure a stiffness of soft materials," *Acta of Bioengineering and Biomechanics*, vol. 16, 2014.
- [35] X. Ye and W. J. Yoon, "Design of a bending mechanism for automated cystoscope," in *2012 IEEE International Conference on Automation Science and Engineering (CASE)*, 2012.
- [36] S. Kim, C. Laschi and B. Trimmer, "Soft robotics: a bioinspired evolution in robotics," *Trends in biotechnology*, vol. 31, pp. 287-294, 2013.
- [37] R. J. Webster and B. A. Jones, "Design and kinematic modeling of constant curvature continuum robots: A review," *The International Journal of Robotics Research*, 2010.
- [38] R. J. Webster, J. S. Kim, N. J. Cowan, G. S. Chirikjian and A. M. Okamura, "Nonholonomic modeling of needle steering," *The International Journal of Robotics Research*, vol. 25, pp. 509-525, 2006.
- [39] D. C. Rucker, B. A. Jones and R. J. Webster III, "A geometrically exact model for externally loaded concentric-tube continuum robots," *IEEE Transactions on Robotics*, vol. 26, pp. 769-780, 2010.

- [40] D. C. Rucker, R. J. Webster, G. S. Chirikjian and N. J. Cowan, "Equilibrium conformations of concentric-tube continuum robots," *The International journal of robotics research*, 2010.
- [41] P. Dupont, A. Gosline, N. Vasilyev, J. Lock, E. Butler, C. Folk, A. Cohen, R. Chen, G. Schmitz, H. Ren and others, "Concentric tube robots for minimally invasive surgery," in *hamlyn symposium on medical robotics*, 2012.
- [42] P. E. Dupont, J. Lock, B. Itkowitz and E. Butler, "Design and control of concentric-tube robots," *IEEE Transactions on Robotics*, vol. 26, pp. 209-225, 2010.
- [43] C. Sophocleous, E. G. Christoforou, P. S. Shiakolas, I. Seimenis, N. V. Tsekos and C. C. Doumanidis, "Development and initial testing of a prototype concentric tube robot for surgical interventions," in *Bioinformatics \& Bioengineering (BIBE), 2012 IEEE 12th International Conference on*, 2012.
- [44] P. Ravi, P. S. Shiakolas, J. C. Oberg, S. Faizee and A. K. Batra, "On the Development of a Modular 3D Bioprinter for Research in Biomedical Device Fabrication," in *ASME 2015 International Mechanical Engineering Congress and Exposition*, 2015.
- [45] J. J. Craig, *Introduction to robotics: mechanics and control*, vol. 3, Pearson Prentice Hall Upper Saddle River, 2005.
- [46] R. P. Paul, B. Shimano and G. E. Mayer, "Kinematic control equations for simple manipulators," *IEEE Transactions on Systems, Man, and Cybernetics*, vol. 11, pp. 449-445, 1981.
- [47] J. Black and G. Hastings, *Handbook of biomaterial properties*, Springer Science & Business Media, 2013.

- [48] R. K. Bansal, A textbook of Strength of Materials, Laxmi Publications, 2010.
- [49] A. F. & P. Association and A. W. Council, Beam Design Formulas with Shear and Moment Diagrams: Design Aid, 2007.
- [50] *Semiconductor Strain Gages at Micron Instruments.*
- [51] X. Wang, T. Geng, Y. Elsayed, C. Saaj and C. Lekakou, "A unified system identification approach for a class of pneumatically-driven soft actuators," *Robotics and Autonomous Systems*, vol. 63, pp. 136-149, 2015.
- [52] W. Wang, Y. Zhao and Q. Lin, "An integrated MEMS tactile tri-axial micro-force probe sensor for minimally invasive surgery," in *2009 IEEE 3rd International Conference on Nano/Molecular Medicine and Engineering*, 2009.
- [53] I. Vlastelica, D. Veljkovic, V. Rankovic, B. Stojanovic, M. Rosic and M. Kojic, "Modeling of Urinary bladder deformation within passive and active regimes," *Journ. of the Serbian Society for Computational Mechanics*, vol. 1, pp. 129-134, 2007.
- [54] J. U. L. I. A. N. VINCENT, Structural Biomaterials: Third Edition, STU - Student edition ed., Princeton University Press, 2012.
- [55] F. Urban, J. Kadlec, R. Vlach and R. Kuchta, "Design of a pressure sensor based on optical fiber Bragg grating lateral deformation," *Sensors*, vol. 10, pp. 11212-11225, 2010.
- [56] B. Trimmer, "A journal of soft robotics: why now?," *Soft Robotics*, vol. 1, pp. 1-4, 2014.
- [57] K. Totsu, Y. Haga and M. Esashi, "Ultra-miniature fiber-optic pressure sensor using white light interferometry," *Journal of Micromechanics and Microengineering*, vol. 15, p. 71, 2004.

- [58] J. Stoll, P. Novotny, R. Howe and P. Dupont, "Real-time 3D ultrasound-based servoing of a surgical instrument," in *Proceedings 2006 IEEE International Conference on Robotics and Automation, 2006. ICRA 2006.*, 2006.
- [59] K. Stav, D. Leibovici, E. Goren, A. Livshitz, Y. I. Siegel, A. Lindner and A. Zisman, "Adverse effects of cystoscopy and its impact on patients' quality of life and sexual performance.," *The Israel Medical Association journal: IMAJ*, vol. 6, pp. 474-478, 2004.
- [60] H. Sorkhi, M.-R. Navaeifar, H.-G. Nooreddini, R. Navaee, H. Shafee and A. Hadipoor, "Sonographic measurement of bladder wall thickness in healthy children," *Iranian Journal of Pediatrics*, vol. 19, pp. 341-346, 2009.
- [61] P. D. Soden and I. Kershaw, "Tensile testing of connective tissues," *Medical and biological engineering*, vol. 12, pp. 510-518, 1974.
- [62] S. Sivaraman, "Investigating Polymer based Scaffolds for Urinary Bladder Tissue Engineering," 2015.
- [63] A. F. Silva, R. P. Rocha, J. P. Carmo and J. H. Correia, "Photonic sensors based on flexible materials with FBGs for use on biomedical applications," *Current Trends in Short-and Long-period Fiber Gratings*, vol. 1, pp. 105-132, 2013.
- [64] A. M. Sabatini, M. Bergamasco and P. Dario, "Force feedback-based telemicromanipulation for robot surgery on soft tissues," in *Engineering in Medicine and Biology Society, 1989. Images of the Twenty-First Century., Proceedings of the Annual International Conference of the IEEE Engineering in*, 1989.

- [65] M. A. Saab, "Applications of high-pressure balloons in the medical device industry," *Medical Device & Diagnostic Industry Magazine*, pp. 86-94, 2000.
- [66] D. Roylance, "Mechanical properties of materials," *Massachusetts Institute of Technology Publishing. USA*, 2008.
- [67] M. Rothmaier, M. P. Luong and F. Clemens, "Textile pressure sensor made of flexible plastic optical fibers," *Sensors*, vol. 8, pp. 4318-4329, 2008.
- [68] P. Roriz, O. Frazão, A. B. Lobo-Ribeiro, J. L. Santos and J. A. Simões, "Review of fiber-optic pressure sensors for biomedical and biomechanical applications," *Journal of biomedical optics*, vol. 18, pp. 50903-50903, 2013.
- [69] S. Roccabianca and T. R. Bush, "Understanding the mechanics of the bladder through experiments and theoretical models: Where we started and where we are heading," *Technology*, vol. 4, pp. 30-41, 2016.
- [70] P. Ravi, P. S. Shiakolas, T. Welch, T. Saini, K. Guleserian and A. K. Batra, "On the Capabilities of a Multi-Modality 3D Bioprinter for Customized Biomedical Devices," in *ASME 2015 International Mechanical Engineering Congress and Exposition*, 2015.
- [71] P. Polygerinos, Z. Wang, K. C. Galloway, R. J. Wood and C. J. Walsh, "Soft robotic glove for combined assistance and at-home rehabilitation," *Robotics and Autonomous Systems*, vol. 73, pp. 135-143, 2015.
- [72] R. P. Paul and B. Shimano, "Kinematic control equations for simple manipulators," in *Decision and Control including the 17th Symposium on Adaptive Processes, 1978 IEEE Conference on*, 1979.

- [73] R. Mutlu, G. Alici and W. Li, "An effective methodology to solve inverse kinematics of electroactive polymer actuators modelled as active and soft robotic structures," *Mechanism and Machine Theory*, vol. 67, pp. 94-110, 2013.
- [74] B. McGinty, *Continuum Mechanics*, Bob McGinty, 2012.
- [75] L. E. Malvern, *Introduction to the Mechanics of a Continuous Medium*, 1969.
- [76] C. Majidi, "Soft robotics: a perspective—current trends and prospects for the future," *Soft Robotics*, vol. 1, pp. 5-11, 2014.
- [77] W. Liu and C. R. Rahn, "Fiber-reinforced membrane models of McKibben actuators," *Journal of Applied Mechanics*, vol. 70, pp. 853-859, 2003.
- [78] W. Liu, F. Li, C. Stefanini, D. Chen and P. Dario, "Biomimetic flexible/compliant sensors for a soft-body lamprey-like robot," *Robotics and Autonomous Systems*, vol. 58, pp. 1138-1148, 2010.
- [79] W. Liu, A. Menciassi, S. Scapellato, P. Dario and Y. Chen, "A biomimetic sensor for a crawling minirobot," *Robotics and Autonomous systems*, vol. 54, pp. 513-528, 2006.
- [80] H. Lipson, "Challenges and opportunities for design, simulation, and fabrication of soft robots," *Soft Robotics*, vol. 1, pp. 21-27, 2014.
- [81] F.-Y. Lin, C. Bergeles and G.-Z. Yang, "Biometry-based concentric tubes robot for vitreoretinal surgery," in *2015 37th Annual International Conference of the IEEE Engineering in Medicine and Biology Society (EMBC)*, 2015.

- [82] C. Lally, A. J. Reid and P. J. Prendergast, "Elastic behavior of porcine coronary artery tissue under uniaxial and equibiaxial tension," *Annals of biomedical engineering*, vol. 32, pp. 1355-1364, 2004.
- [83] M. P. Krehel, "Polymeric Optical Fibres for Biomedical Sensing," 2014.
- [84] M. Krehel, R. M. Rossi, G.-L. Bona and L. J. Scherer, "Characterization of flexible copolymer optical fibers for force sensing applications," *Sensors*, vol. 13, pp. 11956-11968, 2013.
- [85] S. Kim, C. Laschi and B. Trimmer, "Soft robotics: a bioinspired evolution in robotics," *Trends in biotechnology*, vol. 31, pp. 287-294, 2013.
- [86] Z. G. Jia, W. Li and Z. R. Zhou, "Mechanical characterization of stomach tissue under uniaxial tensile action," *Journal of biomechanics*, vol. 48, pp. 651-658, 2015.
- [87] J. T. Iivarinen, R. K. Korhonen and J. S. Jurvelin, "Experimental and numerical analysis of soft tissue stiffness measurement using manual indentation device--significance of indentation geometry and soft tissue thickness," *Skin Research and Technology*, vol. 20, pp. 347-354, 2014.
- [88] M. Fatemi, A. Manduca and J. F. Greenleaf, "Imaging elastic properties of biological tissues by low-frequency harmonic vibration," *Proceedings of the IEEE*, vol. 91, pp. 1503-1519, 2003.
- [89] M. Es-Souni, M. Es-Souni and H. F. Brandies, "On the transformation behaviour, mechanical properties and biocompatibility of two NiTi-based shape memory alloys:: NiTi42 and NiTi42Cu7," *Biomaterials*, vol. 22, pp. 2153-2161, 2001.

- [90] P. E. Dupont, J. Lock and B. Itkowitz, "Real-time position control of concentric tube robots," in *Robotics and Automation (ICRA), 2010 IEEE International Conference on*, 2010.
- [91] Y. de Jong, J. H. F. M. Pinckaers, R. M. ten Brinck, A. A. B. L. à Nijeholt and O. M. Dekkers, "Urinating standing versus sitting: position is of influence in men with prostate enlargement. A systematic review and meta-analysis," *PloS one*, vol. 9, p. e101320, 2014.
- [92] C. cc, B. J. Berger, F. T. Fischabach and K. D. Pagana, *Cystoscopy test Overview*, 2015.
- [93] J. S. Boyer, *Measuring the water status of plants and soils*, Academic Press, Inc., 1995.
- [94] A. Al-Badr and G. Al-Shaikh, "Recurrent urinary tract infections management in women: a review," *Sultan Qaboos University medical journal*, vol. 13, p. 359, 2013.